

Spring 2019

DEVELOPMENT OF A METHODOLOGY
FOR THE EVALUTATION OF UAV-BASED
PHOTOGRAMMETRY: IMPLEMENTATION
AT AN UNDERGROUND MINE

Rachel Becker

Follow this and additional works at: https://digitalcommons.mtech.edu/grad_rsch

Part of the [Geological Engineering Commons](#)

DEVELOPMENT OF A METHODOLOGY FOR THE
EVALUTATION OF UAV-BASED PHOTOGRAMMETRY:
IMPLEMENTATION AT AN UNDERGROUND MINE

by
Rachel Becker

A thesis submitted in partial fulfillment of the
requirements for the degree of

Master of Science in Geoscience:
Geological Engineering Option

Montana Tech

2019



Abstract

Autonomous systems in underground mining are increasingly being implemented as tools to collect data in inaccessible areas and improve the safety of mine personnel. There are many areas in the underground mining environment that cannot be accessed by personnel due to the high potential for ground fall and insufficient ground support. By combining unmanned aerial vehicles (UAVs) with technologies such as photogrammetry and LiDAR (Light Detection and Ranging) scanners, 3D point clouds can be created for inaccessible sites. A 3D digital point cloud can provide valuable geotechnical information such as the ability to measure discontinuities, inspect rock conditions, generate accurate volume estimates, and obtain a georeferenced geometry of the inaccessible opening.

There are many challenges to operating UAVs and collecting high-quality imagery in underground environments including poor lighting and visibility, dust, water, confined spaces, air turbulence, and a lack of GPS coverage for navigation and stability. Due to the difficult flying conditions and GPS-denied environment, several companies are developing UAVs with LiDAR-based simultaneous localization and mapping (SLAM) to enhance the obstacle detection and avoidance capabilities of the platforms and minimize the potential for a collision.

The objective of this research was to develop a methodology that can be used to evaluate UAV-based imaging tools designed to fly in underground environments. A series of demonstrations was designed to test the functionalities of available UAVs and to identify the most effective platforms for collecting UAV-based photogrammetric imagery in an underground mine. Each of the four participating teams was challenged to fly their UAV-based systems (Hovermap, Elios, M2, Ranger/Batonomous) in underground drifts and long-hole stopes while capturing high-quality imagery that could be used to create a 3D digital photogrammetric model of the opening. The demonstrations were held at Barrick Gold Corporation's Golden Sunlight Mine (GSM) in Whitehall, MT.

The systems were evaluated based upon the performance of the collision avoidance (or recovery) system in the underground environment and the quality and accuracy of the data provided. By successfully completing the underground flights and demonstrating well-developed SLAM-based collision avoidance, the Hovermap system proved to be the most reliable, robust, and easily controllable system. The Elios system, relying on collision recovery rather than avoidance, is an affordable alternative for flights in difficult environments.

The imagery collected by each system was used to generate photogrammetric point clouds using three software packages: Agisoft PhotoScan, Bentley ContextCapture, and Pix4Dmapper. The point clouds were qualitatively compared based on completeness and detail and quantitatively evaluated for accuracy by comparing the geometry of the point cloud to LiDAR scans of the stopes. Based on the results of the qualitative comparison, the point clouds considered in the accuracy evaluation were built using the photogrammetry software Bentley ContextCapture. When the photogrammetric point clouds were compared with the LiDAR point clouds (assumed to be an accurate baseline reference), the mean error values ranged between 0.47 and 2.86 feet. Despite the different conditions and locations in which the imagery was collected for each model, the observed error varies by less than one order of magnitude. Improvements in the coverage and overlap of the imagery as well as in the method used for georeferencing could further increase the accuracy of the photogrammetric point clouds.

Keywords: Unmanned aerial vehicles, photogrammetry, underground mine, LiDAR, point cloud

Acknowledgements

I would like to extend my sincerest appreciation to Dr. Mary MacLaughlin for helping to create the opportunities that have allowed me to complete this research. I would also like to especially thank Ryan Turner for his help coordinating the flight demonstrations, building models, and sharing his knowledge on all things UAVs. Additionally, I would like to thank Micah Gregory-Lederer for his help building and troubleshooting dozens of photogrammetric models. Additionally, I would also like to thank my committee members, Dr. Larry Smith and Jeremy Crowley, for the support and experience they brought to this project.

This project would not have been possible without the generous support of Barrick Gold Corporation's Golden Sunlight Mine and Redpath Mining employees, who provided a safe environment for data collection. Special thanks to Clint Mortenson, Sean Chabot, Kellan Osborne, and Brian Dale for helping considerably with facilitating the underground work. Additional thanks to Gerald Rosas of Barrick Gold, who was instrumental in the business communications between the teams, Barrick, and Montana Tech.

Lastly I am grateful to everyone who took part in the flight demonstrations, either as participants or observers. I learned a tremendous amount through conversations with everyone who visited during the flights. Thank you to Emesent, Near Earth Autonomy, Inkonova, Flyability, and Unmanned Aerial Services Inc. for sharing your technologies and providing your expertise throughout this project.

The material in this document is based upon work supported by the National Science Foundation under Grant No. CMMI-1742880 and by the Alpha Foundation for the Improvement of Mine Safety and Health under Grant No. AFC518-67. The views, opinions and recommendations expressed herein are solely those of the authors and do not imply any endorsement by the National Science Foundation or the ALPHA FOUNDATION, their Directors and staff. Some financial support was also provided by Montana Tech.

Table of Contents

| | |
|--|------------|
| ABSTRACT | II |
| ACKNOWLEDGEMENTS | III |
| LIST OF TABLES..... | VI |
| LIST OF FIGURES..... | VII |
| GLOSSARY OF TERMS | XII |
| | |
| 1. INTRODUCTION | 1 |
| 2. BACKGROUND..... | 4 |
| 2.1. <i>Data Collection Using Laser Scanners</i> | 6 |
| 2.2. <i>Data Collection Using Photogrammetry</i> | 8 |
| 2.3. <i>Enhanced Collision Avoidance for UAVs</i> | 13 |
| 3. PROPOSED RESEARCH | 16 |
| 3.1. <i>Research Objective and Approach</i> | 16 |
| 3.2. <i>Data Collection Site</i> | 17 |
| 4. UNDERGROUND UAV SYSTEM DEMONSTRATIONS | 19 |
| 4.1. <i>Demonstration Summary</i> | 19 |
| 4.2. <i>UAV System Descriptions and Demonstration Summary</i> | 24 |
| 4.2.1. Hovermap System | 24 |
| 4.2.2. Tilt Ranger and Batonomous Systems | 31 |
| 4.2.3. M2 Exploration System | 36 |
| 4.2.4. Elios System..... | 41 |
| 4.3. <i>Demonstration Results</i> | 45 |
| 5. PHOTGRAMMETRIC MODELING RESULTS AND DISCUSSION | 47 |
| 5.1. <i>Qualitative Comparison of Photogrammetric Point Clouds</i> | 48 |
| 5.2. <i>Underground Photogrammetry Results</i> | 50 |

| | |
|--|----|
| 5.2.1. Drift Change Detection | 51 |
| 5.2.2. Stope Photogrammetric Models | 54 |
| 5.3. <i>Evaluation of Photogrammetric Point Clouds</i> | 64 |
| 6. CONCLUSIONS AND RECOMMENDATIONS | 76 |
| 7. REFERENCES CITED..... | 82 |
| 8. APPENDIX A: UNDERGROUND FLIGHT DEMONSTRATION NOTES | 86 |
| 9. APPENDIX B: QUALITATIVE EVALUATION SCORE SHEETS | 91 |
| 10. APPENDIX C: UAV FLIGHT WORKFLOW | 93 |
| 11. APPENDIX D: WORKFLOW FOR COMPLETING PHOTOGRAMMETRIC POINT CLOUD ANALYSIS | 94 |

List of Tables

| | |
|---|----|
| Table I: Qualitative comparison of photogrammetric point clouds produced by three different software packages. Possible scores 0 to 10 (10 being highest) for Completeness and Detail categories and 0 to 20 for the combined total possible score..... | 49 |
| Table II: Comparison of Photogrammetric Point Clouds to LiDAR | 65 |

List of Figures

- Figure 1. Sublevel drifts (drill access 1 and 2) are used to drill and blast the stope. The ore settles at the base of the stope where it is extracted from the draw point and transported for processing (Atlas Copco, 2007).....5
- Figure 2. (*Top*) The points in one image have many possible origins. (*Bottom*) Two offset images provide a unique location for each point in the images (ADAM Technology, 2010).
.....9
- Figure 3. Underground mine map of Barrick’s Golden Sunlight Mine. The UAV system demonstrations were completed in the South Area, shown in detail on the right. .18
- Figure 4. Examples of different flight types including the (*left*) surface wash bay, (*center*) underground drift flight, and (*right*) underground stope flight.....21
- Figure 5. Several 6-inch diameter reflective foam balls were placed in survey collars along the flight path to be used as ground control points (GCPs). GCPs were placed in mine survey monuments using wooden dowels.23
- Figure 6. Emesent’s Hovermap Mining payload (*left*) and Standard payload (*right*).26
- Figure 7. Pre-planned flight path around tree on lawn (*left*) and Hovermap Standard payload completing a semi-autonomous flight (*right*).27
- Figure 8. The Hovermap Standard payload entering the surface wash bay as a stope simulation.
.....28
- Figure 9. The Hovermap Mining payload obstacle detection system was able to identify a rope barricade across the drift (*left*) and a rope hanging from the roof (*right*).29
- Figure 10. (*Left*) The Hovermap Mining payload crashed into a muckpile after a flight controller malfunction. (*Right*) PVC pipe was used to retrieve the UAV from the stope. (*Bottom*)

| | |
|--|----|
| Most of the damage to the UAV was repairable including broken propellers and denting. | 30 |
| Figure 11. (<i>Left</i>) Inkonova’s Batonomous prototype and (<i>Right</i>) Tilt Ranger. Note the wheels were removed from the Tilt Ranger for flight demonstrations. | 32 |
| Figure 12. Damage done to the Batonomous after an unintentional landing in a puddle of muddy water..... | 33 |
| Figure 13. Wear to the Ranger propellers from dust in the air during flight. | 34 |
| Figure 14. First-person view (FPV) goggles used by the pilot to view a live video feed from the UAV during flight..... | 35 |
| Figure 15. Near Earth Autonomy’s M2 platform. | 37 |
| Figure 16. A power station located on the wall along the flight path may have introduced magnetic interference to the UAV’s compass. | 38 |
| Figure 17. Near Earth Autonomy’s M2 platform autonomously navigating the 995-480 drift. | 39 |
| Figure 18. The M2 platform was held near the entrance to the 945 stope to measure the stope with the VLP-16 LiDAR scanner without completing a flight..... | 40 |
| Figure 19: Flyability’s Elios platform. The UAV and camera are mounted on a detachable gimbal so the carbon fiber cage can freely rotate around it. The propellers are located on the bottom of the UAV so that the camera and LEDs (shown in red) can be located on the top. | 42 |
| Figure 20: The Elios was piloted from behind a barricade (metal mesh shown in image) toward the ventilation raise, which is located directly above the Elios. | 43 |

| | |
|---|----|
| Figure 21: Mine rescue scenario where Elios was used to find a “victim” sitting against the wall. | 44 |
| Figure 22. (<i>Top</i>) Two point clouds were constructed at the entrance to the 735 stope using imagery from the Ranger. (<i>Bottom</i>) The results of the change detection analysis show similar alignment where the point clouds overlap. | 53 |
| Figure 23. Results of the change detection analysis completed in the Lower SAM drift at GSM. After an initial flight, three stacks of rocks were placed within the drift to determine if the change could be identified in a photogrammetric point cloud. A, B, and C are photos of the stacks of rocks. For scale, the drift is approximately 15 feet wide and each rock is approximately 1 cubic foot. | 54 |
| Figure 24. Underground mine map of Barrick’s Golden Sunlight Mine. The location of the 102 stope is magnified in black (<i>left</i>) and the location of the 735 stope is magnified in orange (<i>right</i>). | 55 |
| Figure 25: Point cloud associated with LiDAR reference scan of the 102 stope performed on 19 July 2018. Scale is in units of feet. | 56 |
| Figure 26: (Left) Photogrammetric model of the 102 stope from Hovermap imagery. (Right) Photogrammetric model aligned to the LiDAR reference scan point cloud. | 57 |
| Figure 27: (Left) Photogrammetric model of the 102 stope from Elios imagery. (Right) Photogrammetric model aligned to the LiDAR reference scan point cloud. | 58 |
| Figure 28: Point cloud associated with the LiDAR reference scan of the 735 stope performed on 11 September 2018. Scale is in units of feet. | 59 |
| Figure 29: Photogrammetric model of the 735 stope from Hovermap imagery aligned to the LiDAR reference scan point cloud. | 60 |

Figure 30: Photogrammetric model of the 735 stope from Elios imagery aligned to the LiDAR reference scan point cloud.61

Figure 31: Photogrammetric model of the 735 stope from Ranger imagery aligned to the LiDAR reference scan point cloud.62

Figure 32: Photogrammetric model of the 735 stope from Montana Tech imagery aligned to the LiDAR reference scan point cloud.63

Figure 33: Colorized point cloud of the 102 stope measuring the difference from the Hovermap photogrammetric point cloud to the LiDAR reference scan. Circled is a region with high absolute distance that may represent changes in the shape of the muckpile between the time of the LiDAR scan and the time of the imagery collection.66

Figure 34: Colorized point cloud of the 102 stope measuring the difference from the Elios photogrammetric point cloud to the LiDAR reference scan. (*Top*) Circled is the ‘filled in’ entrance to the stope; in reality this is an open excavation to the connected drift. (*Bottom*) Circled is an artifact with a high absolute distance value that is floating centrally within the stope.68

Figure 35: Colorized point cloud of the 735 stope measuring the difference from the Hovermap photogrammetric point cloud to the LiDAR reference scan. Circled is a region with high absolute distance near the outer boundary of the point cloud.....69

Figure 36: Colorized point cloud of the 735 stope measuring the difference from the Elios photogrammetric point cloud to the LiDAR reference scan. Distortion in the photogrammetric point cloud caused the roof of the stope to appear lower than in the LiDAR reference point cloud.....71

Figure 37: Colorized point cloud of the 735 stope measuring the difference from the Ranger photogrammetric point cloud to the LiDAR reference scan. Circled is a region with high absolute distance that may represent changes in the shape of the rock pile acting as a barrier to the stope between the time of the LiDAR scan and the time of the imagery collection.....72

Figure 38: Colorized point cloud of the 735 stope measuring the difference from the Montana Tech M100 photogrammetric point cloud to the LiDAR reference scan. (*Top*) Circled are regions with high absolute distance near the boundary of the point cloud. (*Bottom*) Circled is the high absolute distance near the entrance of the stope is caused from changes in the shape of the barrier rock pile between the time of the LiDAR scan and the time of the imagery collection.74

Glossary of Terms

| Term | Definition |
|-------------------|---|
| UAV | Unmanned aerial vehicle; drone |
| Photogrammetry | The science of using a set of overlapping two-dimensional images to create a three-dimensional (3D) representation of a subject |
| Drift | A horizontal passageway used for travelling through an underground mine |
| Stope | Large underground openings that have been excavated to extract ore |
| Ventilation Raise | A vertical excavation used to connect different levels of an underground mine that allow for clean air to travel through the underground workings |

1. Introduction

Adverse geologic structures within unsupported openings in underground mining environments, such as stopes, raises, and drifts, have the potential to create loose ground and be the source of rock fall that can endanger miners, underground workers, and equipment. Falls of ground are one of the leading causes of worker fatalities in metal mines, so efforts to remediate and better predict these events are a vital safety priority (Benton et al., 2016). In U.S. mines, entry is prohibited into unsupported openings due to the risk of ground fall (MSHA 30 CFR 75.202), and precautionary measures are always taken when working around these sites. Mine personnel face the challenge of collecting data in these no-entry areas, namely regarding the void geometry, rock stability, mine plan progress, and presence of ore minerals. Additionally, engineers need geotechnical data from these areas in order to model and predict potential structural failures.

One method available for surveying an unsupported excavation involves deploying a stationary cavity monitoring survey (CMS) scanner from a boom into the opening (Azhari et al., 2017). A 3D model can be generated from the scan showing the geometry of the void. Because the CMS scanner must remain stationary for several minutes during the scan, it is at a high risk of getting hit by rock fall. The CMS scans are also frequently incomplete because the scanner can only be positioned within line-of-sight of the unsupported opening, leaving holes in the data in any areas that are hidden around corners or behind protruding rock. Laterally extensive and irregularly shaped openings often require several separate scans from different access points, which can make the data collection process time-intensive. The point clouds created from CMS scanners do not usually include RGB (red-green-blue) metadata and only capture the geometry

of the void. Furthermore, the stationary positioning of the scanner leads to decreasing accuracy of the data with increasing distance from the scanner (Azhari et al., 2017).

Increasingly, unmanned aerial vehicles (UAVs) are being investigated as a data collection tool in areas that are otherwise difficult to access using traditional methods (Preston and Roy, 2017; Bamford et al., 2017; Azhari et al., 2017; Russell, 2018). In an underground environment, UAVs provide an opportunity for engineers and geologists to better view and understand the geologic structures in areas that are otherwise inaccessible to mine personnel. A UAV can potentially access more locations within an unsupported excavation while simultaneously collecting high-quality imagery for creating photogrammetric point clouds. These point clouds include RGB data rather than just a scan of the geometry, allowing for geologic structures and mineralization to more easily be identified. Photogrammetric data can be competitively accurate when compared to LiDAR (Light Detection and Ranging) with the use of georeferenced ground control points (Tonon and Kottenstette, 2006; Novel et al., 2016). Some UAVs can simultaneously carry a LiDAR scanner for capturing geometrically accurate point clouds and a camera for collecting high-quality RGB imagery. The LiDAR scans can then be used in conjunction with photogrammetric point clouds to improve geometric accuracy in locations where georeferenced ground control points are lacking while also obtaining RGB metadata.

The demand for UAVs with enhanced obstacle detection and avoidance capabilities has increased dramatically due to the many difficulties of manually piloting a UAV underground and beyond visual line-of-sight. Many of the developing systems rely on LiDAR-enabled simultaneous localization and mapping (SLAM) to navigate through an unknown environment. Most SLAM systems function by using a laser scanner, such as LiDAR, to build a point cloud of the environment and surrounding obstacles while concurrently identifying the position of the

vehicle within the point cloud (Durrant-Whyte and Bailey, 2006). The point cloud is updated continuously as the UAV is in flight, so obstacles can often be detected on the fly. Although systems using SLAM for navigation have been in development for years, the increased payload capacity of UAVs and decreased size and cost of sensors have only recently allowed for the implementation of this tool on aerial vehicles. If UAVs can navigate reliably through difficult underground environments while collecting high quality data, they can serve as tools to allow engineers to have a more detailed understanding of these inaccessible areas and complete geotechnical analyses and risk assessments more accurately, thoroughly, efficiently, and safely.

This thesis describes a study conducted to evaluate the performance of four recently developed LiDAR-enabled UAV platforms equipped with SLAM navigation. A set of UAV system demonstrations was designed to test the four systems in an active underground mining environment. The focus of the demonstrations was to evaluate the ability of the UAVs to collect photogrammetric data, including safely navigating through inaccessible environments while carrying a camera and lighting system and returning with useable data. Included within the demonstrations was a comparison of a set of photogrammetric point clouds built from the imagery collected by the four teams who participated in the demonstrations.

The two primary objectives of this research are to: design and implement a suite of underground demonstrations to evaluate the enhanced navigation and collision avoidance capabilities of UAV systems, and to quantify the accuracy of the 3D digital photogrammetric point clouds built using UAV-based imagery in comparison to LiDAR point clouds.

2. Background

Obtaining geotechnical data is vital for completing stability analyses and risk assessments in underground mining environments. Geotechnical measurements are the foundation for rock strength estimates, rock mass characterization, and ground support design (Vallejo and Ferrer, 2011). In order to ensure a safe working environment for underground miners and personnel, engineers need an adequate understanding of the rock conditions throughout the mine. In U.S. mines, unsupported excavations, including stopes, raises, and ore passes, are inaccessible to underground workers because of the intentional lack of adequate ground support. However, engineers still need to be able to characterize the rock properties within these areas to complete stability analyses and model potential failure zones. Although these areas are barricaded and access is restricted, large ground fall events can still pose safety risks to those working underground. As a large body of rock is displaced during a ground fall event, it creates a high-pressure blast of air that can travel throughout the underground workings, potentially harming mine personnel, utilities, and equipment.

There are several different methods used to extract ore in underground mines depending on factors including the size, shape, orientation, and grade of the ore body and the strength of the surrounding rock. Room-and-pillar mining is used when an ore body is flatly dipping. The ore is mined as rooms, and the pillars are left intact to support the hanging wall. Another method, block caving, is used in ore bodies that are lower grade but very large. In block caving, the rock beneath the orebody is fractured through blasting so the overlying rock and ore body collapse and can be extracted (Hamrin, 2001). This study is focused on investigating the use of UAVs in underground mining methods that involve the excavation of stopes. Stopes are large underground openings that have been excavated to extract continuous ore bodies. More specifically, sublevel

open stoping is a mining method generally utilized for large, steeply dipping bodies of ore surrounded by competent rock (Villaescusa, 2014). Several sublevel access drifts are initially developed into the ore body. The drilling and blasting is completed from the sublevel drifts, beginning from the lowest level, so that the ore falls to the lowest access drift. After the ore settles to the bottom of the stope, it is collected at the draw point, or the lowest access point, for processing. This process is demonstrated in Figure 1, below.

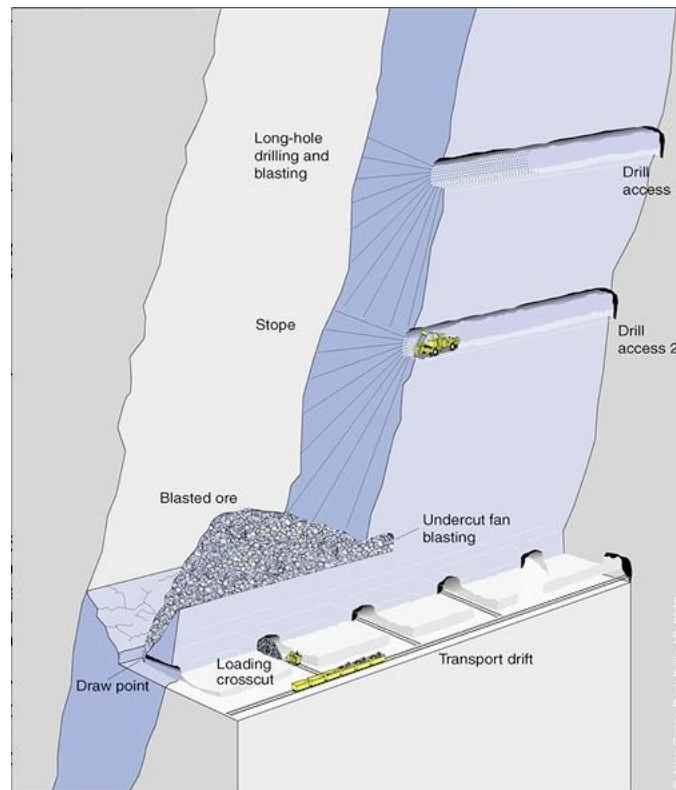


Figure 1. Sublevel drifts (drill access 1 and 2) are used to drill and blast the stope. The ore settles at the base of the stope where it is extracted from the draw point and transported for processing (Atlas Copco, 2007).

To conduct stability analyses of underground openings, engineers rely on data from geologic mapping and the characterization of rock mass discontinuities. The orientation of a set of discontinuities is the major predictor of the mode of failure that will occur. Other parameters including the spacing, roughness, length, aperture, infill material, and presence of water are

pertinent clues that inform how stresses are behaving within the rock. Many of these parameters are inputs for characterizing the quality of a rock mass using geomechanical classification schemes. The most widely used classifications include the Rock Mass Rating (RMR) Quality Index (Bieniawski, 1989), the Rock Tunneling (Q) Quality Index (Barton et al., 1974), and the Geological Strength Index (GSI) (Hoek, 1994). Ground support designs for underground excavations are developed based on the results of these rock classifications (Hoek, 2007).

The following sections discuss data collection using laser scanners and photogrammetry in underground environments. To effectively collect data, UAVs with enhanced navigation capabilities are being built to minimize the incidence of collision, crash, or loss of data. A summary of the methods used to accomplish these tasks is also included.

2.1. Data Collection Using Laser Scanners

Inaccessible underground openings, such as stopes, are currently routinely surveyed to identify how well the post-blast geometry fits the mine design. Divergence from the design in the form of underbreak or overbreak can hinder the productivity of an underground mine. Frequent underbreakage leads to the loss of ore while frequent overbreakage leads to the dilution of ore, both of which decrease the profits and productivity of a mine (Azhari et al., 2017). Stope surveys can be accomplished by extending a cavity monitoring survey (CMS) laser scanner mounted on an extendable boom into the opening (Azhari et al., 2017). The laser scanner, or LiDAR, rapidly emits pulses of laser light that reflect off obstacles and return to the sensor. Because light travels at a fixed speed, the time it takes for the pulse of light to return to the sensor can be used to calculate the distance the light travelled (Donovan and Lebaron, 2009). The compilation of millions of measurements is used to build a 3D digital representation of the geometry of the excavation. The 3D model can be used for various applications including assessing how closely

the stope geometry fits the blast design and identifying rock discontinuities that may be indicative of loose ground or potential areas of failure. When collecting data using an airborne LiDAR system, such as on a UAV, additional flight parameters have to be documented that adjust for the movement of the sensor to ensure a high level of accuracy. The precise location, elevation, and orientation of the UAV are simultaneously recorded using GPS and inertial measurement unit (IMU) data (LiDAR UK, 2019). This helps correct for changes in the position of the laser from when the pulse is emitted and then received.

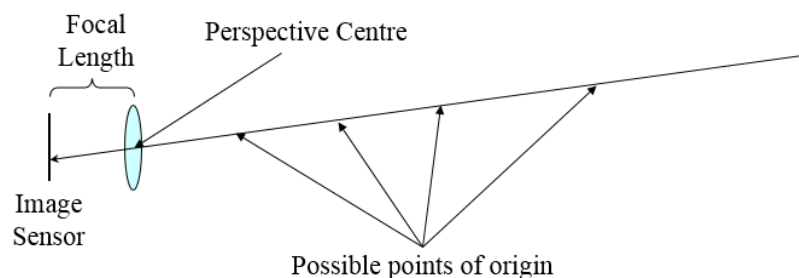
To complete a scan using a CMS scanner, the device is positioned within line-of-sight of a draw point or access point of the excavation and subsequently only collects spatial data for areas within line-of-sight of the scanner. As a result, there can be holes in the data in areas that are obscured by obstacles such as protruding rock, particularly in laterally extensive openings. The quality of the scans also decrease in accuracy as the distance from the scanner is increased (Azhari et al., 2017). To combat these shortcomings, several scans may be completed at different access points to obtain as much coverage as possible. Depending on the size and available access points of the stope, the data collection process can become time-intensive. Additionally, because the CMS scanner is often positioned centrally within the opening for the duration of the scan, it can be at a high risk of getting hit by rockfall. In this instance, the scanner could be damaged or become irretrievable within the stope, potentially requiring the replacement of the scanner. Due to their high cost, the frequent repair or replacement of these scanners can cost a mine significant time and money.

Currently, the primary purpose for CMS scans is to accurately measure the geometry of an excavation to record for mine records and designs. In a geotechnical characterization of rock stability, there are some parameters that are not easy to interpret from a LiDAR point cloud.

Although LiDAR produces high resolution geometric scans, it can be difficult to identify small or ‘closed’ geologic structures from the resulting point clouds (Donovan and Lebaron, 2009; Tonon and Kottenstette, 2006). Other clues used to characterize the rock, including the presence of water or ore minerals, may be more easily identified with the use of RGB (red-green-blue) imagery.

2.2. Data Collection Using Photogrammetry

Photogrammetry is another technique that can be used to determine geometry as well as other RGB-based features for geotechnical characterization. Similarly to the technique that the brain uses to interpret depth from the two-dimensional, offset images it receives from the eyes, photogrammetry is the science of using a set of overlapping two-dimensional images to create a three-dimensional (3D) representation of a subject (Bemis et al., 2014). Figure 2 shows how one image cannot provide enough information to identify the location of a point in space, but two offset images can. Photogrammetric techniques have long been used to record 3D spatial data in the geosciences; the combination of aerial photography and photogrammetry has been a commonly used method for creating topographic maps and collecting geographic information for decades (Matthews, 2008). The applications for this data processing tool have dramatically broadened with the development of widely available unmanned aerial vehicles (UAVs) and software to easily process the captured photographs.



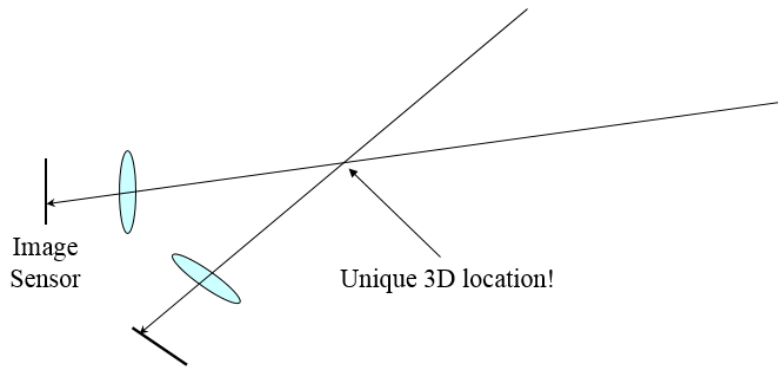


Figure 2. (Top) The points in one image have many possible origins. (Bottom) Two offset images provide a unique location for each point in the images (ADAM Technology, 2010).

Historically, a photogrammetric model was created using a pair or small set of images captured from highly optimized camera positions. Aligning the set of photographs required knowing the precise location and orientation of either the camera or of a set of control points that could be located within the photos (Westoby et al., 2012). With technological advances, the common practice for building photogrammetric models has transitioned to using much larger sets of images from many different, less optimized positions. In modern digital photogrammetry, stereoscopically overlapping images are used to identify the three-dimensional location of a large set of points shared between the images with relation to the camera positions (Bemis et al., 2014). This set of often millions of tie points forms a 3D digital point cloud that can be exported as a variety of surfaces including a mesh, digital elevation model (DEM), or orthomosaic image. Nearly any digital camera can be used to collect imagery for a photogrammetric model, but higher resolution cameras will generally produce higher resolution models (Westoby et al., 2012). Today, the photogrammetry software packages rely less on user-defined inputs and instead solve for the unknown parameters of camera position and orientation using proprietary, iterative analytical processes (Bemis et al., 2014).

The advent of digital cameras and the ability to take numerous photographs of objects or terrain from a range of perspectives has led to digital terrain modeling using photogrammetry, commonly referred to as Structure-from-Motion (SfM) (Westoby et al., 2012). In contrast to traditional photogrammetry, the precise location and orientation of the camera is no longer a required input for model construction using SfM. Instead, the SfM approach simultaneously identifies coordinating features in several images and creates an initial estimate of the camera position. As the features are tracked in more images, the camera positions are refined using an iterative approach. The model geometry is constructed in a relative scale and coordinate system until the user defines these parameters using the coordinates of known ground control points (Westoby et al., 2012). The development of high resolution imaging, sufficient computer processing power, and commercial availability of UAVs and consumer-grade photogrammetry software has simplified the data collection procedure and allowed for UAVs to become a popular tool for collecting photogrammetric imagery. As an added benefit, UAVs can easily access large areas or vertical structures that traditional aerial imagery collection methods can not cover. Larger photosets can be collected and imported into the software packages with ease.

Conventionally, UAVs are being used to capture photogrammetric data above ground by flying in a pre-defined flight plan. Parameters including flight elevation, areal coverage, image overlap, and flight orientation can be defined before the flight depending on the desired resolution and amount of data needed for the model. For a higher resolution model, the UAV can be flown closer to the ground so that each pixel in the image represents a smaller area (Sabins, 1997). The UAV follows the pattern of the flight plan using GPS navigation and captures images over the area of interest without the need for pilot input. In less traditional applications, the data collection process can become more difficult as the need for a skilled pilot is increased.

For a photogrammetric model to have coordinates that are accurate in space, the digital model must be georeferenced using ground control points (GCPs). A ground control point is a target or feature that is included in the imagery and has known spatial coordinates. Typically, GCPs are set up before collecting imagery as easily identifiable targets located throughout the area being imaged. If possible, a minimum of five GCPs should be evenly spaced throughout the area being imaged (Pix4D, 2017). The spacing and positioning of the GCPs can be a factor in the final spatial accuracy of the georeferenced model. After the model is created from the imagery and coordinates are assigned to GCPs in the model, the coordinates of the model will be adjusted to closely match the real-world coordinates. While some of the accuracy of the georeferencing is dependent on the proprietary methods used by each software package, it is also dependent on the accuracy of the survey completed to measure the GCPs (Pix4D, 2017; Tonon and Kottenstette, 2006). Georeferencing is a crucial step for models that will be used for any form of spatial analysis; without accurate georeferencing, a quantitative analysis will not be possible.

As photogrammetry tools become simpler and less expensive, many applications for this data collection and analysis methodology have been identified (Eisenbeiss and Sauerbier, 2011; Bemis et al., 2014; Benton et al., 2016; Turner et al., 2018). Using photogrammetry inherently creates a digital archive of both the imagery captured and the digital point cloud of a site. This detailed record of the conditions at a site at a given moment in time allow for the review and potential revision of an interpretation at a later time. The data collection process can be completed rapidly in the field, and provides the option for interpretation to be completed remotely (Sturzenegger and Stead, 2009). This is ideal for collecting data in areas that have strict timelines for availability. The point clouds created using photogrammetry also include RGB data rather than just a record of the geometry. In geotechnical investigations, a colored point cloud

allows for the easier identification of ‘closed’ rock discontinuities, degree of weathering and discoloration, and the presence of water. Using photogrammetry allows spatial data to be collected more time-efficiently, cost-efficiently, and accurately than other 3D data collection tools (Matthews, 2008). In geotechnical investigations, photogrammetric point clouds provide a new perspective for engineers to view a rock mass. With an accurate photogrammetric model, discontinuities can be measured and characterized from a digital point cloud with similar results to hand mapping in the field (Tonon and Kottenstette, 2006; Sturzenegger and Stead, 2009; Russell, 2018).

When done with precision, photogrammetry can also compete in accuracy with other frequently used survey tools including LiDAR (Tonon and Kottenstette, 2006). The accuracy of a photogrammetry project can be configured by controlling input parameters surrounding the camera calibration and the GCP identification and coordinates. The ground pixel size, which corresponds to the area on the ground that is covered by each pixel in the image, is directly related to the focal length of the camera lens and the distance from the camera to the ground (Sturzenegger and Stead, 2009). By decreasing the distance between the camera and the subject, the GCPs will be easier to identify in the point cloud and the geolocation accuracy will be improved. In a study completed by Tonon and Kottenstette in 2006, a photogrammetric model of an outcrop was created that had a maximum deviation of 1.18 inches from the true rock surface. These results are comparable to some LiDAR systems, which have a reported accuracy of 1.2 inches at the same object distances (Velodyne LiDAR, Inc., 2019).

Most photogrammetry projects follow a similar workflow. After determining the location to be recorded, GCPs are marked and, if a georeferenced point cloud is desired, surveyed. The imagery is collected while adequate overlap, lighting, and resolution are maintained.

Photogrammetric imagery requires a minimum of approximately 60% overlap between adjacent images, but a higher degree of overlap is preferable. Imagery can be captured either as still images or as a video. If using a video, still frames can be extracted at a set interval based on the speed of the movement of the camera. After uploading the images into the photogrammetry software, both sparse and dense point clouds are built. The surveyed GCP coordinates can be used to georeference the point cloud, if desired. The final product can then be built based on the point cloud and exported. A variety of file types are available for export including but not limited to a dense point cloud, triangulated mesh, orthomosaic, or digital elevation model.

2.3. Enhanced Collision Avoidance for UAVs

Flying a UAV in an underground environment creates numerous challenges that are not faced in above-ground scenarios. Most notably, UAVs will often be flown beyond line-of-sight of the pilot in openings that have numerous obstacles including frequent rockfall, irregular geometry, and hanging rock bolts, wire mesh, and rope. Additional challenges include darkness, wet conditions, poor visibility, dust, confined spaces, air turbulence from ventilation, and a lack of GPS for UAV navigation and stability. Because of these difficulties, any UAV that will fly underground needs to be designed specifically to face these obstacles. As the potential role of UAVs in underground mining is being increasingly recognized, companies have begun developing semi-autonomous UAVs with enhanced navigation and obstacle avoidance capabilities. By relying on the UAV's on-board sensors rather than on the skill of the pilot, UAVs can be flown more confidently and successfully into these difficult environments.

One of the more commonly used techniques for developing semi-autonomous UAVs is simultaneous localization and mapping (SLAM) with a laser scanner such as LiDAR. SLAM was

developed in the robotics industry to equip autonomous vehicles with the ability to be placed in an unknown environment and incrementally create a map of its surroundings while also locating itself within the map (Durrant-Whyte and Bailey, 2006). A point cloud is built in real-time from the laser scanner, and the vehicle can differentiate open pathways meant for navigation from walls or obstacles that block its path. Any sensor that can create a point cloud can theoretically be used as the basis for SLAM navigation. LiDAR scanners are a common tool for SLAM because of the reliable accuracy, point density, and relatively quick processing time.

While implementing SLAM for enhanced navigation on a terrestrial vehicle is difficult, applying the navigational tool to a UAV poses additional challenges. The physical size of the system has to be kept to a minimum because all additional weight decreases the available flight time of the UAV. Scanners other than LiDAR, such as SONAR, have also been investigated for use with SLAM for the lighter weight and adequate accuracy for mapping (Azhari et al., 2017). The position of aerial vehicles can prove more difficult to pinpoint than terrestrial systems because of the variable air turbulence that creates random error in roll, pitch, and yaw. The SLAM navigational tool can be combined with inertial measurement unit (IMU) data to improve the accuracy of the position measurements of the UAV and scanner during flight (Paredes et al., 2018; Azhari et al., 2017).

Other sensors can be installed on a UAV for improved collision avoidance and distance sensing that do not rely on SLAM navigation. Time-of-Flight (ToF) sensors estimate the distance of an object by measuring the difference in time between the emission and return of a signal (Corrigan, 2018). A pulse of infrared light is emitted from the sensor, and the return pulse is captured in each pixel of the camera. The return time of the signal is used to measure the 3D

distances for the entire frame in one image. Compared to other existing systems, ToF sensors are simple, compact, and efficient.

In contrast to systems that sense and avoid surrounding obstacles, some UAVs are being designed with barriers to protect the propellers and payload. Installing physical barriers to separate the propellers from the surrounding environment does not necessarily enhance the collision avoidance capabilities of UAVs, however it minimizes the impact of a collision. The two most common forms of physical barriers include propeller guards, which generally protect the outer boundary of the propellers in the same plane as the propeller rotation, and collision-tolerant cages, which encase the entire UAV in an open shell. Physical barriers have the advantages of being low-tech, inexpensive, and easy to replace. However, a strong collision still has the potential to break the barrier and cause the UAV to crash.

3. Proposed Research

Imagery data collected by a UAV in an unsupported excavation can be used to create 3D, digital photogrammetric models that provide spatial information about geologic structures in inaccessible areas. The models allow quantitative measurements to be made in areas that otherwise are difficult to analyze. Recently, Russell (2018) successfully completed an initial proof-of-concept for using UAV-based imagery to model and map an underground rock mass. An off-the-shelf UAV was customized to carry the necessary camera and lighting payload for capturing imagery sufficient for photogrammetry. The portion of the project that is covered in this thesis focuses on the development of a method for evaluating the accuracy of the photogrammetric models generated by available UAV systems. A spatially and geometrically accurate photogrammetric model is necessary for making accurate structural measurements remotely.

3.1. Research Objective and Approach

The objective of this research is to develop a systematic method for comparing photogrammetric models built using imagery collected from different UAV systems designed for semi-autonomous navigation in underground mines. The UAV systems were flown in inaccessible areas of an underground mine, and the resulting photogrammetric models were compared to LiDAR scans to measure accuracy.

The project objective was accomplished in two stages. In the first stage, a series of demonstrations was designed to assess the flight performance of UAV systems specifically with regard to collision avoidance. One of the key objectives for the flights involved the collection of imagery of the underground openings to be used for building photogrammetric models; this challenge required the UAVs to carry a high resolution camera with adequate lighting, maintain

a steady flight orientation, and operate in a controlled and defined pattern. Four semi-autonomous UAV systems designed for flight in underground environments were evaluated.

In the second stage, the data collected by each system were used to build 3D digital photogrammetric models. Ground control points were placed on the walls prior to the flights in each location; however, the necessary control points were not captured in all of the flight imagery. Instead, the models were georeferenced by aligning the photogrammetric point clouds with a georeferenced LiDAR point cloud that had been previously created. A quantitative comparison was completed to assess the accuracy of the photogrammetric point clouds in relation to the LiDAR point cloud.

3.2. Data Collection Site

The data collection for this analysis was completed at Barrick Gold Corporation's Golden Sunlight Mine (GSM) in Whitehall, Montana. Originally mined from the surface as an open pit, GSM is now a narrow vein underground mining operation that uses sub-level long-hole open stoping to extract ore. Figure 3 shows the underground operations known as the 2BUG and South Area (SA) that wrap underneath the previously mined open pit. The demonstrations were completed in drifts, stopes, and ventilation raises within the South Area, which was in active operation throughout the course of the project.

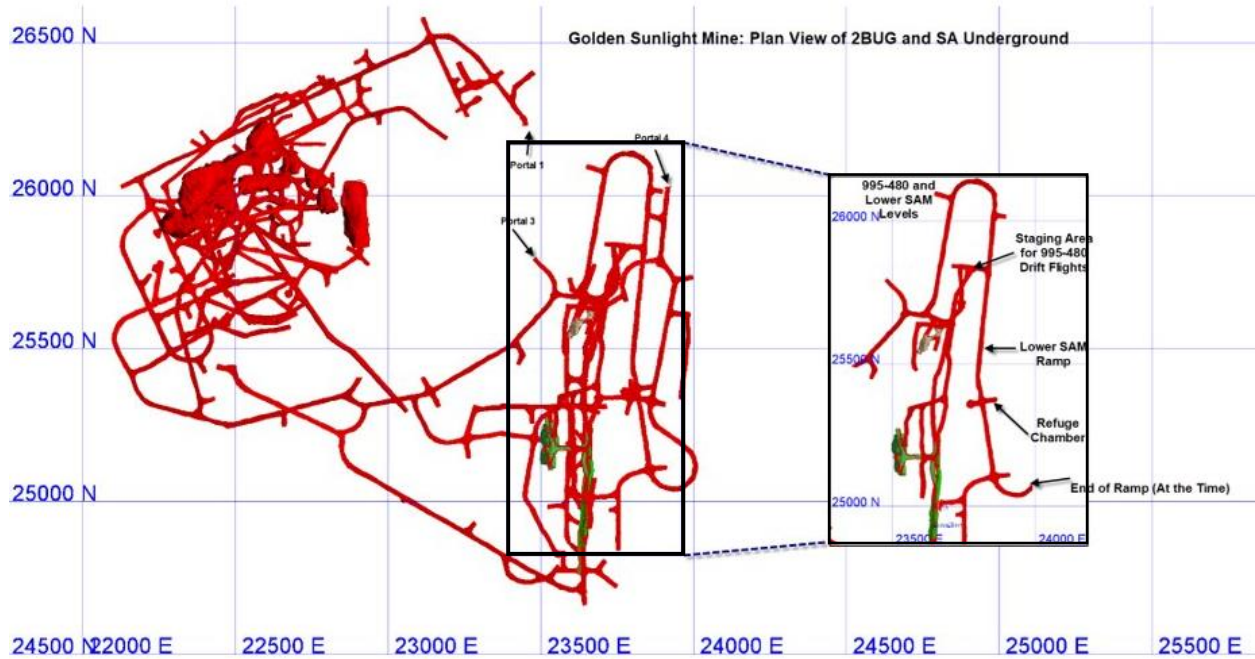


Figure 3. Underground mine map of Barrick's Golden Sunlight Mine. The UAV system demonstrations were completed in the South Area, shown in detail on the right.

4. Underground UAV System Demonstrations

Included in this chapter is a summary of the UAV system demonstrations completed for this investigation. Although a similar pattern was followed for each demonstration, there were slight variations. Details of the flight demonstrations and UAV systems are provided in the following sections. A full record of the flight demonstration notes is provided in Appendix A: Underground Flight Demonstration Notes.

4.1. Demonstration Summary

A series of UAV system demonstrations was developed to test the flight and data collection capabilities of different UAV platforms in inaccessible underground environments. The demonstrations were completed by personnel of contracting companies in underground drifts, long-hole stopes, and in some cases, ventilation raises at GSM. The flight conditions that could be anticipated underground were provided to the pilot and accompanying personnel prior to the flight demonstrations. The flight scenarios were designed to start with the simplest environments and work up to the more complex and higher risk challenges. Each UAV system was tasked with completing several flight scenarios including:

- Surface wash bay flights as a stope simulation
- Underground drift flights to test repeatability and precision
- Underground drift flight with obstacles for change detection analysis
- Underground drift flight beyond line-of-sight
- Underground stope flights within line-of-sight
- Underground stope flights beyond line-of-sight

The demonstrations were designed to provide flight environments that were as consistent as possible given the dynamic nature of an underground mine. While this was not always

possible, the flight demonstrations followed the same general workflow. The initial flights took place in the wash bay, a large surface facility used for washing heavy equipment (Figure 4, left). With the garage door lowered to a height that simulated the roof of a draw point, the UAVs could take off outside and fly into the bay through the opening made by the door. This trial simulated the flight pattern that would be used to fly through the confined entryway of a stope underground. The surface flights also provided an opportunity for the UAVs to be tested after shipment to GSM. The higher elevation at GSM (5500 feet) played a factor in UAV performance, where the thinner air decreases flight time and payload capacity.

Once underground, the UAVs would complete multiple flights along the same section of a drift, within line-of-sight (Figure 4, center). The duplicate flights were completed to demonstrate the repeatability of the flight and to allow for a comparison of the provided data, which included visual imagery and LiDAR point clouds. Obstacles such as rocks, scaling bars, and cones were then placed throughout the drift and additional flights were completed. The purpose of these flights was to collect data that could be used to complete a change-detection analysis. By comparing the flights with obstacles to the flights without obstacles, the level of detail of the point clouds could be tested. Next, the UAVs were flown beyond line-of-sight down the drift, testing the ability of the UAV to detect and avoid obstacles. This flight also demonstrated the usability of the system by the pilot when the UAV was beyond line-of-sight.

The demonstrations continued by flying the UAVs into an open stope (Figure 4, right). These flights were significantly riskier because if a UAV crashed inside of a stope, it could become irretrievable. The flights started outside the draw point, and the ground control points were captured in the imagery before entering the stope. The initial flights within the stopes were kept within line-of-sight of the pilot to minimize the likelihood of a collision. Lastly, the flights

were pushed beyond line-of-sight within the stope. Again, these flights tested the obstacle detection and collision avoidance system on the UAVs and provided an opportunity to collect data that could later be evaluated for accuracy. Based on the results of the previous demonstrations, not all UAV systems were flown into a stope. The ultimate goal of these demonstrations was for the UAVs to be flown with ease in inaccessible underground environments such as stopes, so the successful completion of this step was a strong indicator of the stage of development of each system. If a UAV was successfully flown in each of the previous scenarios, additional flight environments were provided in other challenging areas of the mine including in a ventilation raise. A ventilation raise is a vertical excavation used to connect different levels and allow for clean air to travel through the underground workings.



Figure 4. Examples of different flight types including the (left) surface wash bay, (center) underground drift flight, and (right) underground stope flight.

There are many challenges to face when attempting to fly a UAV in an underground environment. Not only was each UAV system assessed for the performance of its obstacle detection and avoidance system, but observations were also made for how well it was designed to handle the water, darkness, poor visibility, dust, and air turbulence. For each flight completed in the underground UAV demonstrations, several data files were collected. When the UAV was able to carry the weight of a camera, video footage was collected from the perspective of the UAV during the flight. This was the crucial dataset for creating photogrammetric models from the flights. A video was recorded of the flight from the observer's point of view, as well as a

post-flight interview with the pilot debriefing what occurred during the flight. Several team members recorded written notes of the flight summary including the flight number, length of flight, objectives, payload, and summary. When applicable, a LiDAR point cloud was also collected from the UAV flight. The workflow from completing the underground UAV flights is included in Appendix C: UAV Flight Workflow.

In order to obtain correctly scaled and oriented spatial data from a digital point cloud, the model must first be georeferenced. To reduce the distortion and improve the geospatial accuracy of a photogrammetric model, GCPs should be evenly distributed throughout the project area. This poses a challenge when imaging inaccessible areas, as GCPs cannot be easily placed. A recent study has investigated the use of paintballs to mark points that can be both surveyed and identified in photogrammetric imagery with moderate success (Russell, 2018), however these markers cannot be identified in a LiDAR point cloud. To georeference a LiDAR scan, GCPs must be displayed in a manner that can be detected from a laser scanner. Because a laser scanner measures the intensity of the returned signal, highly reflective objects reflect nearly 100% of the laser scan and have a clear contrast from the surrounding material. Utilizing this concept, 6” diameter foam balls were covered with 3M retro reflective tape, and a wooden dowel was used to place the GCPs in survey collars in the wall along the flight path, as shown in Figure 5 (personal communication, Matt McKinnon, July 16, 2018). At least four reflective balls were installed in the walls either along a drift or around a draw point. The GCPs could not be distributed throughout the study area, but several were located near the beginning of the flight path. The coordinates of the survey collars were measured using a Leica total station. The LiDAR point cloud was georeferenced by identifying the location of the spheres within the point cloud and

assigning the corresponding GCP survey coordinates (personal communication, Laurie McBean, January 9, 2019).



Figure 5. Several 6-inch diameter reflective foam balls were placed in survey collars along the flight path to be used as ground control points (GCPs). GCPs were placed in mine survey monuments using wooden dowels.

All new technology that is introduced into a mining environment is held to a high standard of safety. Due to the inherent hazards of working with UAVs, such as the quickly rotating propellers and potential autonomy of the system, all actions were taken to minimize the likelihood that a collision could inflict harm to anyone involved in the flight demonstrations. During the demonstrations, the UAVs were evaluated for their ability to avoid an accident if someone was to unknowingly approach the UAV during flight. In a trial setting, the UAVs were approached from all directions with an obstacle (i.e. a person carrying a shovel or small table) to determine if it could quickly detect and respond to the location of a moving obstacle.

Four UAV systems were evaluated in the demonstrations: Emesent's Hovermap system, Inkonova's Tilt Ranger/Batonomous systems, Near Earth Autonomy's M2 system, and Flyability's Elios system. Each UAV was demonstrated by experienced personnel from the

companies that developed the system, allowing for the best demonstration of the system performance while eliminating the costs associated with purchasing each system.

4.2. UAV System Descriptions and Demonstration Summary

The following sections describe the four UAV systems that participated in the underground flight demonstrations: the Hovermap, Tilt Ranger/Batonomous, M2, and Elios. Also included are details of the flights completed by each UAV system.

4.2.1. Hovermap System

The Hovermap system was developed by Emesent (<https://emesent.io/>), a company that formed after working as part of the CSIRO (Commonwealth Scientific and Industrial Research Organization) Data61 program of Australia. Emesent focuses on the creation and enhancement of autonomous robotic systems, specifically regarding the continued development and commercialization of the Hovermap payload. Designed to allow UAV flight in unconventional GPS-denied environments, the Hovermap payload is mounted on a UAV to provide LiDAR-based SLAM for obstacle sensing and collision avoidance.

The Hovermap system, shown in Figure 6, includes an on-board, rotating Velodyne Puck Lite (VLP-16) LiDAR scanner that identifies when the UAV approaches obstacles without the need for additional lighting or cameras. The VLP-16 measures approximately 300,000 points per second within a range of 330 feet and an accuracy of +/- 1.2 inches (Velodyne LiDAR, Inc., 2019). For the duration of the flight demonstrations, the Hovermap payload was mounted on a DJI Wind 2 UAV, however it can be attached to other UAV platforms. After the attachment of the Hovermap payload, the UAV could carry an additional payload of approximately 3 pounds, allowing for the addition of the LED lights and cameras necessary for capturing

photogrammetric imagery. Although the cost of this system is unavailable, the developers estimate that it is on a similar order of magnitude as a CMS scanner.

Two versions of the Hovermap, the Standard payload (Hovermap VF1) and the Mining payload (Hovermap HF1), were evaluated. On the Standard payload (Figure 6, right), the LiDAR scanner is mounted beneath the center of the UAV, near the center of gravity. On the Mining payload (Figure 6, left), the scanner is still mounted beneath the UAV but it is oriented near the front of the UAV rather than beneath the center. The orientation of the Mining payload allows the scanner to obtain a wider field of view and detect the environment immediately above the UAV, while the Standard payload must fly several feet into an area before having a map of the environment above it. Compared to other systems, both payloads are unique in that the LiDAR scanner is mounted to a detachable gimbal that rotates around a fixed axis. In combination with the rotation of the laser scanner within its housing, the rotating gimbal allows for an angular field of view of 360° by 360° (Hovermap, 2019). Traditional fixed mounting of the Velodyne Puck Lite only allows the LiDAR to capture 360° horizontal by 30° vertical fields of view (Velodyne LiDAR, Inc., 2019).



Figure 6. Emesent’s Hovermap Mining payload (left) and Standard payload (right).

The Hovermap system includes several different flight modes. In *Assisted Flight with Collision Avoidance*, the pilot can manually fly the UAV with SLAM-enabled obstacle detection activated. In this mode, the pilot receives live updates of the distance from the UAV to obstacles in all directions. The pilot can define an obstacle detection radius either before or during flight that actively prevents the UAV from having a collision. The Hovermap can also be flown using *Waypoint Guided Mode*, in which the pilot defines path waypoints based upon the LiDAR point cloud being generated during flight, and the Hovermap autonomously generates a flight path between the waypoints. There are two subsets within the Waypoint Guided Mode: *Posemap* and *Tap-to-Fly*. In the Posemap option, a previously collected point cloud is used to plan the flight waypoints before the UAV takes off. The input point cloud could be one that was collected on a previously flown Assisted Flight or from a stationary LiDAR scanner. In the Tap-to-Fly option, the waypoints are defined while the UAV is in flight based on the point cloud that is actively being generated. The point cloud is updated as the UAV progresses through the environment and is transmitted to the operator. Lastly, a *Free Exploration Mode* is in development and would

allow the UAV to explore an environment fully autonomously without a previous point cloud and without defined waypoints.

The Hovermap flight demonstrations took place from 16-19 July 2018. The first flights were completed using the Standard payload on the lawn above ground to test the equipment after shipment. The obstacle detection and collision avoidance system was initially demonstrated by flying around a large tree located on the lawn. A flight plan, shown in Figure 7, was built based on the LiDAR scan of the lawn, and the UAV flew semi-autonomously around the tree.

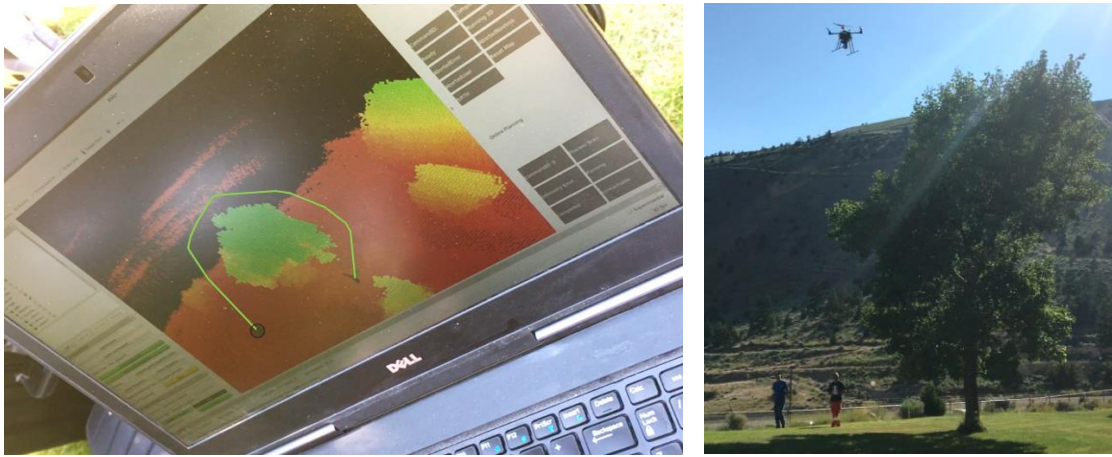


Figure 7. Pre-planned flight path around tree on lawn (left) and Hovermap Standard payload completing a semi-autonomous flight (right).

After the initial tests of the system, the Standard payload was flown in the surface wash bay facility using the *Assisted Flight* mode. With the garage door partially lowered, as shown in Figure 8, the UAV followed a flight pattern similar to entering a stope. The wash bay flights were completed successfully.



Figure 8. The Hovermap Standard payload entering the surface wash bay as a stope simulation.

The underground flights began in the Lower SAM drift using the *Assisted Flight* and *Tap-to-Fly* modes on the Standard payload. The Lower SAM is a straight extent of a drift that approaches an intersection and curve at one end. These flights also demonstrated the obstacle detection and collision avoidance system by identifying and altering the flight path around a rope barricade across the end of the drift and a 0.5-inch diameter rope hanging from the roof (Figure 9). Several flights were repeated with both the Standard and Mining payload along the same extent of the drift in order to complete a change detection analysis of the consistency of the data. These drift flights also included flights beyond line-of-sight, with a safety pilot following behind the UAV to take control if it started to fly off course. Additional drift flights were completed with the Mining payload in the nearby 995-480 drift where the team was not given a preview of the drift. The task was to explore the drift using just the UAV. This flight included flying past the inlet for a ventilation bag, where the air became turbulent. Both the Standard and Mining payload were tested flying within and beyond line-of-sight, and each trial was completed successfully.



Figure 9. The Hovermap Mining payload obstacle detection system was able to identify a rope barricade across the drift (*left*) and a rope hanging from the roof (*right*).

After several successful drift flights, the Mining payload was flown from the 735-level of the 102 stope, a large narrow-vein stope with entry-points at multiple levels. The flights into the stope were completed using the *Assisted Flight* and *Tap-to-Fly* flight modes. During one of the initial *Tap-to-Fly* flights in the stope, a malfunction caused the UAV to diverge from the flight plan and collide with the muckpile within the stope (Figure 10, left). Although personnel are prohibited from entering the stope, the UAV was able to be retrieved using a long segment of 1.5-inch diameter PVC pipe (Figure 10, right) with a repairable level of damage (Figure 10, bottom). The cause of the crash was determined to be from a lapse in communication from the DJI A3 flight controller on the UAV, and the team adjusted the failsafe in the code so that error would not be repeated.

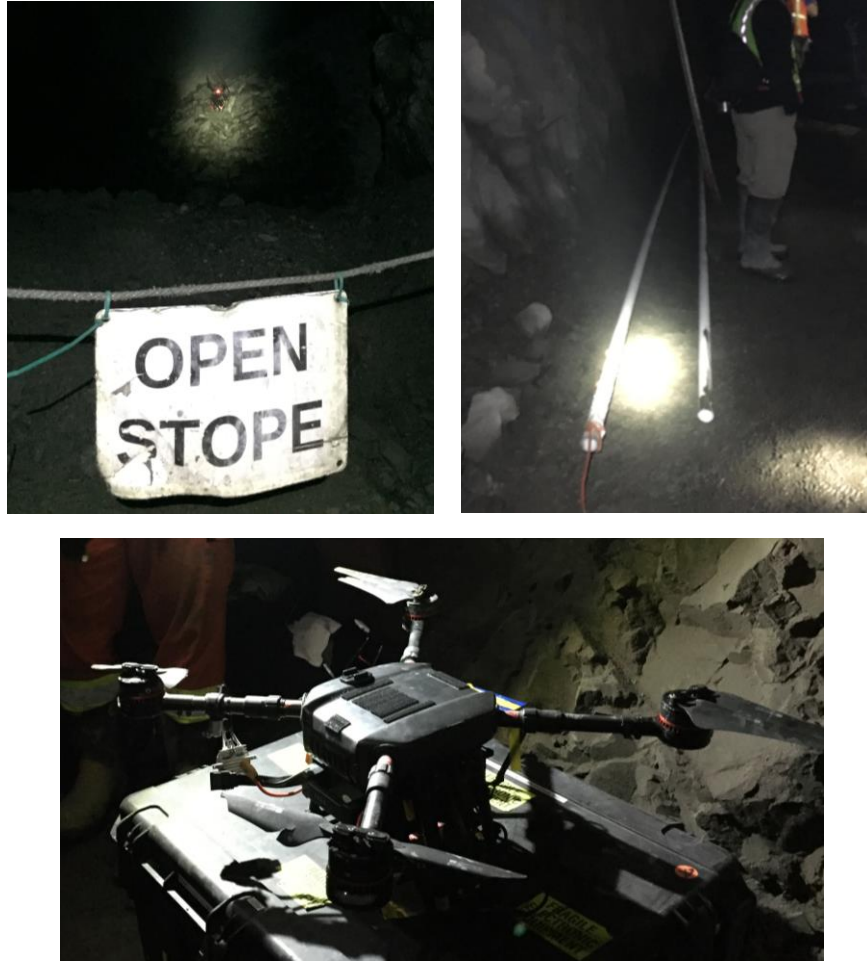


Figure 10. (Left) The Hovermap Mining payload crashed into a muckpile after a flight controller malfunction. (Right) PVC pipe was used to retrieve the UAV from the stope. (Bottom) Most of the damage to the UAV was repairable including broken propellers and denting.

The obstacle detection and avoidance capabilities of both the Hovermap Standard payload and Mining payload were tested in a situation simulating a mine personnel approaching the UAV. In a flight that took place above ground, an obstacle (shovel) was introduced into the path of the UAV on a pre-programmed flight mission. The UAV immediately identified the obstacle and stopped moving forward. It momentarily held its position and attempted to fly around the obstacle. The obstacle was repeatedly moved in front of the path of the UAV, but it continued to maintain its distance from the obstacle. When the obstacle was removed from the flight path, the UAV resumed its mission. The obstacle sensing was also demonstrated by

numerous underground flights in which the UAV identified and avoided hanging bolts, blast lines, rope, welded wire mesh, utilities, and ventilation fans. When using Assisted Flight mode, both Hovermap systems provide feedback to the pilot about the position of obstacles and actively prevent collisions by maintaining a minimum distance away from any detected obstacles.

There were 28 successful flights completed using the Standard payload and 12 successful flights using the Mining payload before the stope crash rendered it inoperable. The team successfully demonstrated the capabilities of the UAV in drifts and stopes both within and beyond line-of-sight.

4.2.2. Tilt Ranger and Batonomous Systems

Inkonova (<http://inkonova.se/>) was founded in 2015 in Stockholm, Sweden. The company started out building racing drones but is now focused on developing UAV technology for underground mining environments. Among the UAVs developed by Inkonova are the Tilt Ranger and the Batonomous systems, shown in Figure 11. The Tilt Ranger is a commercially available and custom-built UAV designed for underground flights. The Tilt Ranger has the weight capacity to carry custom payloads such as a LiDAR scanner or camera. Time-of-flight sensors are located on the front, back, left, right, and top of the UAV to aid in obstacle detection and avoidance. There are forward-facing, onboard LEDs that provide sufficient illumination for photogrammetric imagery. First-person-view (FPV) cameras are mounted facing forward, above, and below the UAV so the pilot can better locate its position when flying with FPV goggles. The Tilt Ranger is designed to be flown manually by the pilot and does not have autonomous flight capabilities. The Tilt Ranger has an estimated cost of approximately \$20,000.

The Batonomous unit is a custom-built, semi-autonomous UAV with a stationary Velodyne Puck Lite (VLP-16) LiDAR scanner mounted on its top. Similar to the Tilt Ranger, the Batonomous has time-of-flight sensors located on the front, back, left, right, and top of the UAV. Forward-facing LEDs provide enough illumination for capturing video for the pilot using the on-board FPV cameras and video for photogrammetry using a GoPro Hero 3+ camera. The Batonomous is available as a beta version.



Figure 11. (Left) Inkonova's Batonomous prototype and (Right) Tilt Ranger. Note the wheels were removed from the Tilt Ranger for flight demonstrations.

Both the Tilt Ranger and the Batonomous have a *Manual* flight mode where the pilot is entirely in control of the UAV without the assistance of obstacle detection and avoidance. Both units can also be flown manually by the pilot with the obstacle detection and avoidance system enabled. The semi-autonomous capabilities of the Batonomous are displayed in *Waypoint Navigation* mode, where the pilot uses a laptop to place waypoints based on the point cloud being generated by the LiDAR scanner on the UAV. The UAV builds a path connecting the defined waypoints that is based on the geometry of the region captured on the LiDAR point cloud.

The demonstrations of the Inkonova systems took place from 26-27 August 2018. The first flights were completed in the surface wash bay to test the equipment after shipment. The demonstrations continued underground in the 895 drift, beginning with a demonstration of the semi-autonomous flight mode using the Batonomous platform. These flights accomplished several objectives including collecting LiDAR point clouds and imagery for photogrammetric analysis that could be used for change detection analysis, demonstrating obstacle avoidance, and flying beyond line-of-sight. In *Waypoint Navigation* mode, the pilot would create waypoints on a laptop displaying the scan of the environment and the Batonomous would fly to the defined points. The Batonomous was manually flown during take-off until the connection with the laptop was verified and the point cloud was created. The pilot would then switch to the semi-autonomous *Waypoint Navigation* mode and control the horizontal position from the laptop. During the second flight with the Batonomous, the UAV briefly lost connection with the controller and landed beyond line-of-sight in the drift. The UAV landed in a puddle of muddy water, and the electrical system was compromised. The damage to the Batonomous, shown in Figure 12, included fine sediment and water covering the landing gear and electrical components of the UAV. The Batonomous flights ranged in length from 2 to 3 minutes.

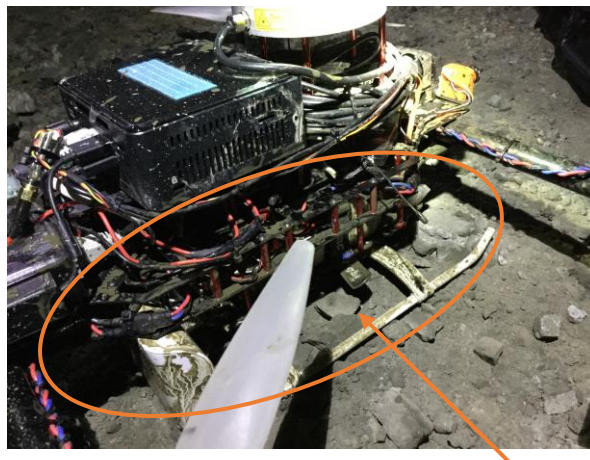


Figure 12. Damage done to the Batonomous after an unintentional landing in a puddle of muddy water.

The flights in the 895 drift were continued with the Tilt Ranger. During the underground flights, the vertical tilt-rotor wheels (Figure 11, right) were removed to improve flight time. For this reason, the Tilt Ranger will be referred to as the Ranger moving forward. The obstacle detection and avoidance system of the Ranger was demonstrated by waving obstacles, such as a folding chair, in front of the UAV in each direction. In each test, the UAV would move in the opposite direction of the obstacle as it approached.

After the drift flights were completed successfully, the Ranger was flown from the 750-level draw point of the 735 stope to collect photogrammetric data. Repeated flights were made to allow for full coverage of the stope. Each flight focused on one section of the wall at a time for the allotted flight time. No crashes occurred within the stope. Some wear was noted on the propellers, as shown in Figure 13, which was attributed to the amount of dust in the air during flight. This was not an issue because worn propellers were easily replaced. Where possible, the flight area was sprayed with water to minimize dust in the air that could interfere with the clarity of the imagery or damage the UAV. An additional flight was completed in which the UAV was flown from the draw point of the 735 stope and around the corner opposite the stope into a drift. One wall was captured during the advance of the flight and the opposite wall was captured during the retreat.



Figure 13. Wear to the Ranger propellers from dust in the air during flight.

The pilot flew both the Batonomous and Ranger using first-person view (FPV) goggles (Figure 14) that showed live video footage from the UAV, so there was no safety pilot following the UAV. The UAVs maintained a less stable flight behavior, however the pilot indicated that the stability could be adjusted based on the preference of the user. The UAV's controls were adjusted to allow for high responsiveness based on the pilot's preferences from his experience in drone racing. Consequently, the UAVs were observed to display lower stability during flight than some of the other systems.



Figure 14. First-person view (FPV) goggles used by the pilot to view a live video feed from the UAV during flight.

The obstacle detection and avoidance of the Ranger was tested underground by moving an obstacle (folding table) in front of the UAV during flight. The Ranger responded quickly when the obstacle was introduced by moving away from the obstacle as it approached. As the obstacle got closer, the Ranger continued to move away from the obstacle, maintaining a defined distance. This method was used to test the obstacle detection in all directions. The upward obstacle detection was also tested by flying the Ranger upward toward the roof. The Ranger

would not fly closer than the defined distance even when the pilot was commanding it to. The obstacle detection capabilities of the Batonomous were not tested due to a malfunction early in the trial. The Batonomous relies on the same technology used in the Ranger and has the added benefit of carrying a LiDAR that is used for SLAM.

A total of 5 flights were completed with the Batonomous and 12 flights were completed with the Ranger. In total, 12 flights were completed in underground drifts and 4 flights were completed in underground stopes. The unexpected landing of the Batonomous in a puddle was the only crash that caused any damage to the UAVs. Flight beyond line-of-sight was successfully demonstrated in both drifts and stopes.

4.2.3. M2 Exploration System

Near Earth Autonomy (<https://www.nearearth.aero/>), based out of Pittsburgh, Pennsylvania, is focused on expanding the capabilities of autonomous flight of unmanned vehicles. Without specifically focusing on underground mining environments, Near Earth Autonomy has developed systems equipped for exploring caves, inspecting tunnels, mapping in GPS-denied environments, and more. They also have multiple contracts with the US military for developing autonomous aircraft.

The M2 exploration system demonstrated by Near Earth Autonomy includes an on-board, stationary Velodyne Puck Lite (VLP-16) LiDAR scanner mounted on the top of a DJI Matrice 100 with propeller guards. Because the LiDAR scanner is mounted to be stationary, the system builds a 2D map of the environment and is not equipped for vertical exploration. The M2 exploration system is not commercially available.



Figure 15. Near Earth Autonomy's M2 platform.

The platform is capable of two different flight modes: *Piloted mode* (P-mode) and *Autonomous mode* (F-mode). In P-mode, the pilot manually controls the UAV without the assistance of the obstacle detection and avoidance system. This mode is dominantly used for take-off and landing. Once the UAV has taken off and is stable, the pilot switched to F-mode. In F-mode, the UAV explores an environment freely without a previously collected map. Using LiDAR-based SLAM, the UAV determines where to travel based on the location of holes in the map it is creating on the fly, attempting to make the map as complete as possible by flying in areas that it can access. Once a single area is fully mapped and there are no large holes, it will explore other areas to expand the map.

The demonstration of the Near Earth Autonomy system took place from 1-2 August 2018. The demonstrations began in the Lower SAM underground drift with a demonstration of the autonomous flight mode and resulting LiDAR scan. Upon take-off, the UAV immediately began showing signs of malfunctions by entering into an uncontrolled yaw-spin in which it would start to rotate in place, accelerating until the UAV was manually landed. This problem has been observed in the past by flights completed by Montana Tech personnel and is attributed to the UAV approaching its maximum payload with insufficient battery power; at this point, one of

the propeller motors stops receiving enough power to keep the UAV in flight, causing an imbalance that rotates the UAV in place. All non-essential components of the payload were removed including the small LED lights and the DJI Zenmuse X3, with just a GoPro remaining to collect imagery. Because no lights could be carried on the UAV, all lighting came from an external, handheld LED flashlight with a brightness of 13,000 lumens. Although several flights were completed along the same extent of the drift, the UAV had repeated problems with clipping the wall near the same location on a curve in the drift. A large power station (Figure 16) located on the wall at that location may have been introducing magnetic interference into the compass; however, the source of this error was never verified. Because of the repeated collisions in this area, most of the flights were limited to 1 to 3 minutes in length.



Figure 16. A power station located on the wall along the flight path may have introduced magnetic interference to the UAV's compass.

The flights continued in the nearby 995-480 drift. The challenge in this location was to fly the UAV system down the drift without having any knowledge about the conditions beyond line-of-sight. The air inlet for a ventilation fan also created air turbulence near the take-off location, creating an additional challenge. The UAV was able to fly past the ventilation fan with only slight instability. The flights in this location lasted between 2-4 minutes and focused on the

ability of the UAV to autonomously travel through unknown areas in exploration mode, shown in Figure 17. These drift flights would also demonstrate the ability to fly beyond line-of-sight; a safety pilot followed the UAV during flight but would only intervene if it went off course. During these flights, the UAV travelled down the center of the drift until it reached an intersection. It made a turn at the intersection and scanned the unexplored area until the data collection was complete. It retreated out of the intersection to the original drift and continued toward the next intersection. When it reached a location in the drift blocked by active mining operations, it turned around and attempted to return to the original take-off location. The UAV had to be quickly landed after getting too close and clipping the wall. The pilot manually flew the UAV back to the starting location.



Figure 17. Near Earth Autonomy's M2 platform autonomously navigating the 995-480 drift.

There continued to be some problems with the uncontrolled yaw spin and the UAV clipping the wall at corners. The Near Earth Autonomy personnel interpreted these collisions as an error in the distance of the obstacle avoidance bounding box and continued adjusting the

dimensions as necessary. The battery also needed to be closely monitored to ensure that there was enough power to keep the UAV in flight without entering the yaw spin.

After facing numerous problems with the flight in the underground, a demonstration of the exploration mode was attempted in the surface wash bay. The wash bay was used to simulate the stope environment by lowering the garage door and placing a truck inside as an added obstacle. Upon take-off, the UAV immediately scanned the entire wash bay without flying past the entrance and did not attempt any further exploration. The free exploration mode also does not allow the pilot to direct the UAV to fly in any specific direction. While the UAV did successfully complete its scan, this did not demonstrate the obstacle avoidance system being used in flight.

The UAV was used to gather additional LiDAR point cloud scans underground by using it as a hand-held device, but no further flights were completed. The UAV was carried from the 995 drift to the 895 drift on another level to test its ability to create maps with three dimensions. The UAV was also held near the 895-level entrance of the 945 stope to determine how much of the stope could be scanned from the opening, as shown in Figure 18. Based on the lack of success in the simpler components of the demonstrations, the stope flights were not attempted



Figure 18. The M2 platform was held near the entrance to the 945 stope to measure the stope with the VLP-16 LiDAR scanner without completing a flight.

A safety demonstration of the M2 exploration system's obstacle detection and collision avoidance was not completed during the flights; instead, observations were made during the other flight demonstrations, particularly with regard to the UAV's ability to quickly adjust to moving obstacles. The main safety concern with the UAV was that it would easily lose control and enter an uncontrolled yaw spin when flown near its maximum payload. When this occurred, the UAV would have to be quickly landed. Despite SLAM-assisted obstacle detection and avoidance, there were multiple collisions with the walls during the flights. Although the UAV system did use propeller guards, which act as a physical barrier around the propellers during a low-velocity collision, a high-velocity collision would likely cause the propeller guards to break.

There were 14 flights completed in underground drifts. All but 5 flights ended in a collision or uncontrolled yaw spin. The team demonstrated flight beyond line-of-sight in a drift, but due to the high rate of collision, a safety pilot was always present. No flights were attempted in a stope.

4.2.4. Elios System

Flyability (<https://www.flyability.com/>), founded in Switzerland in 2014, develops inspection-oriented UAVs designed to safely operate in confined spaces and around people. Flyability's primary product, the Elios, is a commercially available UAV that is contained entirely within a spherical carbon fiber cage. The drone and camera are mounted on a gimbal and are de-coupled from the cage. These components work in conjunction to help minimize the impact of a collision on the flight pattern and imagery of the UAV. The Elios is operated entirely manually by the pilot, but the durability and robustness of the platform allow for a less-experienced pilot to successfully fly the UAV without damage. The standard system includes two cameras mounted on-board including a 1080 HD camera and a non-radiometric FLIR

thermal camera. The cameras located on the front of the Elios transmit a live video feed to the pilot during flight and records video for later use on an on-board SD memory card. There are several adjustable LED lights that face forward, allowing the pilot to adjust the lighting on the fly to achieve the appropriate exposure in the imagery based on the distance of the UAV away from the rock face. There is no LiDAR system integrated for obstacle avoidance. The Elios has an estimated cost of \$25,000.



Figure 19: Flyability’s Elios platform. The UAV and camera are mounted on a detachable gimbal so the carbon fiber cage can freely rotate around it. The propellers are located on the bottom of the UAV so that the camera and LEDs (shown in red) can be located on the top.

The Elios demonstrations took place from 13-14 September 2018. Because the Elios system is designed to recover from collisions rather than avoid them entirely, the flights were completed differently than for the other systems. The first flights were completed in the 895 underground drift, where it demonstrated its ease of flight, durability, and safety when bumping into objects. The drift flights were completed to test different camera positions with relation to the walls for obtaining the best photogrammetric imagery. The Elios was then flown from the 895 level of the 102 stope to investigate the roof and floor of the stope. The same stope was flown the next day after having been blasted on the night shift to collect video imagery of the

results of the blast. Multiple flights were also completed in the 750 drift and the 735 stope in which the Elios was flown beyond line-of-sight to investigate the roof, walls, and around a corner within the stope. The stope flights were all completed successfully with no technical difficulties. Because the Elios does not use a LiDAR for enhanced navigation, ground control points only need to be able to be identified in photogrammetric imagery. Spray painted targets on the walls were sufficient for these flights.

After the successful stope flights, the Elios was flown in the 895 ventilation raise. The strong and turbulent air and confined space in the raise make it difficult for most UAVs to travel. The 895 ventilation raise is approximately 15 feet in diameter and extends 115 feet vertically, connecting two levels of the mine. The carbon fiber cage gave the Elios the unique ability to fly in such a tight space without the concerns for damaging the propellers or crashing that most UAVs would have. Figure 20 shows the Elios approaching the 895 ventilation raise.



Figure 20: The Elios was piloted from behind a barricade (metal mesh shown in image) toward the ventilation raise, which is located directly above the Elios.

The Elios was also used to demonstrate its usefulness for reconnaissance in a mine rescue scenario. A “victim” sat against a wall out of line-of-sight of the starting location, as shown in Figure 21, and the pilot utilized the visual and thermal cameras to locate the “victim”. The pilot relied on the video transmitted from the UAV to manually identify the location of the mine personnel in an area that was hypothetically unsafe to travel on foot.



Figure 21: Mine rescue scenario where Elios was used to find a “victim” sitting against the wall.

Rather than relying on a LiDAR scanner to detect obstacles, the Elios has a physical barrier between the moving parts of the UAV and the user. Throughout the demonstrations, the carbon-fiber cage was demonstrated to be effective for minimizing any interaction between the propellers and humans, utilities, or other equipment. The Elios could be launched from a person’s hands and caught in mid-flight, as long as the user kept their fingers on the outside of the cage. The Elios was even nudged against people during flight and the cage successfully kept the propellers from doing any harm.

A total of 18 flights were completed with the Elios including 6 underground drift flights, 10 underground stope flights, and 1 ventilation raise flight. There were no crashes that caused

damage to the UAV. The team successfully flew beyond line-of-sight in the drift, stop, and ventilation raise.

4.3. Demonstration Results

By successfully completing the underground flights and demonstrating well-developed SLAM-based collision avoidance, the Hovermap system proved to be the most reliable, robust, and easily controllable UAV system. Despite its larger size, the Hovermap was able to fly in the confined environments present at GSM. This was possible because of its ability to hold a steady position during flight, even within a GPS-denied environment. The stable flight allowed for a high degree of overlap and clarity in the provided photogrammetric imagery. Although the obstacle detection and collision avoidance system minimizes the likelihood of a collision, a skilled pilot should be employed when flying the Hovermap due to the high cost of the system.

The Ranger was also successfully flown in both drifts and stops beyond line-of-sight. The small size of both the Ranger and Batonomous systems allows for flight in confined spaces; even within stops and drifts, they can maneuver easily around obstacles such as hanging bolts or wire mesh. Based on the pilot's preference for a more responsive flight pattern, the imagery collected by the Ranger had less clarity and completeness than other systems. By adjusting the responsiveness, it would become easier to control the UAV and complete a stable flight. The Batonomous did not collect any photogrammetric imagery due to its initial crash, however the obstacle detection and collision avoidance system was effective. Once the system is fully developed to include a robust casing that protects its electrical systems from dust and water, it would likely do well in an underground environment.

The Elios system, which relies on collision recovery rather than avoidance, is a more affordable alternative for flights in difficult environments. Because it does not operate with an

on-board LiDAR scanner for SLAM navigation, the price is lower than the other UAV systems evaluated in this study. An additional benefit is that the operator does not necessarily need to be a highly skilled UAV pilot; the Elios is able to withstand most collisions without crashing.

Although the M2 had several technical difficulties in the underground environment, Near Earth Autonomy demonstrated other UAV platforms in development that may have been a better fit for the provided flight conditions. The M2 was not specifically designed for the vertical exploration needed for open stope mining environments; rather, it was more equipped for flight in horizontal excavations such as room and pillar mines.

The UAV systems evaluated in this study were designed to minimize the likelihood or consequences of a collision when flying in difficult environments. Although the obstacle detection and collision avoidance capabilities of each system was demonstrated, a reasonably skilled pilot is still necessary, at this time, to ensure photogrammetric imagery has sufficient overlap and clarity. Like any machine, personnel should be trained to fly a UAV before operating in environments such as stopes.

5. Photogrammetric Modeling Results and Discussion

Photogrammetry, and particularly UAV-based photogrammetry, is a time-efficient method for capturing large amounts of spatial data. For any valid interpretation to be completed on the resulting point clouds, the models need to be reliably spatially accurate. Previous work, completed by Tonon and Kottenstette (2006), investigated the spatial accuracy of photogrammetric point clouds built using terrestrial imagery of surface rock outcrops obtained from individually calibrated camera-lens systems. Similarly, Sturznegger and Stead (2009) studied terrestrial photogrammetry and terrestrial laser scanning as tools for characterizing rock discontinuities.

As commercially available UAV-based systems have become capable of collecting imagery and improved photogrammetric methods (i.e. Structure-from-Motion) have emerged, new software has been developed that does not require well-defined camera lens parameters or locations. Rather than needing a small selection of precisely captured images, models can be constructed from larger selections of images with more image pairs and less defined positions and orientations (Westoby et al., 2012). With these improvements, a wide range of applications for UAV-based photogrammetry emerged in different fields of research. To evaluate the reliability of photogrammetry accuracy, traditional terrestrial photogrammetry was compared to the results of UAV-based photogrammetry projects (Bemis et al., 2014). A comparison was also completed by Novel et al. (2016) analyzing the difference between models produced using aerial photogrammetry and laser scanning for complexly shaped subjects. Expanding on the concern for UAV-based photogrammetry accuracy, a recent study similar to Tonon and Kottenstette (2006) was completed comparing the quality and accuracy of models created using the same set

of input photographs in three photogrammetry software packages: Agisoft PhotoScan, Pix4Dmapper, and Bentley ContextCapture (Becker et al., 2018).

As the above-ground applications for photogrammetry have quickly become widespread, photogrammetry has expanded as a tool for collecting data in underground environments. In a study by Benton et al. (2016), terrestrial photogrammetry was evaluated as a method for monitoring rock movement, ground support deformation, and ground support corrosion in an underground mine. In 2017, Preston and Roy integrated a custom-built UAV to collect photogrammetric imagery in an inaccessible underground site and compared photogrammetry, CMS scans, and borehole camera surveys as investigative tools. Russell (2018) completed a proof-of-concept investigation that an off-the-shelf UAV could be used to collect photogrammetric imagery for geotechnical characterization of rock in an inaccessible underground environment. This work was expanded upon by Turner et al. (2018), who captured UAV-based FLIR (forward looking infrared) thermal imagery to build photogrammetric models to identify loose rock underground.

This chapter contains an analysis of the quantitative spatial accuracy of photogrammetric point clouds built using UAV-based imagery of underground sites. An initial qualitative comparison to determine which photogrammetry software most successfully built underground models is also described.

5.1. Qualitative Comparison of Photogrammetric Point Clouds

A qualitative analysis was completed comparing the photogrammetric point clouds built using images from this study in three photogrammetry software packages: Agisoft PhotoScan, Pix4Dmapper, and Bentley ContextCapture. One photoset was selected from each of the systems evaluated, and the images were used to build point clouds using each software. The

chosen photosets were not necessarily the best photosets for each system, but rather encompassed a variety of site geometries including both drifts and stopes. The focus of the comparison was on the completeness and detail of the point clouds, with each of these categories further broken down into four aspects. The completeness of the model was judged on whether the point cloud had a continuous surface, realistic geometry, lacked excessive artifacts, and lacked distortion. The detail of the model was judged on whether the point cloud had realistic surface texture, surface resolution, visible discontinuities, and recognizable features. In the completeness and detail categories, each of the four aspects was ranked as poor, moderate, or good. Each category was then given a score from 1-10, for a total score out of 20.

The point clouds were anonymously provided to two objective judges to score. With one photoset used from each of the four systems and the point clouds built in three software packages, a total of twelve models was produced for the comparison. The full score sheets completed by the objective judges are located in Appendix B: Qualitative Evaluation Score Sheets. Table I shows the average scores for each of the point clouds.

Table I: Qualitative comparison of photogrammetric point clouds produced by three different software packages. Possible scores 0 to 10 (10 being highest) for Completeness and Detail categories and 0 to 20 for the combined total possible score.

| Site (System) | Completeness | | | Detail | | | Combined Total Score | | |
|-------------------------|----------------------|---------------------------|-------------|----------------------|---------------------------|-------------|----------------------|---------------------------|-------------|
| | Agisoft PhotoScan | Bentley ContextCapture | Pix4Dmapper | Agisoft PhotoScan | Bentley ContextCapture | Pix4Dmapper | Agisoft PhotoScan | Bentley ContextCapture | Pix4Dmapper |
| 102 stope (Hovermap) | 7 | 9.5 | 3 | 8.5 | 9.5 | 5.5 | 15.5 | 19 | 8.5 |
| 102 stope (Elios) | 7 | 9 | 6.5 | 6.5 | 10 | 6.5 | 13.5 | 19 | 13 |
| 895 drift (Ranger) | 8.5 | 10 | 5 | 8 | 10 | 5.5 | 16.5 | 20 | 10.5 |
| Lower SAM drift (M2) | 8.25 | 7 | 7 | 8.5 | 9.5 | 7 | 17 | 16.5 | 14 |

The models built in Bentley ContextCapture scored the highest followed by Agisoft PhotoScan and Pix4Dmapper. Similar results were also observed in a recent study comparing the three software packages using images of a surface outcrop (Becker et al., 2018). Based on the results of the qualitative comparison, the point clouds used for the quantitative analysis were built using Bentley ContextCapture.

5.2. Underground Photogrammetry Results

After the qualitative comparison was completed, the video collected from each UAV flight was used to build photogrammetric models in Bentley ContextCapture. The model building process followed the same general workflow for each point cloud (Bentley, 2017). A project was created to represent any work done on a set of input files. The video file was imported into the software and the parameters used to extract images from the video were defined. These input parameters include the start time, end time, and rate that the images were extracted. In most cases, the images were extracted at a rate of 1 image per second for the duration of the flight. The photos were then submitted to an Aerotriangulation, which calculated the camera parameters and built a sparse point cloud based on the alignment of the photos and identification of tie points. During the Aerotriangulation definition, the *optical properties estimation mode* was set to *multi-pass* rather than the default *one-pass* in the Aerotriangulation settings. By using this setting, the camera parameters including focal length and distortion were more closely estimated, but the computation can take more time to run. After the tie points were identified, the sparse point cloud was used to build the dense point cloud and triangulated mesh. The full workflow for constructing photogrammetric point clouds is included in Appendix D: Workflow for Completing Photogrammetric Point Cloud Analysis.

In the case of this investigation, the point cloud files were often too large to easily manipulate on the designated computer workstation. To combat this, the point clouds were downsampled using the public domain software CloudCompare to have a lower point density and therefore a smaller file size. The geometry of the point cloud is not changed during this process, but the resolution of the point cloud is decreased. To downsample the point cloud, after the existing file is imported into CloudCompare, the *Subsample a point cloud* tool is used allowing the user to define the minimum distance between points. In this investigation, a spatial resampling was selected with a minimum distance of 0.01 feet. The minimum distance is defined in the units of the point cloud. The downsampled point cloud is then saved as a .LAS file type and exported at the highest resolution.

Typically, the photogrammetric point cloud would be georeferenced by visually selecting the location of the GCP and applying the known coordinates to that point in the photogrammetry software. In most of the models built for this study, there were not enough GCPs picked up in the imagery to consistently use this method on the photogrammetric point clouds for all of the flights and teams. Instead, the *fine alignment tool* was used in CloudCompare to align the photogrammetric point clouds to a georeferenced LiDAR point cloud. The georeferenced LiDAR point clouds were used as the ground truth and the photogrammetric point cloud orientation and scale were adjusted to match.

5.2.1. Drift Change Detection

In addition to evaluating the accuracy of the photogrammetric point clouds, the precision of the point clouds was also tested. To measure the repeatability of the UAV-based photogrammetric data collected in the underground environment, several of the drift flights were completed multiple times in order to collect two or more sets of similar imagery. The different

photosets were then used to build point clouds in the same software package. Two point clouds can be imported into CloudCompare and the differences between the point clouds can be identified.

In the first change detection study, imagery collected by the Ranger was used to build two point clouds of the 750-level drift outside the draw point of the 735 stope using Agisoft PhotoScan. The conditions for the flights were held constant, and the same UAV, lighting, and GoPro camera were used to capture the imagery. From the flight video, images were extracted at a rate of 2 frames per second and used to build the point clouds. The point clouds were exported from Agisoft PhotoScan as .LAS file types and imported into CloudCompare for the analysis. The areas in the flights that did not overlap were cropped using the segment tool. Because the point clouds were not initially georeferenced, the two point clouds were aligned by selecting corresponding match points from each of the point clouds. At this point, the cloud-to-cloud distance tool was used to detect the areas that were similar or dissimilar between the point clouds. The resulting model, shown in Figure 22 (bottom), shows a high degree of similarity in areas where the point clouds overlap. The areas with the most divergence (shown in green to red), lie outside of the points shared by both point clouds. Because neither point cloud was georeferenced and the two point clouds were manually aligned to each other, some error may have been introduced in the matching process. For a true change detection analysis, the point clouds should have been georeferenced prior to the difference measurements. This was not possible because there were not enough GCPs captured in the imagery.

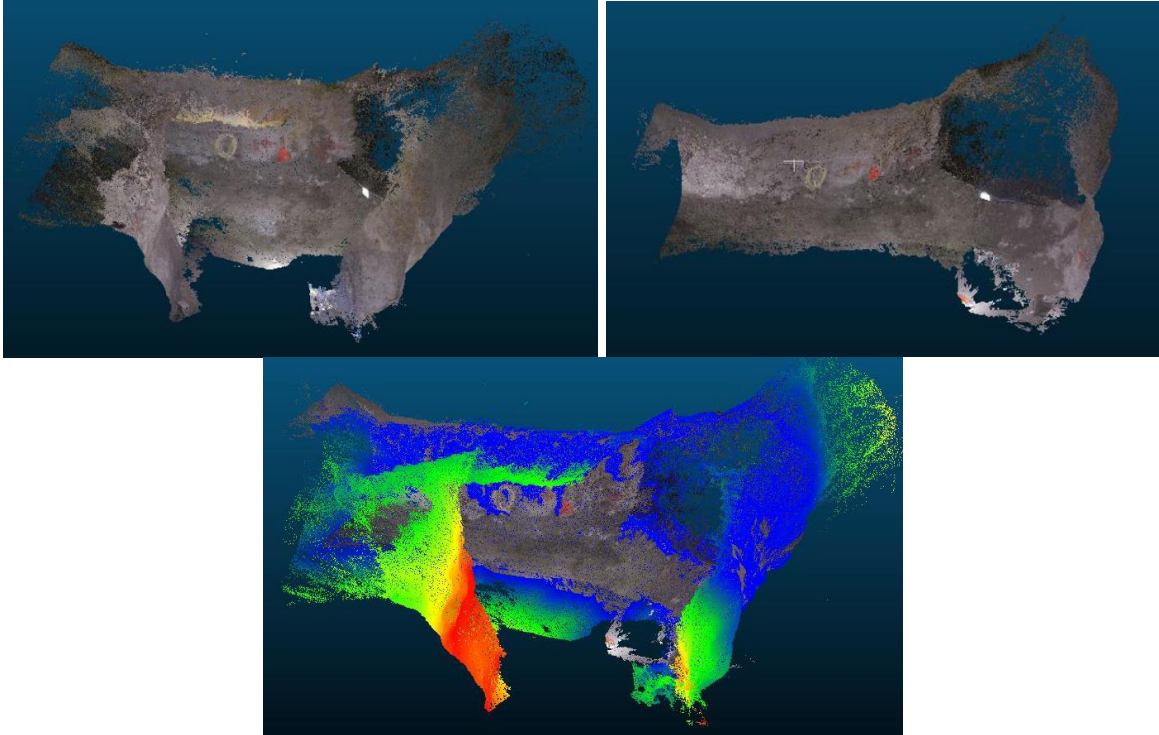


Figure 22. (Top) Two point clouds were constructed at the entrance to the 735 stope using imagery from the Ranger. (Bottom) The results of the change detection analysis show similar alignment where the point clouds overlap.

A second change detection study was completed using the same workflow but purposely introducing new obstacles into the flight path. The Hovermap system was used to capture imagery in the Lower SAM drift. After an initial drift flight with no obstacles, three stacks of rocks were placed randomly along the drift. The flight path was repeated with the same UAV, lighting, and DJI Zenmuse X3 camera. The two flight videos were imported into Agisoft PhotoScan, and images were extracted at a rate of approximately 3 frames/second. The point clouds were exported from Agisoft PhotoScan as .LAS file types and imported into CloudCompare for the analysis. Figure 23 shows the results of the change detection using the CloudCompare *cloud-to-cloud distance tool*. The objects placed before the second flight were detected as changes in the point cloud geometry, shown in Figure 23 by the colorization from

blue to red; the warmer colors represent points farther away from the reference point cloud. Each of the three rock obstacles was identified as being different from the reference point cloud.

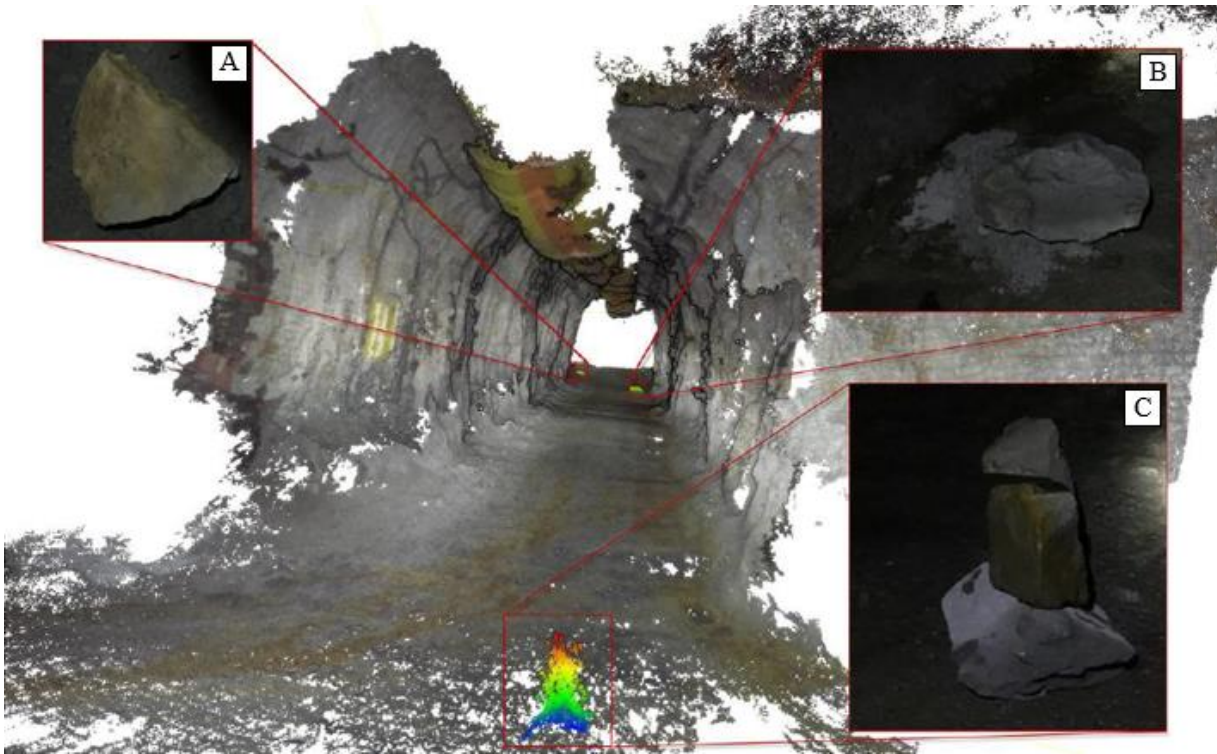


Figure 23. Results of the change detection analysis completed in the Lower SAM drift at GSM. After an initial flight, three stacks of rocks were placed within the drift to determine if the change could be identified in a photogrammetric point cloud. A, B, and C are photos of the stacks of rocks. For scale, the drift is approximately 15 feet wide and each rock is approximately 1 cubic foot.

5.2.2. Stope Photogrammetric Models

Photogrammetric point clouds were constructed with imagery from the 102 stope and 735 stope in the South Area of GSM. In Figure 24, the location of the 102 stope and 735 stope are shown in relation to the underground workings. Although both stopes can be accessed from multiple levels, the UAV was flown from the lowest draw point for each of the following photogrammetric point clouds.

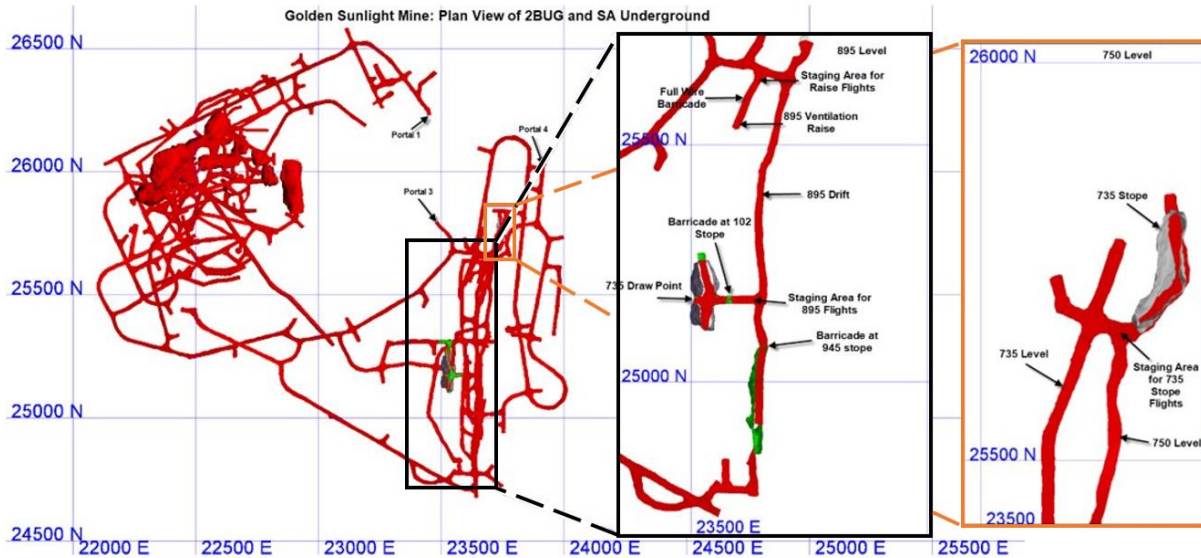


Figure 24. Underground mine map of Barrick's Golden Sunlight Mine. The location of the 102 stope is magnified in black (*left*) and the location of the 735 stope is magnified in orange (*right*).

The 102 stope, shown in Figure 24, extends laterally but can be accessed by a central drift near its base. It is approximately 170 feet tall, 50 feet long, and ranges from 50 to 150 feet wide. The point cloud associated with a LiDAR scan collected from the Emesent Hovermap platform was used as the reference model for the 102 stope model comparison. The stope was measured during a flight beyond line-of-sight on 19 July 2018 and then registered to the mine model. Figure 25 shows the geometry and level of detail captured in the LiDAR point cloud. Incidentally, the same pilot flew the Hovermap and Elios systems to capture the imagery used to construct the following photogrammetric point clouds.

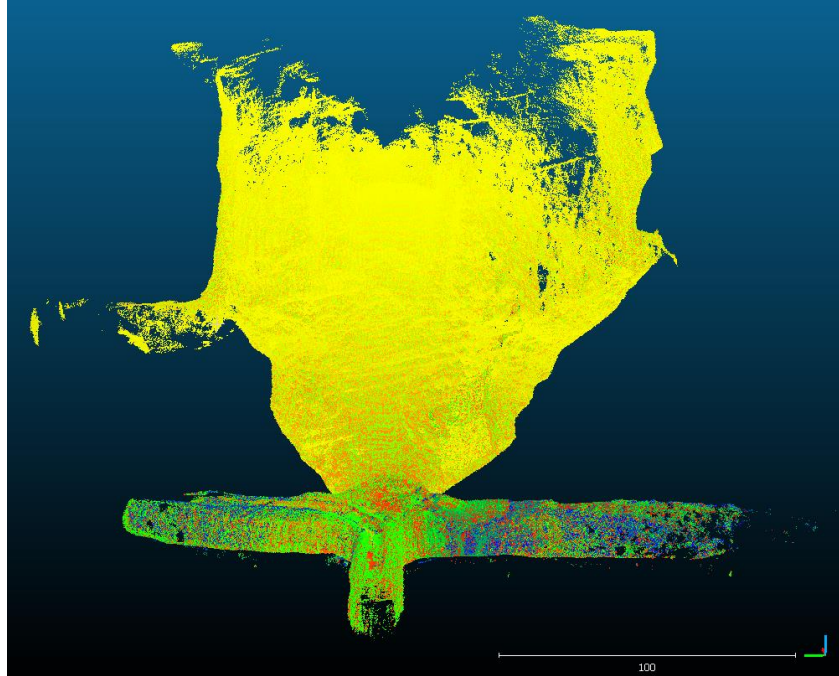


Figure 25: Point cloud associated with LiDAR reference scan of the 102 stope performed on 19 July 2018. Scale is in units of feet.

The photogrammetric model built using the imagery collected of the 102 stope by the Hovermap platform is shown in Figure 26. The imagery was collected on 11 September 2018 in a flight lasting approximately 9.5 minutes. After the UAV entered the 102 stope from the 735 level, the pilot used a vertical flight pattern to ensure the imagery had enough overlap for photogrammetry. The UAV maintained a central position laterally in the stope and was flown up to approximately 20 meters above the floor of the opening and then back down to a height of approximately 3 meters. The pilot then rotated the UAV enough to maintain adequate overlap with the previous strip and repeated the vertical flight. This procedure was repeated multiple times until the stope was fully imaged. The camera, a Zenmuse X3, captured a video of the flight at 29 frames/second. In total, 548 photos were extracted from the flight video at a rate of 1 frame/second, and 520 photos were used to build the resulting point cloud.

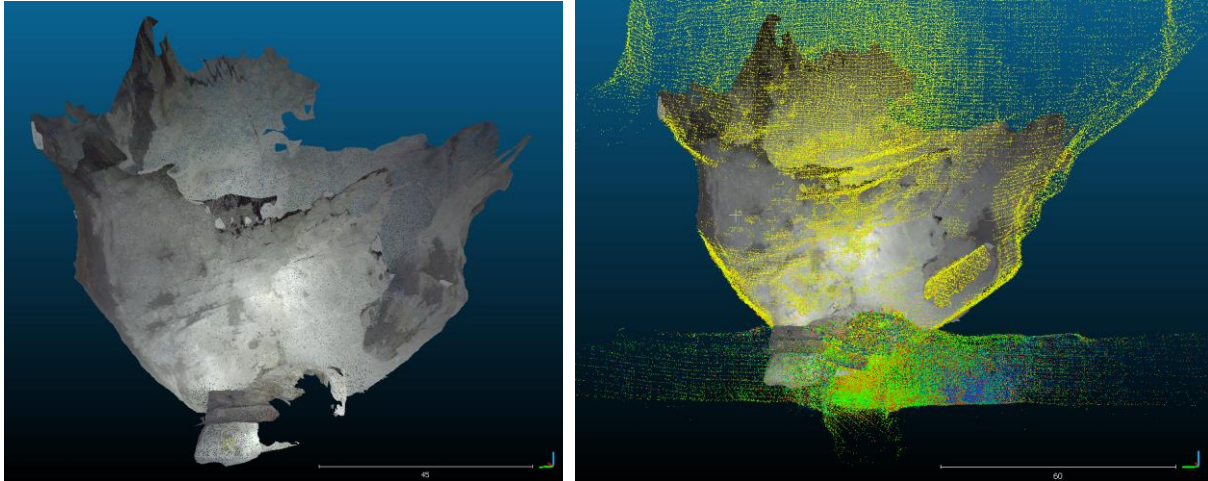


Figure 26: (Left) Photogrammetric model of the 102 stope from Hovermap imagery. (Right) Photogrammetric model aligned to the LiDAR reference scan point cloud.

Imagery of the 102 stope was also collected using the Elios platform on 14 September 2018 in a flight lasting approximately 7 minutes. Similarly to the Hovermap flight, the pilot used a vertical flight pattern for capturing the photogrammetric imagery. Upon entering the 102 stope from the 735 level, the pilot flew the UAV up and down, introducing a slight rotation after each vertical path. The video of the flight was captured using a 1080 HD camera at 30 frames/second. From the video, 430 photos were extracted at a rate of 1 frame/second and 347 photos were used to build the point cloud, shown in Figure 27.

Although the same pilot incidentally flew the Hovermap and Elios for these flights, the behavior of the Elios platform was less stable during flight, causing the video to be blurred in many frames. The Elios also had a slightly lower quality video. These factors contribute to the slightly lower quality seen in the Flyability photogrammetric model.

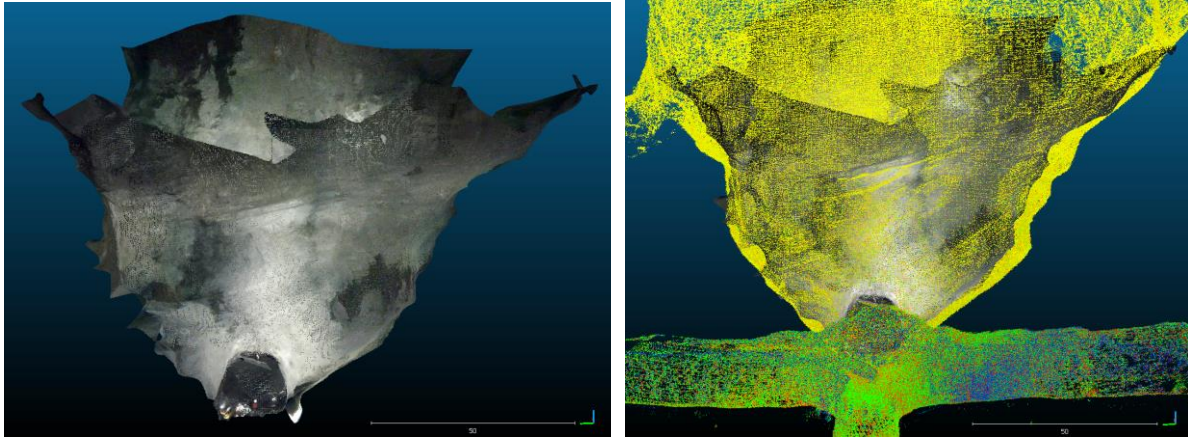


Figure 27: (Left) Photogrammetric model of the 102 stope from Elios imagery. (Right) Photogrammetric model aligned to the LiDAR reference scan point cloud.

The 735 stope, shown in Figure 24, extends laterally but is accessed at the draw point from one end. There is also a slight bend in the shape of the stope that makes it difficult to see around the corner. The stope is approximately 110 feet tall, 20 feet wide, and 140 feet long. A LiDAR scan collected from the Emesent Hovermap platform was once again used to ground truth the photogrammetric models of the 735 stope (Figure 28). The scan was completed during a flight of the stope and then registered to the mine model. The scan was performed on 11 September 2018.

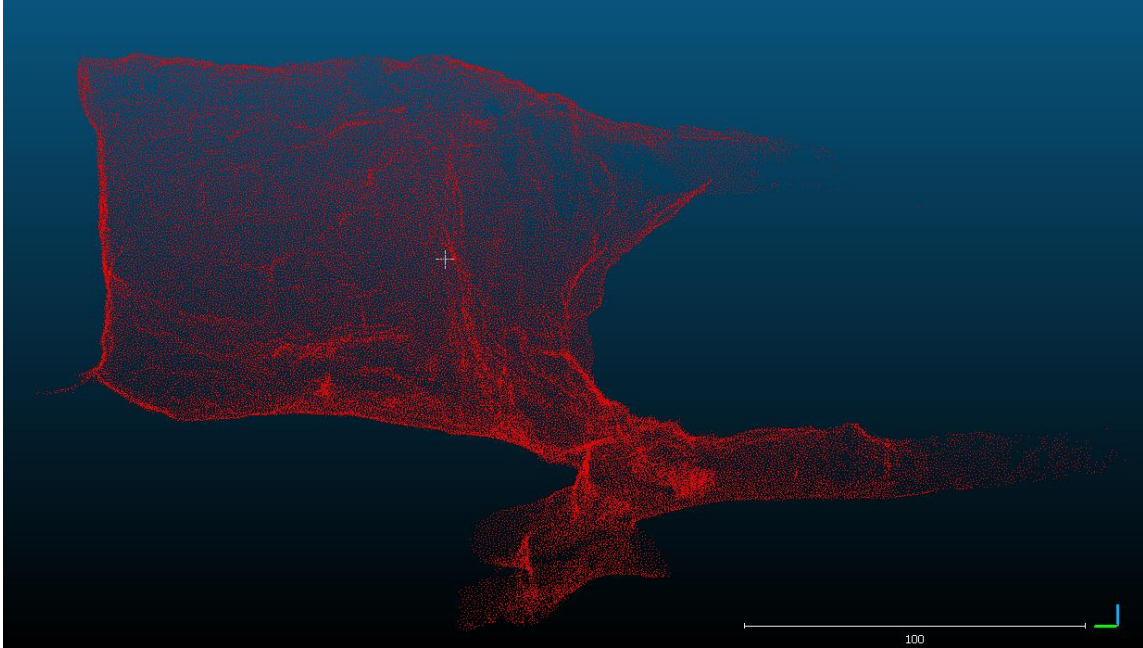


Figure 28: Point cloud associated with the LiDAR reference scan of the 735 stope performed on 11 September 2018. Scale is in units of feet.

Two consecutive flights completed by the Emesent Hovermap platform were used to construct the photogrammetric model of the 735 stope shown in Figure 29. The flights were completed on 11 September 2018, and each flight lasted approximately 6.5 minutes for a total of 13 minutes of flight time. The flights were completed from the 750 level of the 735 stope which is the bottom draw point. The video of the flight was captured using a Zenmuse X3 at 29 frames/second. From the flight videos, 799 photos were extracted at a rate of 1 frame/second and 782 photos were used to build the point cloud.

Neither of the individual flights covered enough of the stope to construct a full model, so two flight videos were used. Because of this, more images were used in the model and the model therefore had a large file size. To combat this, the model was downsampled in CloudCompare using the methodology described in Section 5.2.

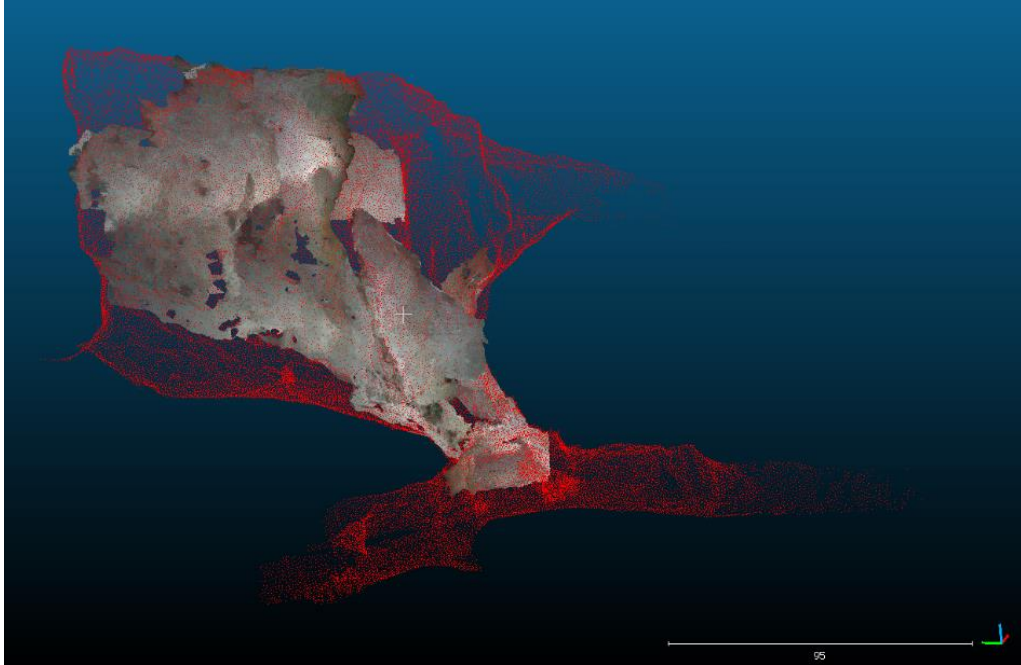


Figure 29: Photogrammetric model of the 735 stope from Hovermap imagery aligned to the LiDAR reference scan point cloud.

The photogrammetric model of the 735 stope from the Elios imagery, shown in Figure 30, was also constructed using two consecutive flights completed on 13 September 2018. Each of the flights lasted approximately 5.5 minutes for a total of 11 minutes of flight video. The flights were flown from the lowest draw point of the 735 stope at the 750 level. Because of the different geometry of the 735 stope, the flight pattern was different than that which was used for the 102 stope. A slight curve in the shape of the stope led to the pilot flying the UAV farther beyond line-of-sight than is typical. The UAV was flown almost directly to the wall of the stope opposite the draw point and flown vertically until it approached the top of the stope. The camera was then repositioned to point upward so that the roof could be imaged. The flight video was recorded using a 1080 HD camera at 30 frames/second. The still images were extracted at a rate of 1 frame/second for a total of 653 images, and 475 were used to build the resulting point cloud.

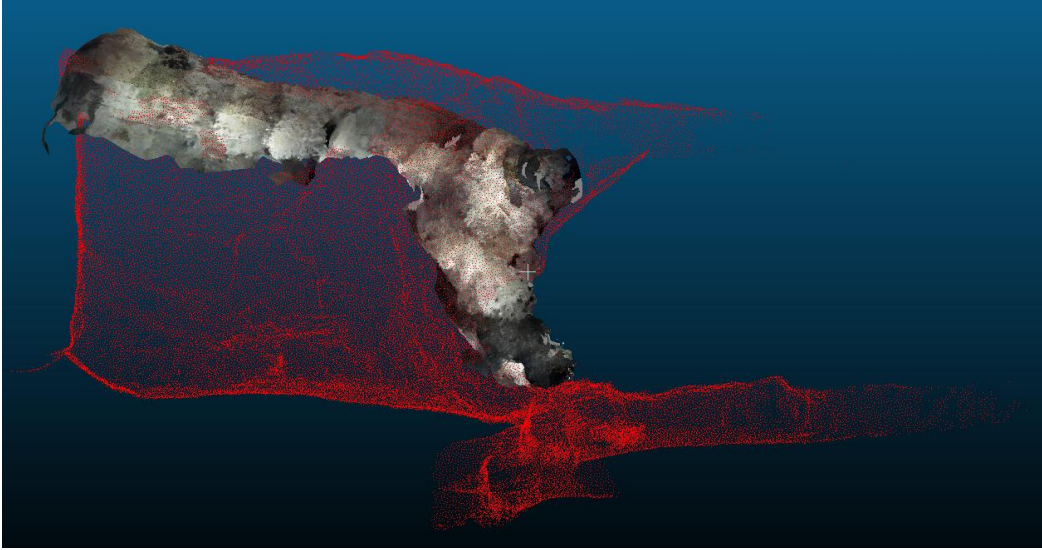


Figure 30: Photogrammetric model of the 735 stope from Elios imagery aligned to the LiDAR reference scan point cloud.

Images from two flight videos collected from the Inkonova Ranger were used for the construction of a third photogrammetric model of the 735 stope. The flights were completed on 27 August 2018, and the video imagery was captured using a GoPro Hero 3+ at a rate of 23 frames/second. The flights focused on the ground control points located outside of the draw point as well as on the left wall upon entry to the stope. Once inside of the stope, a vertical flight pattern was used to capture the necessary overlap in the imagery. The first flight was approximately 5 minutes and the second flight was approximately 2.5 minutes for a total flight time of 7.5 minutes. Still images were extracted from the videos at a rate of 1 frame/second. For the first flight, 292 out of 293 images were used to build the point cloud. For the second flight 131 out of 143 images were used. The two point clouds were built separately and then merged together using the *fine alignment tool* in CloudCompare. This method was used because there was not enough overlap between the two videos for the two photosets to be used to build the same model.

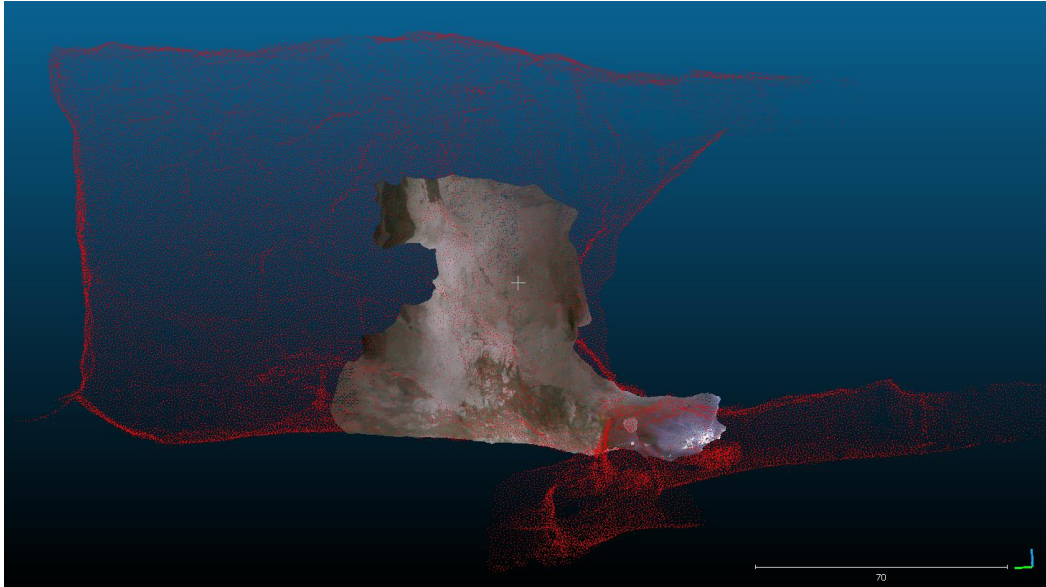


Figure 31: Photogrammetric model of the 735 stope from Ranger imagery aligned to the LiDAR reference scan point cloud.

Also included in this comparison is a photogrammetric model of the 735 stope built using the Montana Tech M100 UAV flown on 31 August 2018. Russell (2018) describes, in detail, the design of the UAV, which consists of a DJI Matrice 100 platform with customizations including high-powered LED lights and lengthened legs for landing. Imagery from two flights was used to build the photogrammetric point cloud. The first flight followed a vertical flight pattern along the right wall near the corner where the stope begins to curve beyond line-of-sight and lasted approximately 3.5 minutes. The second flight followed a horizontal flight pattern where the pilot flew to the top of the stope and flew in horizontal strips on the way back to the draw point. This flight lasted approximately 6.5 minutes and focused on the right wall. In total, 626 images were extracted from 10 minutes of flight video, and 565 images were used to build the two models. The two point clouds were merged using the *fine alignment tool* in CloudCompare.

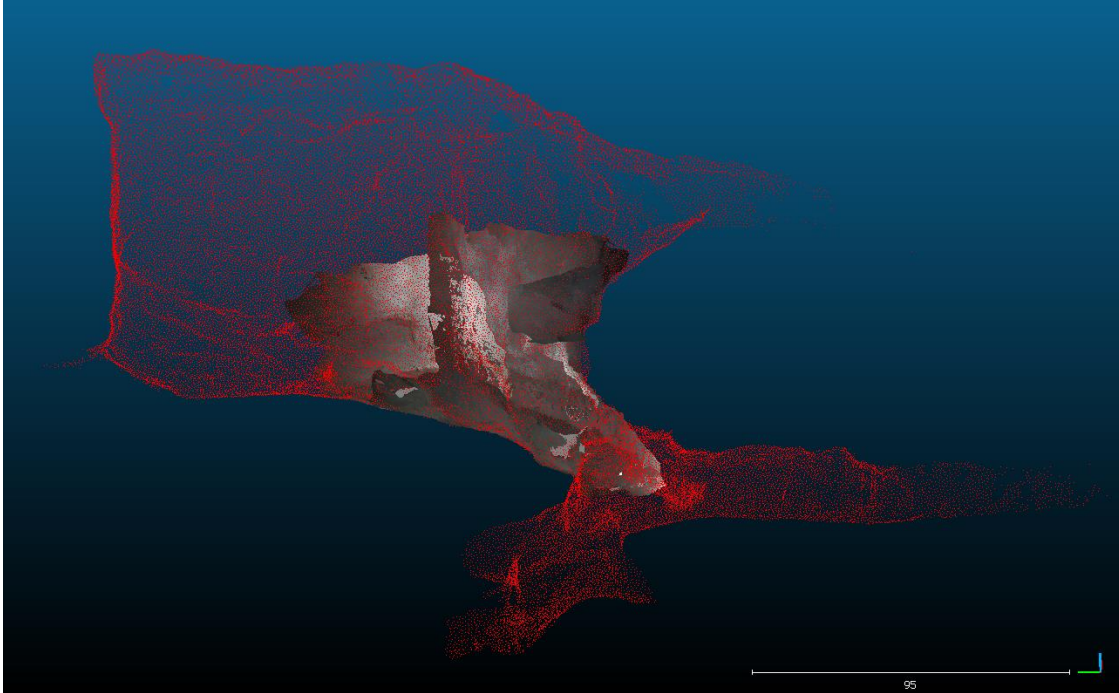


Figure 32: Photogrammetric model of the 735 stope from Montana Tech imagery aligned to the LiDAR reference scan point cloud.

The vertical strip flight pattern used in the 102 stope ensured adequate coverage based on the stope geometry, and the slow flight speed ensured adequate overlap in the imagery. Because of this, the point clouds have few holes and are geometrically realistic. This flight pattern is not always possible or ideal in different stope geometries. A horizontal strip pattern was more appropriate in the laterally extensive 735 stope. However, the incompleteness of the models of the 735 stope indicate the imagery did not have enough overlap between strips and did not cover enough of the stope geometry; improving the flight pattern to systematically image the stope would help to ensure a complete and detailed photogrammetric point cloud could be constructed. The imagery collected from flights that did not follow a methodical flight plan, including some of the 735 stope flights, produced point clouds with more holes and erroneous geometries.

Overall, the completeness of coverage observed in the models of the 735 stope varied significantly between the different systems that were used to perform the imaging. Compared to

the 102 stope, the models have a less complete geometry and include more holes in the areas that were processed. This inconsistency decreases the effectiveness of a direct comparison between the different groups' models. The poorer quality dataset is likely due to the larger and more complex geometry of the stope; capturing the entire stope required longer and more skillful flights that were not always possible in the allotted timeframe.

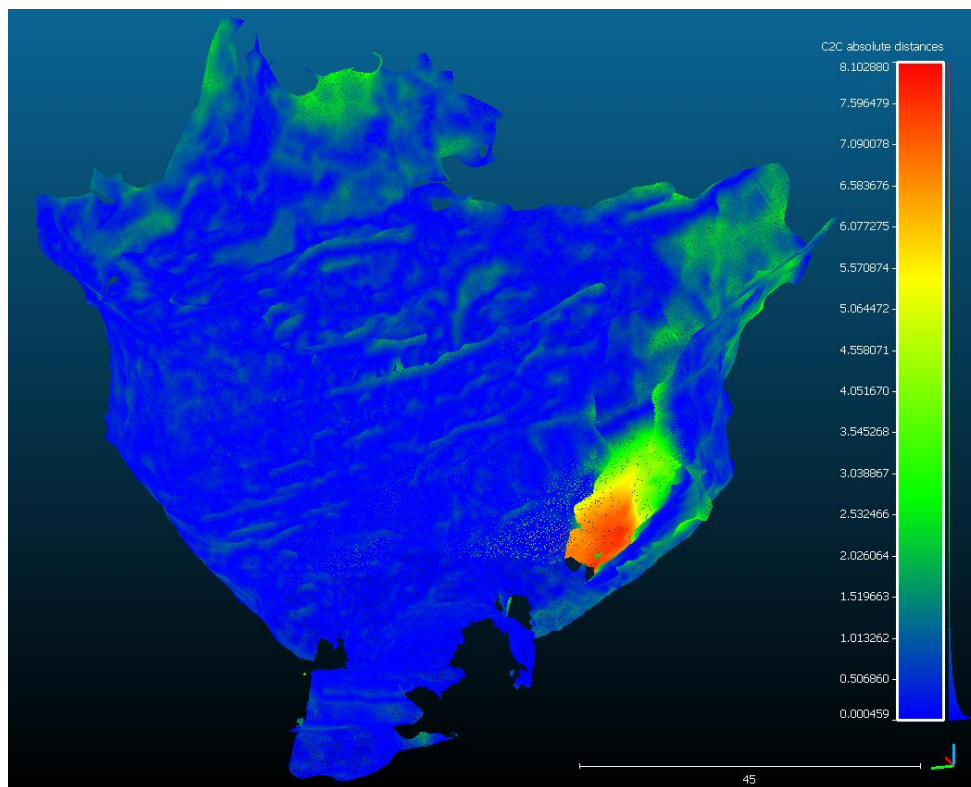
5.3. Evaluation of Photogrammetric Point Clouds

A quantitative comparison of the photogrammetric point clouds was completed using the public domain software *CloudCompare*. This was accomplished by importing both a georeferenced LiDAR point cloud and an unreferenced photogrammetric point cloud into the software. The *fine alignment tool* was used to match the scale and orientation of the photogrammetric point cloud to the coordinates of the LiDAR point cloud. The *cloud to cloud distance tool* was used to quantify the difference between the LiDAR and photogrammetric point clouds. The tool measures the distance from each point in the photogrammetric point cloud to the closest point in the LiDAR point cloud and outputs the average, standard deviation, and root mean square error of the distance between point clouds (Cloud-to-Cloud Distance, 2015). The resulting point cloud is colorized based on the distance value from the reference LiDAR point cloud in the same units as the point cloud. Figure 33 shows the colorized point cloud measuring the difference between the photogrammetric point cloud built using Hovermap imagery and the reference LiDAR point cloud, in units of feet. For this investigation, the LiDAR point clouds are assumed to be correct in order to measure the photogrammetric point cloud accuracy; in reality, LiDAR point clouds also have some inherent error that is being ignored. The full workflow for measuring the accuracy of the photogrammetric point clouds is included in Appendix D: Workflow for Completing Photogrammetric Point Cloud Analysis.

The results of this analysis, shown in Table II, include the root mean square error, mean error, and standard deviation of the difference between the photogrammetric and LiDAR point clouds. Despite the sometimes variable flight and stope conditions, the photogrammetric point clouds have fairly consistent error. All of the point clouds analyzed fall within one order of magnitude of error from the LiDAR reference scan. Despite the lower quality of the point clouds of the 735 stope, the error does not differ significantly from the error in the 102 stope point clouds.

Table II: Comparison of Photogrammetric Point Clouds to LiDAR

| Location | System | Root Mean Square Error (ft) | Mean Error (ft) | Standard Deviation |
|-----------|-------------------|-----------------------------|-----------------|--------------------|
| 102 Stope | Hovermap | 1.54 | 0.67 | 1.01 |
| | Elios | 2.78 | 1.59 | 1.91 |
| 735 Stope | Hovermap | 0.75 | 0.53 | 0.37 |
| | Elios | 3.59 | 2.86 | 2.13 |
| | Ranger | 1.20 | 0.81 | 0.78 |
| | Montana Tech M100 | 0.68 | 0.47 | 0.25 |



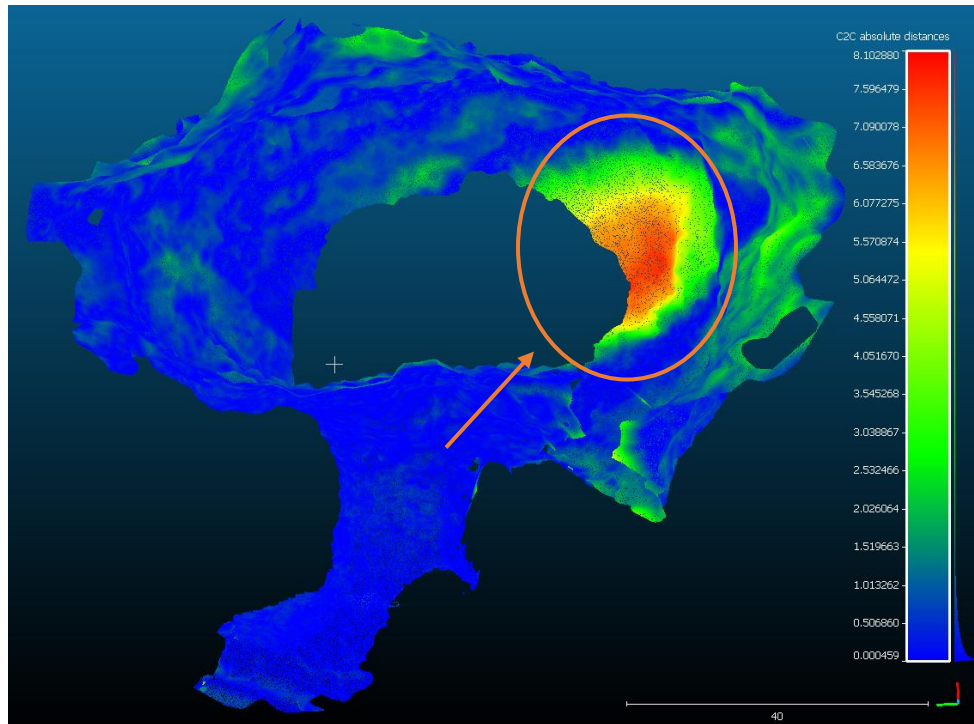
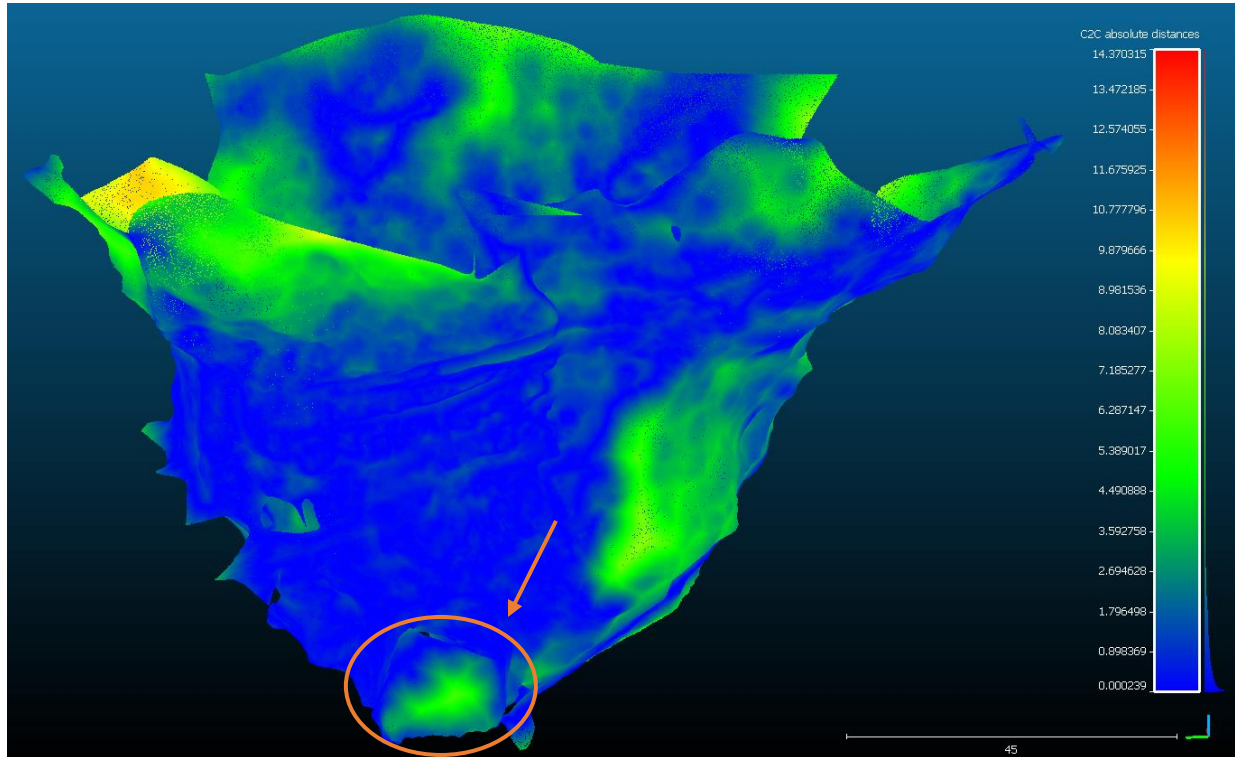


Figure 33: Colorized point cloud of the 102 stope measuring the difference from the Hovermap photogrammetric point cloud to the LiDAR reference scan. Circled is a region with high absolute distance that may represent changes in the shape of the muckpile between the time of the LiDAR scan and the time of the imagery collection.

It should be noted that the LiDAR scan used to compare against the photogrammetric point cloud was not collected at the same time as the photogrammetric imagery. For this reason, there is some difference between the point clouds that is due simply to changes in the geometry or work conditions of the stope. The large amount of error shown near the bottom of the stope in Figure 33 may be due to changes in the size of the muck pile between the time of the LiDAR scan and the time of imagery collection. The mean error is also influenced by outliers such as random artifacts that appear in the point clouds. The point cloud of the 102 stope from the Elios imagery, shown in Figure 34, bottom, includes a small artifact floating within the center of the stope. When viewing the point cloud in 3D, it is clear that this is an error built as part of the point cloud. It can be clearly observed in Figure 34, and it also appears to be the only area of the point cloud with an error over 10 feet, shown as dark orange or red in the legend. By removing this

artifact, the mean error could be decreased. The entrance to the stope is also modelled as being a solid feature when it is actually the excavated opening of a drift, as noted in Figure 34, top.

These errors, while increasing the overall error of the point cloud, are not specifically indicative of error in the geometry or spatial alignment of the point cloud.



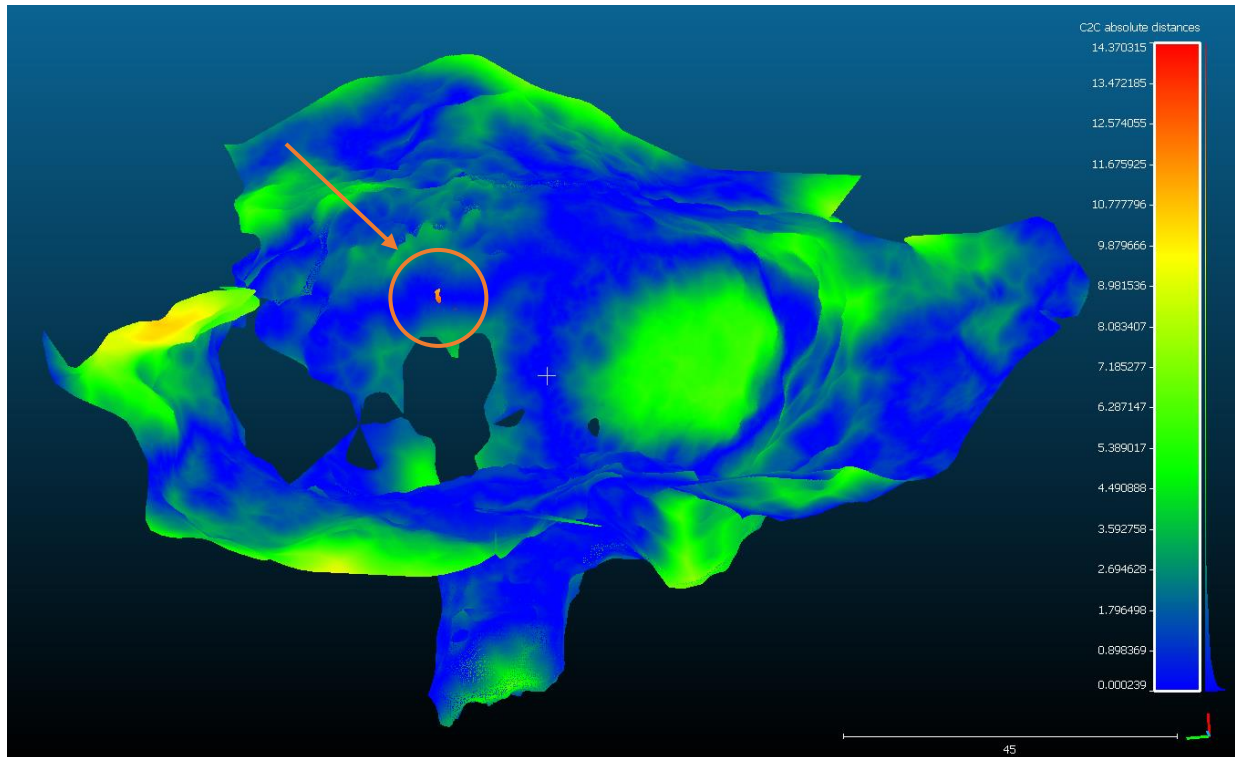


Figure 34: Colorized point cloud of the 102 stope measuring the difference from the Elios photogrammetric point cloud to the LiDAR reference scan. (Top) Circled is the ‘filled in’ entrance to the stope; in reality this is an open excavation to the connected drift. (Bottom) Circled is an artifact with a high absolute distance value that is floating centrally within the stope.

Although the Hovermap point cloud of the 735 stope (Figure 35) is incomplete and has several holes, it matches closely with the LiDAR reference point cloud. As expected, the areas that diverge from the reference point cloud are near the edges of the photogrammetric point cloud, as shown by the green to red coloration circled in Figure 35. The abundance of holes in the point cloud indicates that the flight pattern used in the stope did not have adequate overlap and coverage. Unlike the other point clouds of the 735 stope, the Hovermap system covered the majority of the stope along one wall. Other point clouds cover a much smaller portion of the excavation.

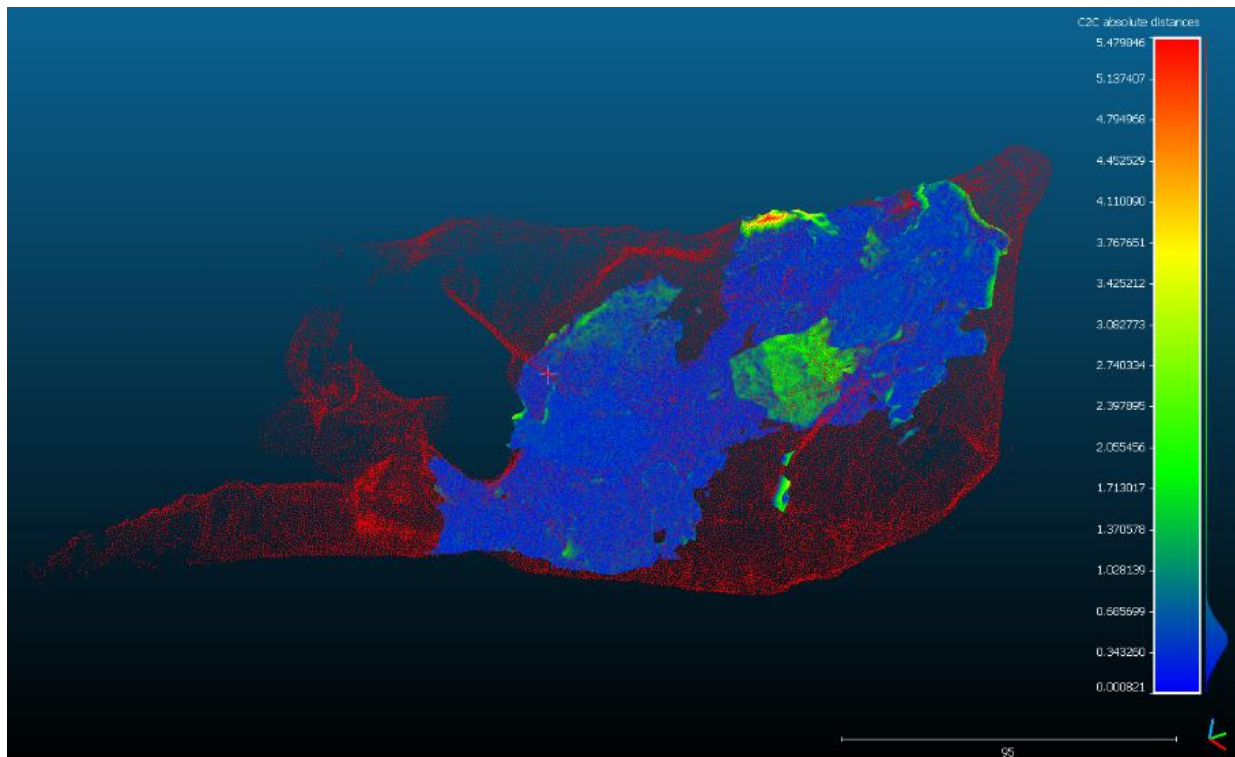
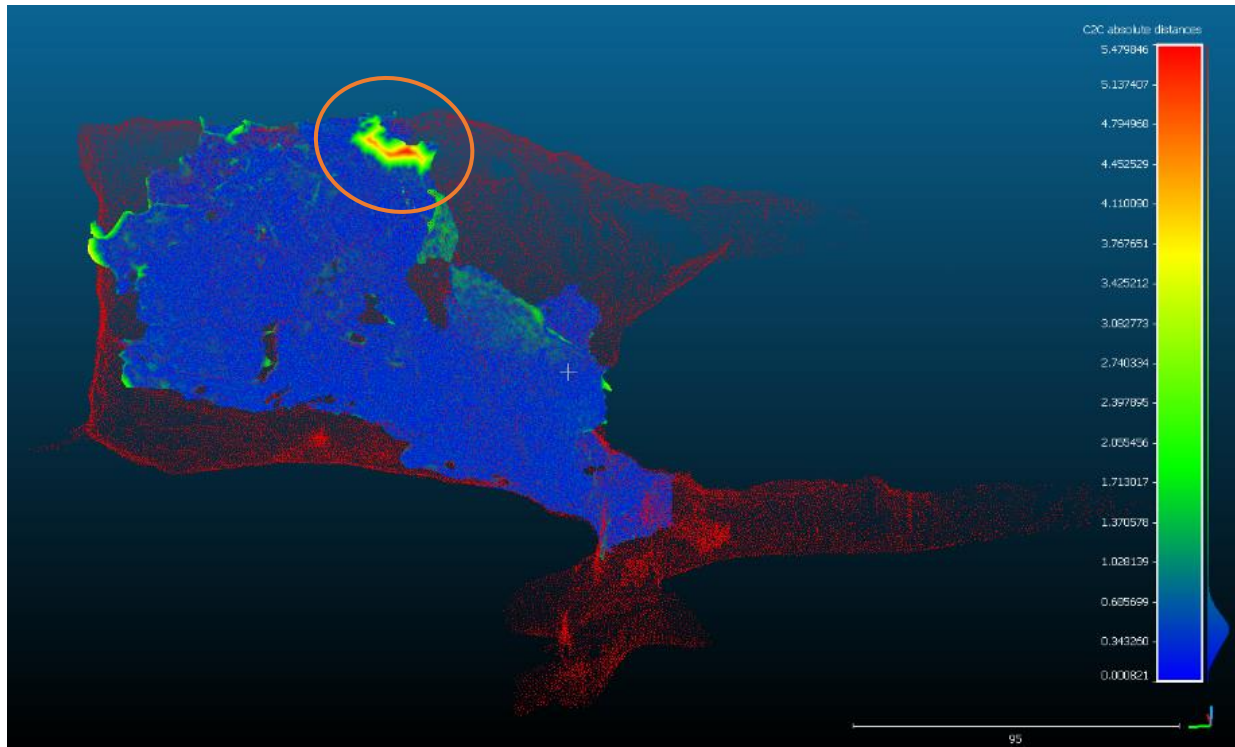
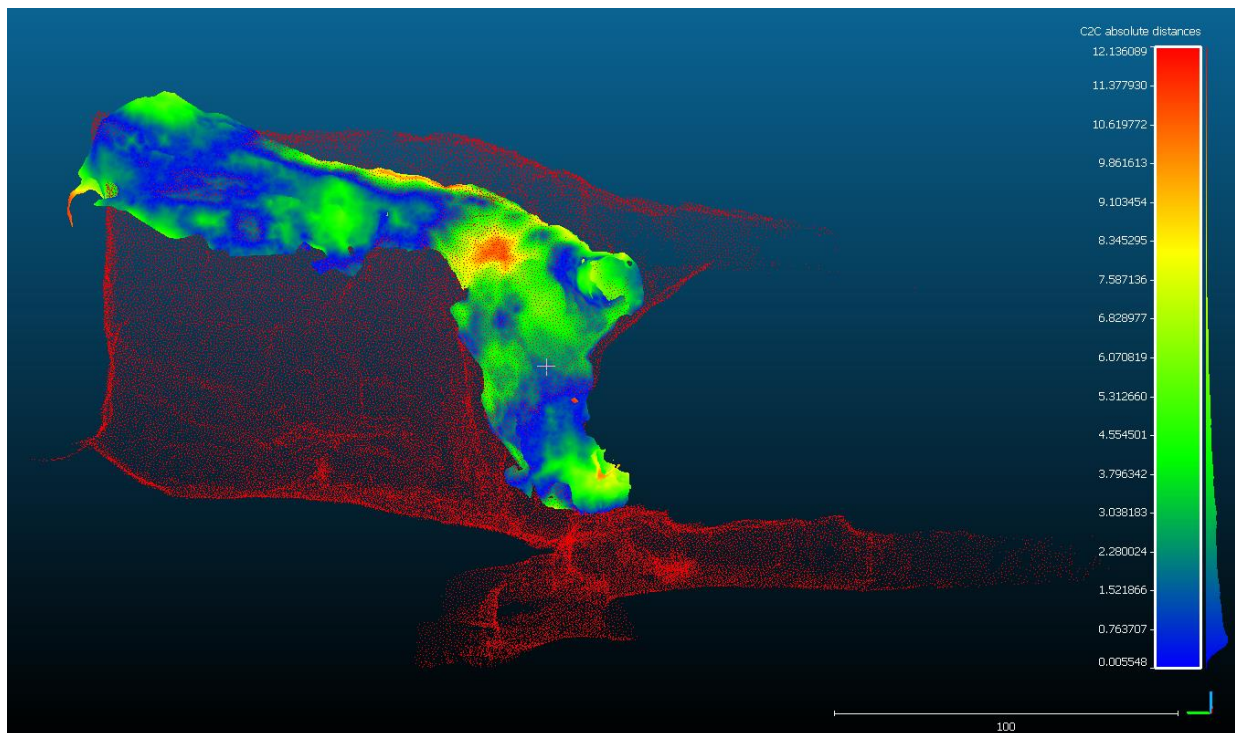


Figure 35: Colorized point cloud of the 735 stope measuring the difference from the Hovermap photogrammetric point cloud to the LiDAR reference scan. Circled is a region with high absolute distance near the outer boundary of the point cloud.

The photogrammetric point cloud of the 735 stope constructed from the Elios imagery did not align with the LiDAR reference point cloud. As seen in Figure 36, the roof of the photogrammetric model is distorted so that it deviates from the reference point cloud near the front of the stope. The regions of the point cloud with a high amount of error are not limited to the edges of the point cloud or to floating artifacts, as was commonly seen in other point clouds. In the imagery used to create the point cloud, it was clear that there were instances when the cage obstructed the view of the camera. This obstacle may have contributed to the decreased quality of the photogrammetric point cloud.



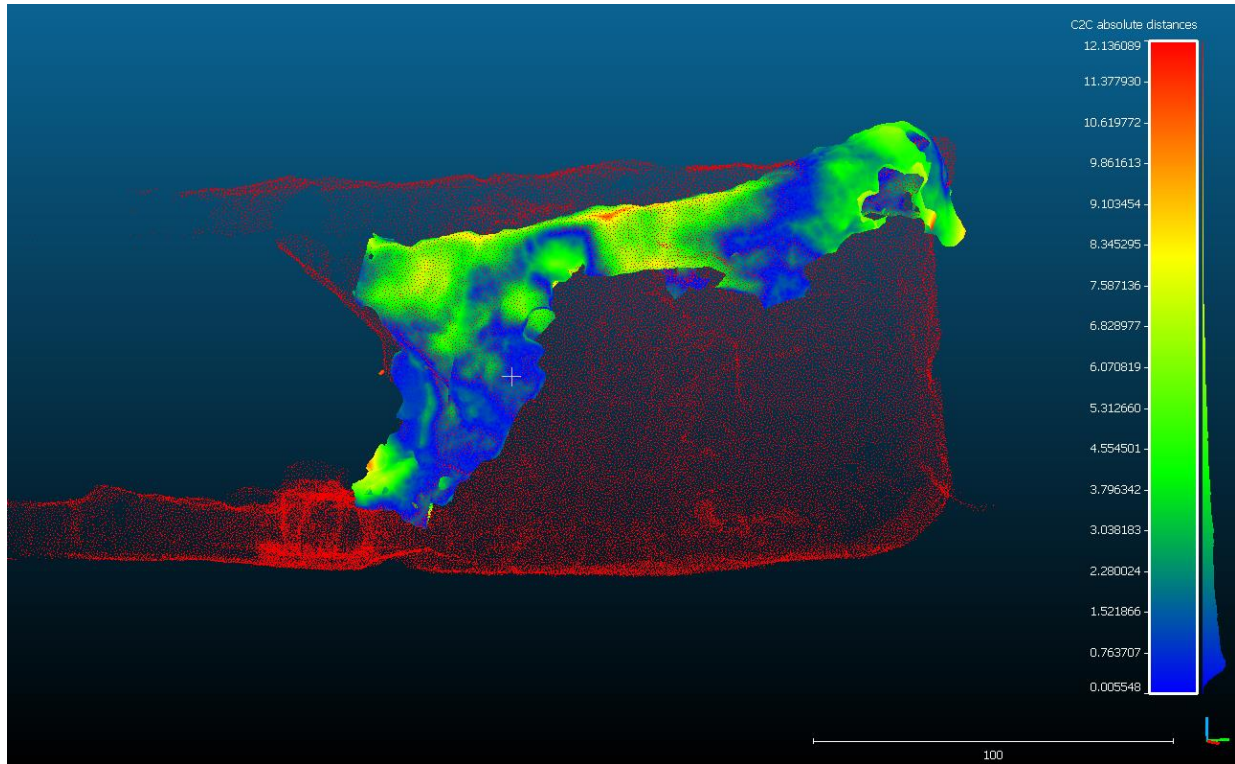


Figure 36: Colorized point cloud of the 735 stope measuring the difference from the Elios photogrammetric point cloud to the LiDAR reference scan. Distortion in the photogrammetric point cloud caused the roof of the stope to appear lower than in the LiDAR reference point cloud.

While limited in extent, the photogrammetric point cloud of the 735 stope constructed from the Ranger imagery (Figure 37) was reasonably complete with few holes or erroneous artifacts. The areas with the greatest differences from the reference point cloud were near the outer boundaries of the photogrammetric point cloud and near the entrance of the stope. Changes in the size and shape of the rock pile that acted as a barrier to the stope may have contributed to the higher degree of error in the area circled in Figure 37.

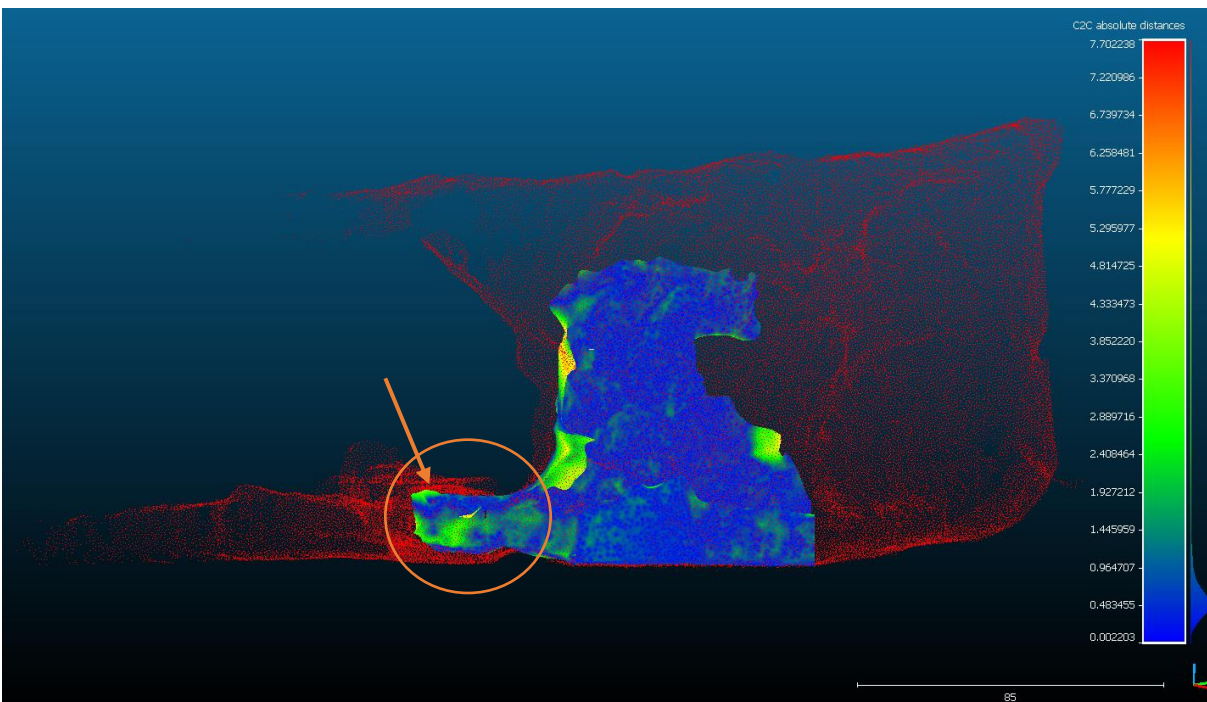
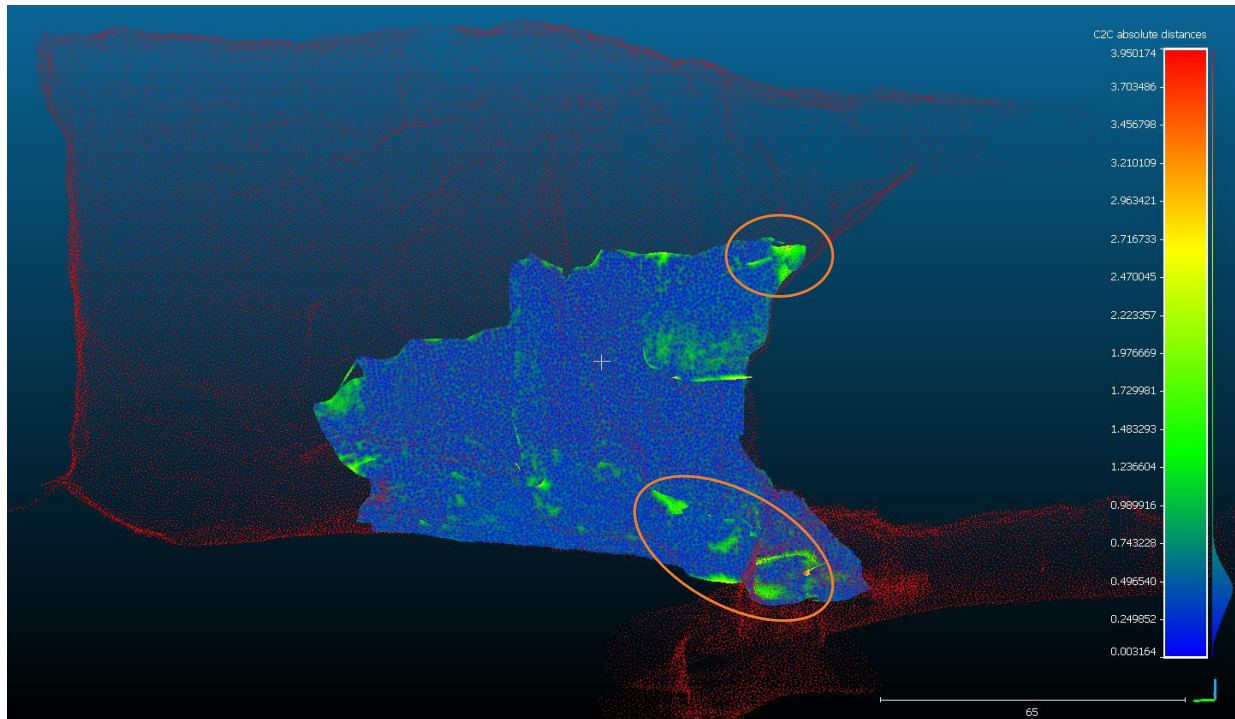


Figure 37: Colorized point cloud of the 735 stope measuring the difference from the Ranger photogrammetric point cloud to the LiDAR reference scan. Circled is a region with high absolute distance that may represent changes in the shape of the rock pile acting as a barrier to the stope between the time of the LiDAR scan and the time of the imagery collection.

The photogrammetric point cloud of the 735 stope built using imagery from Montana Tech's M100 (Figure 38) had the smallest mean error of the 735 stope models. Although the point cloud does not extend far from the entrance of the stope, there are very few holes and the model geometry aligns well with the reference point cloud. There are some areas in green (Figure 38, top) near the edges of the photogrammetric point cloud, similarly to the previous point clouds. Figure 38, bottom, shows the introduction of error that also may have been present in the Ranger point cloud in Figure 37. The greatest error in the photogrammetric point cloud occurs near the stope entrance where the barrier rock pile and barrier sign were likely moved between the times that the reference scan and photogrammetric imagery collection were performed. Unique to this point cloud, there is a spotted coloration pattern that is noticeable specifically in Figure 38, bottom. This is due to the reference LiDAR point cloud being sparser

than the photogrammetric point cloud; each blue spot is clustered around one of the red points in the LiDAR point cloud. The photogrammetry points located between each LiDAR point are colored more green in the photogrammetric point cloud because they are farther away from the points in the reference point cloud.



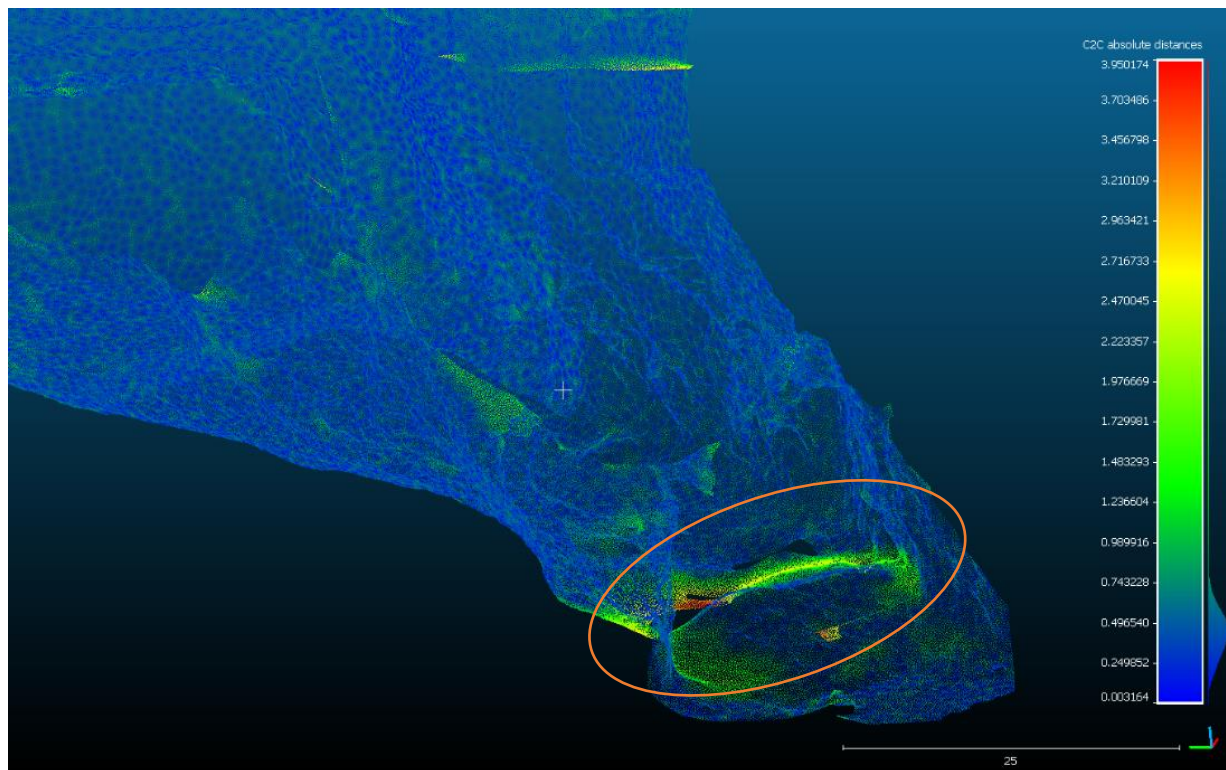


Figure 38: Colorized point cloud of the 735 stope measuring the difference from the Montana Tech M100 photogrammetric point cloud to the LiDAR reference scan. (Top) Circled are regions with high absolute distance near the boundary of the point cloud. (Bottom) Circled is the high absolute distance near the entrance of the stope is caused from changes in the shape of the barrier rock pile between the time of the LiDAR scan and the time of the imagery collection.

In many ways, a photogrammetric point cloud can only be as spatially accurate as the ground survey used during the georeferencing process. Although the error observed in the photogrammetric point clouds from this study is too large to be used for a highly-detailed spatial analysis, the point clouds are accurate enough to identify the location and general orientation of structural features. Because of the natural variability of geological features, the accuracy of a photogrammetric point cloud does not need to be as high as the accuracy of a survey-level scan. Additionally, because the aligning method was used to locate the photogrammetric point clouds in space, some accuracy may have been lost. The mean error may be partially indicative of how well the point clouds were aligned rather than how accurately the point clouds were built. Well-

placed and surveyed GCPs would likely have improved the spatial accuracy and decreased the mean error in these point clouds.

6. Conclusions and Recommendations

The purpose of this investigation was to develop a methodology for evaluating UAVs designed with enhanced navigation for the purpose of flying in inaccessible underground environments. Specifically, the ability of the UAVs to collect imagery sufficient for constructing 3D digital photogrammetric models was tested. The main requirements for successful data collection include maintaining a steady flight pattern without colliding with obstacles and the ability to carry a payload consisting of a high-resolution digital camera and high-powered LED lights. A systematic method for testing the flight capabilities of the platforms and quantitatively comparing the data collected was also developed. Through the course of the flight demonstrations, it was clear that there are viable UAV-based tools that not only can collect adequate photogrammetry data, but can also provide additional forms of data that can be utilized by mine personnel.

For obstacle detection and collision avoidance, the most commonly used method in these demonstrations was LiDAR-enabled simultaneous localization and mapping (SLAM), in which the vehicle creates a map of the surrounding environment using laser scans and locates itself within the map (Durrant-Whyte and Bailey, 2006). While three of the four teams utilized this system for enhanced navigation, only one team mounted the laser scanner so that it rotated while scanning. This addition allowed the UAV to scan its environment in 3D, vastly improving its ability to accurately map the environment and avoid obstacles in all directions. In an environment as transient as an underground mine, the ability to detect all obstacles on the fly is crucial to avoid a collision.

Many of the benefits of using UAVs for data collection in inaccessible environments were demonstrated in this investigation. Because UAVs are highly mobile, they can capture data

in locations that may otherwise be out of sight or obscured in a blindspot. Geologic or structural features can also be closely investigated using high-resolution cameras. From the video feed, areas of interest can be observed either during or after the flight. In most cases, data collection can be completed from just one access point, and requires little time to set up. Although the systems range in price, most are comparable or less expensive than traditional survey tools.

Although efforts were made to maintain consistent flight conditions between all of the demonstrations, this research was being conducted in an actively operating underground mine that was constantly evolving. Over the course of the investigation, access to certain areas of the mine changed and flights had to be completed in new locations. For this reason, not all of the groups flew all of the same sites, as initially planned. While there is some overlap between flight locations, many of the flights cannot be directly compared to the other teams. The quality of the photogrammetry data collected was also dependent on the ability of the pilot to understand and fly in a pattern conducive for photogrammetric modelling. While the preferred flight pattern was communicated to the pilots, there is a learning curve that may not have been picked up during the short visits. In the instances where the same pilot flew different systems (i.e. Hovermap and Elios), there was more opportunity for feedback to the pilot, resulting in higher quality data.

In traditional aerial photogrammetry, when the UAV is following a defined flight path, photographs are captured at a set interval to achieve the desired lateral overlap. In these flight demonstrations, the method used to collect photogrammetric data was to record a video from the UAV during the flight. In the post-processing, still photographs were extracted from the flight video at a defined rate, typically 1 frame/second. However, even when the flight appeared slow and steady in the video, the extracted images were often blurry or low resolution. These images were typically the ones that could not be matched to the neighboring images and were excluded

during the point cloud construction. While extracting frames more frequently from the flight video would potentially increase the likelihood of adequate overlap and clear images, large photosets can quickly become computationally intensive. Depending on the computer processing the point cloud, it may take several hours to build a single model. This may be acceptable for some users, however a standard desktop computer may not be able to run other programs for the duration of the model construction.

Despite these advantages, there still are shortcomings of using UAVs in these environments that need to be addressed. When operating UAVs beyond line-of-sight, the signal between the pilot and the UAV can be lost around corners, around obstacles, or at a distance. Depending on the software developed for the UAV, the UAV may return to the pilot, or this could result in a crash. Furthermore, a collision or crash continues to have high consequences and will typically result in the loss of the UAV. Until the autonomous abilities of the UAVs are consistently reliable, this form of data collection still requires a well-trained pilot. For photogrammetry data in particular, the lighting in the imagery is often inconsistent because of the movement and continuously changing distance of the UAV from the wall. In addition, the flight pattern required for collecting photogrammetry data is different than the flight pattern that would be used to autonomously explore an inaccessible opening. In this way, fully autonomous flight capabilities are less urgent than reliable obstacle avoidance systems.

The main obstacle that was faced during data processing was georeferencing the photogrammetric point clouds to the mine coordinate system. Ultimately, the system that was intended to be used was not redundant enough. Once the photogrammetric models were built, it was clear that several of the control points were not included within the models. In some cases, the flight videos that were used to build the point clouds did not image the control points, while

in other instances there was simply not enough overlap in the imagery. Because access to the stopes is prohibited, all GCPs were placed outside the stope and around the main draw point. To ensure that a photogrammetric model retains geometric accuracy, it is recommended to have GCPs spread out evenly throughout the model (Bemis et al., 2014). Methods have been developed to address this problem including shooting paint balls into a stope and surveying the mark left on a rock. The point can then be identified within the model and be correspondingly georeferenced.

The following are specific recommendations based on the results of this study meant to improve the procedure for underground photogrammetry data collection:

- Use a slow and steady flight pattern with intentional overlap of *at least* 60% to ensure photos will be correctly identified during model construction. For better results, use higher overlap.
- Specific flight patterns should be customized based on the geometry of each stope. The vertical strip flight pattern is not always possible, and a horizontal strip pattern may be more appropriate in laterally extensive stopes.
- Affix the lighting source to the UAV and maintain a consistent distance from the rib being imaged so the lighting conditions remain continuous in the imagery. When possible, turn off all other light sources throughout the flight.
- In addition to the pilot, have a second operator monitoring and controlling the camera. While it is often simpler to leave the camera facing forward so as not to confuse which direction the UAV is flying, the second operator can observe the live video feed to ensure the lighting, flight speed, and image overlap is sufficient.

- Use reflective tape to build a cross-hair target over existing survey control or ground control points where possible. The cross-hair creates a defined target that is easily identifiable in LiDAR point clouds and photogrammetric point clouds.
- Perform the LiDAR scan and photogrammetry image collection on the same day if a quantitative comparison is to be completed between the two point clouds.
- If not utilizing recommended method for georeferencing, ensure the method used has enough redundancy that control points will easily be identified in the imagery.

Although this study examined the accuracy of photogrammetric point clouds of stopes built using UAV-based imagery, there is room for continued investigation into the accuracy of photogrammetry in different scenarios. Mainly, the use of different GCP targets and placement should be explored to improve the spatial accuracy of the point clouds. Additional work could also be completed looking into the different photogrammetry software packages. Although one software was determined to be the most applicable for this investigation, the model building settings could be customized in each of the software to potentially achieve better results.

One immediate benefit of the research that was completed through the course of this project was the improved line of direct communication between UAV developers and underground mine corporations. Although the developers had an understanding of the general conditions to be expected underground and the applications for these technologies, many had spent little time in an actively operating underground mine. The experience of flying the UAVs throughout the underground mine emphasized the need for robust solutions to many of the challenges faced in that environment, including reliable obstacle avoidance and water resistance. Having a first-hand view of the potential applications of UAVs and how the collected data can be

used provided an opening for the developers to continue advancing their technologies with the mining industry in mind. These demonstrations also made it clear that the potential applications of UAVs as data collection tools in underground mines are numerous, and the continuing advancements in the technology of UAVs, LiDAR, and communication links will only improve autonomous and semi-autonomous flight capabilities.

7. References Cited

- ADAM Technology. (2010, September). *ADAM Technology Team Blog*. Retrieved from How Does Photogrammetry Work?: <https://www.adamtech.com.au/Blog/?p=102>
- Atlas Copco. (2007). *Sublevel Stopping Operation*. Retrieved April 11, 2019, from http://minewiki.engineering.queensu.ca/mediawiki/index.php/Sub-level_open_stopping#cite_note-AtlasCopco-0
- Azhari, F., Kiely, S., Sennersten, C., Lindley, C., Matuszak, M., & Hogwood, S. (2017). A comparison of sensors for underground void mapping by unmanned aerial vehicles. *Underground Mining Technology*, 419-430.
- Bamford, T., Esmaili, K., & Schoellig, A. P. (2017). Aerial Rock Fragmentation Analysis in Low-Light Condition Using UAV Technology. *Cornell University*.
- Barton, N. R., Lien, R., & Lunde, J. (1974). Engineering Classification of Rock Masses for the Design of Tunnel Support. *Rock Mechanics*, 6(4), 189-239.
- Becker, R. E., Galayda, L. J., & MacLaughlin, M. M. (2018). Digital photogrammetry software comparison for rock mass characterization. *American Rock Mechanics Association*.
- Bemis, S. P., Micklethwaite, S., Turner, D., James, M. R., Akciz, S., Thiele, S. T., & Bangash, H. A. (2014). Ground-based and UAV-based photogrammetry: A multi-scale, high-resolution mapping tool for structural geology and paleoseismology. *Journal of Structural Geology*, 163-178.
- Bentley. (2017). *ContextCapture Quick Start Guide*. Retrieved from <https://www.bentley.com/-/media/3dca09466818457fb9b7c72ada8e8e97.pdf>

- Benton, D. J., Chambers, A. J., Raffaldi, M. J., Finley, S. A., & Powers, M. J. (2016). Close-range photogrammetry in underground mining ground control. *Proceedings of SPIE*, 1-13.
- Bieniawski, Z. (1989). *Engineering Rock Mass Classifications*. New York: John Wiley and Sons, Inc.
- Cloud-to-Cloud Distance*. (2015, October 6). Retrieved from CloudCompare:
https://www.cloudcompare.org/doc/wiki/index.php?title=Cloud-to-Cloud_Distance
- Corrigan, F. (2018, September 06). *Time of Flight Camera Sensors On Drones and 10 Terrific Uses*. Retrieved from DroneZon: <https://www.dronezon.com/learn-about-drones-quadcopters/best-uses-for-time-of-flight-tof-camera-depth-sensor-technology-in-drones-or-ground-based/>
- Donovan, J., & Lebaron, A. (2009). A comparison of photogrammetry and laser scanning for the purpose of automated rock mass characterization. *43rd US Rock Mechanics Symposium*.
- Durrant-Whyte, H., & Bailey, T. (2006). Simultaneous Localization and Mapping: Part 1. *IEEE Robotics & Automation Magazine*, 99-108.
- Eisenbeiss, H., & Sauerbier, M. (2011, December). Investigation of UAV Systems and Flight Modes for Photogrammetric Applications. *The Photogrammetric Record*, 26(136), 400-421.
- Hamrin, H. (2001). Underground Mining Methods and Applications. In W. A. Hustrulid, & R. L. Bullock, *Underground Mining Methods: Engineering Fundamentals and International Case Studies* (pp. 3-14). Society for Mining, Metallurgy, and Exploration, Inc.
- Hoek, E. (1994). Strength of Rock and Rock Masses. *ISRM News Journal*, 2(2), 4-16.

- Hoek, E. (2007). *Practical Rock Engineering*. Retrieved from Rocscience:
<https://www.rocscience.com/learning/hoek-corner>
- Hovermap. (2019, March 12). Retrieved from Emesent: <https://emesent.io/products/hovermap/>
- LiDAR UK. (2019). *How does LiDAR work?* Retrieved from LiDAR UK: <http://www.lidar-uk.com/how-lidar-works/>
- Matthews, N. A. (2008). Aerial and Close-Range Photogrammetric Technology: Providing Resource Documentation, Interpretation, and Preservation. Technical Note 428. U.S. Department of the Interior, Bureau of Land Management, 42 pp.
- Mine Safety and Health Administration. (2018). *Code of Federal Regulations: Title 30 Mineral Resources*. . Office of the Federal Register.
- Novel, C., Keriven, R., Graindorge, P., & Poux, F. (2016). Comparing Aerial Photogrammetry and 3D Laser Scanning Methods for Creating 3D Models of Complex Objects. *A Bentley White Paper*.
- Paredes, J. A., Alvarex, F. J., Aguilera, T., & Villadangos, J. M. (2018). 3D Indoor Positioning of UAVs with Spread Spectrum Ultrasound and Time-of-Flight Cameras. *Sensors*.
- Pix4D. (2017, December 14). *Offline Getting Started and Manual*. Retrieved from Pix4D Support: <https://support.pix4d.com/hc/en-us/articles/204272989-Offline-Getting-Started-and-Manual-pdf->
- Preston, R., & Roy, J. (2017). Use of unmanned aerial vehicles to supplement conventional investigation methods for underground open void stability and mitigation. *Underground Mining Technology*, 609-616.
- Russell, E. A. (2018). UAV-Based Geotechnical Modeling and Mapping of an Inaccessible Underground Site. *Montana Tech*.

- Sabins, F. F. (1997). *Remote Sensing: Principles and Interpretation*. Long Grove: Waveland Press, Inc.
- Sturzenegger, M., & Stead, D. (2009). Close-range terrestrial digital photogrammetry and terrestrial laser scanning for discontinuity characterization on rock cuts. *Engineering Geology*, 106, 163-182.
- Tonon, F., & Kottenstette, J. T. (2006). Laser and Photogrammetric Methods for Rock Face Characterization. *GoldenRocks* (pp. 1-120). Golden: American Rock Mechanics Association.
- Turner, R. M., Bhagwat, N. P., Knoll, L. J., Russell, E. A., & MacLaughlin, M. M. (2018). Geotechnical Characterization of Underground Mine Excavations from UAV-Captured Photogrammetric and Thermal Imagery. *American Rock Mechanics Association*.
- Vallejo, L. I., & Ferrer, M. (2011). *Geological Engineering*. London: Taylor & Francis Group.
- Velodyne LiDAR, Inc. (2019, March 12). *Velodyne LiDAR Puck Lite Data Sheet*. Retrieved from Velodyne LiDAR: <https://velodynelidar.com/vlp-16-lite.html>
- Villaescusa, E. (2014). *Geotechnical Design for Sublevel Open Stoping*. Boca Raton: Taylor & Francis Group.
- Westoby, M., Brasington, J., Glasser, N., Hambrey, M., & Reynolds, J. (2012). 'Structure-from-Motion' photogrammetry: A low-cost, effective tool for geoscience applications. *Geomorphology*, 300-314.

8. Appendix A: Underground Flight Demonstration Notes

| Team: Emesent | | | | | | | | |
|---------------|----------|--------|-------------------------|------------------|----------|-----------------|------------------------|----------------------|
| Date | Flight # | Time | Platform | Flight Location | Length | Flight Mode | Lighting | Imaging Device |
| 15 July 2018 | 1 | - | <i>Standard Payload</i> | Surface Lawn | 2 min | Tap-to-Fly | - | - |
| | 2 | - | <i>Standard Payload</i> | Surface Wash Bay | 3 min | Assisted Flight | - | - |
| | 3 | - | <i>Standard Payload</i> | Surface Wash Bay | 5 min | Assisted Flight | - | - |
| 16 July 2018 | 1 | - | <i>Standard Payload</i> | Lower SAM | 5 min | Assisted Flight | On-board LED (forward) | Zenmuse X3 |
| | 2 | - | <i>Standard Payload</i> | Lower SAM | 3 min | Tap-to-Fly | On-board LED (forward) | - |
| 17 July 2018 | 1 | 10:00a | <i>Mining Payload</i> | Lower SAM | 1.5 min | - | On-board LED (forward) | Zenmuse X3 and GoPro |
| | 2 | 10:30a | <i>Mining Payload</i> | Lower SAM | 2 min | - | On-board LED (forward) | Zenmuse X3 and GoPro |
| | 3 | 11:30a | <i>Mining Payload</i> | Lower SAM | 5 min | Tap-to-Fly | On-board LED (forward) | Zenmuse X3 and GoPro |
| | 4 | 2:00p | <i>Mining Payload</i> | 995-480 Drift | 3 min | Assisted Flight | On-board LED (forward) | Zenmuse X3 and GoPro |
| | 5 | 2:15p | <i>Mining Payload</i> | 995-480 Drift | 9 min | Tap-to-Fly | On-board LED (forward) | Zenmuse X3 and GoPro |
| | 6 | 4:00p | <i>Mining Payload</i> | Lower SAM | 11.5 min | Tap-to-Fly | On-board LED (forward) | Zenmuse X3 and GoPro |
| | 7 | 4:15p | <i>Mining Payload</i> | Lower SAM | 5.5 min | Tap-to-Fly | On-board LED (forward) | Zenmuse X3 and GoPro |
| 18 July 2018 | 1 | - | <i>Mining Payload</i> | 735-102 Stope | 5 min | Assisted Flight | On-board LED (forward) | GoPro |
| | 2 | - | <i>Mining Payload</i> | 735-102 Stope | 7.5 min | Tap-to-Fly | On-board LED (forward) | GoPro |
| | 3 | - | <i>Standard Payload</i> | 895-102 Stope | 3.5 min | Assisted Flight | Handheld LED | - |
| | 4 | - | <i>Standard Payload</i> | 895-102 Stope | 7 min | Assisted Flight | On-board LED (forward) | Zenmuse X3 |
| | 5 | - | <i>Standard Payload</i> | 735-102 Stope | 8.5 min | Assisted Flight | On-board LED (forward) | Zenmuse X3 |
| 19 July 2018 | 1 | - | <i>Standard Payload</i> | 895-945 Stope | 5 min | Assisted Flight | Handheld LED | - |
| | 2 | - | <i>Standard Payload</i> | 735-102 Stope | 2 min | Posemap | Handheld LED | - |
| | 3 | - | <i>Standard Payload</i> | 735-102 Stope | 3 min | Posemap | Handheld LED | - |
| | 4 | - | <i>Standard Payload</i> | 735-102 Stope | 4 min | Posemap | Handheld LED | - |

| Team: Near Earth Autonomy | | | | | | | | |
|---------------------------|----------|--------|----------|--------------------|---------|-------------|------------------------------|----------------|
| Date | Flight # | Time | Platform | Flight Location | Length | Flight Mode | Lighting | Imaging Device |
| 31 July 2018 | 1 | 10:30a | M2 | Lower SAM | 0.5 min | P-mode | 2 key chain lights (forward) | Zenmuse X3 |
| | 2 | 10:50a | M2 | Lower SAM | 4 min | F-mode | 2 key chain lights (forward) | - |
| | 3 | 11:08a | M2 | Lower SAM | 1 min | F-mode | 2 key chain lights (forward) | - |
| | 4 | 11:15a | M2 | Lower SAM | 6 min | F-mode | 2 key chain lights (forward) | - |
| | 5 | 11:35a | M2 | Lower SAM | 0.5 min | F-mode | 2 key chain lights (forward) | Zenmuse X3 |
| | 5b | 11:40a | M2 | Lower SAM | 1 min | F-mode | Handheld LED | Zenmuse X3 |
| | 6 | 11:50a | M2 | Lower SAM | 2 min | F-mode | Handheld LED | GoPro |
| | 7 | 12:13p | M2 | Lower SAM | 0.5 min | F-mode | Handheld LED | GoPro |
| | 7b | 12:18p | M2 | Lower SAM | 3 min | F-mode | Handheld LED | GoPro |
| | 7c | 12:25p | M2 | Lower SAM | 3 min | F-mode | Handheld LED | GoPro |
| | 8a | 2:00p | M2 | 995 Drift | 2 min | F-mode | Handheld LED | GoPro |
| | 8b | 2:08p | M2 | 995 Drift | 3.5 min | F-mode | Handheld LED | GoPro |
| | 9 | 2:30p | M2 | 995 Drift | 3 min | F-mode | Handheld LED | GoPro |
| | 10 | 2:40p | M2 | 995 Drift | 2.5 min | F-mode | Handheld LED | GoPro |
| 01 Aug 2018 | 1 | 11:01a | M2 | Surface Wash Bay | 0.5 min | F-mode | - | - |
| | 2 | 1:30p | M2 | 995 to 895 Drift | 10 min | F-mode | - | - |
| | 3 | 1:54p | M2 | 895-945 Stope Scan | 2 min | F-mode | - | - |

| Team: Inkonova | | | | | | | | |
|----------------|----------|--------|------------|-----------------|---------|-------------------|------------------------|----------------|
| Date | Flight # | Time | Platform | Flight Location | Length | Flight Mode | Lighting | Imaging Device |
| 26 Aug 2018 | 1 | 12:45p | Batonomous | 895 Drift | 3 min | Waypoint | On-board LED (forward) | - |
| | 2 | 1:05p | Batonomous | 895 Drift | 2 min | Batonomous | On-board LED (forward) | - |
| | 3a | 2:05p | Ranger | 895 Drift | 2 min | Manual w/ goggles | On-board LED (forward) | GoPro Hero 3+ |
| | 3b | 2:15p | Ranger | 895 Drift | 1.5 min | Manual w/ goggles | On-board LED (forward) | GoPro Hero 3+ |
| | 4 | 2:18p | Ranger | 895 Drift | 1.5 min | Manual w/ goggles | On-board LED (forward) | GoPro Hero 3+ |
| | 5 | 2:35p | Ranger | 895 Drift | 1.5 min | Manual w/ goggles | On-board LED (forward) | GoPro Hero 3+ |

| | | | | | | | | |
|-------------------|---|--------|----------|---------------------|---------|-------------------------------------|---------------------------|------------------|
| | 6 | 2:40p | Ranger | 895 Drift | 1.5 min | Manual w/ collision avoidance | On-board LED (forward) | GoPro Hero 3+ |
| | 7 | 2:50p | Ranger | 895 Drift | 1 min | Manual w/ collision avoidance | On-board LED (forward) | GoPro Hero 3+ |
| | 8 | 2:55p | Ranger | 895 Drift | 0.5 min | Manual w/ collision avoidance | On-board LED (forward) | GoPro Hero 3+ |
| 27 Aug 2018 | 1 | 9:00a | Batomous | Surface Wash Bay | 1.5 min | Manual | On-board LED (forward) | - |
| | 2 | 9:30a | Batomous | Surface Wash Bay | 2 min | Manual | On-board LED (forward) | - |
| | 3 | 12:40p | Batomous | 895 Drift | 3 min | Manual w/ collision avoidance | On-board LED (forward) | - |
| | 4 | 1:12p | Batomous | 895 Drift | 0.5 min | Manual | Handheld LED | - |
| | 5 | 2:20p | Ranger | 750-735 Stope | 5 min | Manual | On-board LED (forward) | GoPro Hero 3+ |
| | 6 | 2:52p | Ranger | 750-735 Stope | 1 min | Manual w/ goggles | On-board LED (forward) | GoPro Hero 3+ |
| | 7 | 2:53p | Ranger | 750-735 Stope | 2.5 min | Manual w/ goggles | On-board LED (forward) | GoPro Hero 3+ |
| | 8 | 3:23p | Ranger | 750-735 Stope | 1.5 min | Manual w/ goggles | On-board LED (forward) | GoPro Hero 3+ |
| | 9 | 3:26p | Ranger | 750 Drift | 3 min | Manual w/ goggles | On-board LED (forward) | GoPro Hero 3+ |

| Team: Flyability | | | | | | | | |
|--------------------|----------|--------|-------------|-----------------|---------|-------------|-----------------|----------------|
| Date | Flight # | Time | Platform | Flight Location | Length | Flight Mode | Lighting | Imaging Device |
| 13 Sept 2018 | 1 | 10:44a | Undisclosed | 895 Drift | 7 min | Manual | On-board LED | 1080 HD |
| | 2 | 11:16a | Elios | 895-102 Stope | 7.5 min | Manual | On-board LED | 1080 HD |
| | 3 | 12:04p | Elios | 750-735 Stope | 5 min | Manual | On-board LED | 1080 HD |
| | 4 | 12:31p | Elios | 750-735 Stope | 6 min | Manual | On-board LED | 1080 HD |
| | 5 | 1:03p | Elios | 750-735 Stope | 5 min | Manual | On-board LED | 1080 HD |
| | 6 | 1:24p | Elios | 750-735 Stope | 6.5 min | Manual | On-board LED | 1080 HD |
| | 7 | 1:35p | Elios | 735 Drift | 6.5 min | Manual | On-board LED | 1080 HD |
| | 8 | 1:53p | Undisclosed | 735 Drift | 6 min | Manual | On-board LED | 1080 HD |
| | 9 | 2:10p | Undisclosed | 735 Drift | 8 min | Manual | On-board LED | 1080 HD |
| | 10 | 2:20p | Elios | 735 Drift | 5 min | Manual | On-board LED | 1080 HD |
| | 11 | 2:55p | Undisclosed | 995-945 Stope | 1 min | Manual | On-board LED | 1080 HD |

| | | | | | | | | |
|--------------------|---|--------|-------------|-----------------------|-------|--------|--------------|---------|
| 14 Sept 2018 | 1 | 10:45a | Undisclosed | 895-102 Stope | 2 min | Manual | On-board LED | 1080 HD |
| | 2 | 10:55a | Undisclosed | 895-102 Stope | 3 min | Manual | On-board LED | 1080 HD |
| | 3 | 12:00p | Elios | 895 Ventilation Raise | 5 min | Manual | On-board LED | 1080 HD |
| | 4 | 12:15p | Undisclosed | 895 Ventilation Raise | 5 min | Manual | On-board LED | 1080 HD |
| | 5 | 1:20p | Undisclosed | 735-102 Stope | 5 min | Manual | On-board LED | 1080 HD |
| | 6 | 1:37p | Undisclosed | 735-102 Stope | 6 min | Manual | On-board LED | 1080 HD |
| | 7 | 1:50p | Elios | 735 Drift | 5 min | Manual | On-board LED | 1080 HD |

| Supplementary Flights - Team: Unmanned Aerial Services | | | | | | | | |
|--|----------|--------|------------------------------|-----------------|---------|-----------------|------------------------------------|----------------|
| Date | Flight # | Time | Platform | Flight Location | Length | Flight Mode | Lighting | Imaging Device |
| 10 Sep 2018 | 1 | 8:45a | Elios | 895-102 Stope | - | Manual | On-board LED, handheld LED | 1080 HD |
| | 2 | 10:15a | Hovermap <i>Std.</i> Payload | 895-102 Stope | - | Assisted Flight | On-board LED (right) | Zenmuse X3 |
| | 3 | 10:20a | Hovermap <i>Std.</i> Payload | 895-102 Stope | - | Assisted Flight | On-board LED (right) | Zenmuse X3 |
| | 4 | - | Hovermap <i>Std.</i> Payload | 895-102 Stope | - | Assisted Flight | - | Zenmuse XT |
| | 5 | - | Hovermap <i>Std.</i> Payload | 995-945 Stope | - | Assisted Flight | - | - |
| | 6 | - | Hovermap <i>Std.</i> Payload | 995-945 Stope | 5 min | Assisted Flight | On-board LED (right), handheld LED | Zenmuse X3 |
| 11 Sep 2018 | 1 | - | Hovermap <i>Std.</i> Payload | 995-945 Stope | - | Assisted Flight | On-board LED (right), handheld LED | - |
| | 2 | - | Hovermap <i>Std.</i> Payload | 995-102 Stope | 9.5 min | Assisted Flight | On-board LED (right), handheld LED | Zenmuse X3 |
| | 3 | - | Hovermap <i>Std.</i> Payload | 995-102 Stope | - | Assisted Flight | Handheld LED | Zenmuse XT |
| | 4 | - | Hovermap <i>Std.</i> Payload | 995-102 Stope | - | Assisted Flight | On-board LED | Mica Red Edge |
| | 5 | 3:05p | Hovermap <i>Std.</i> Payload | 750-735 Stope | 7 min | Assisted Flight | On-board LED, handheld LED | Zenmuse X3 |
| | 6 | 3:30p | Hovermap <i>Std.</i> Payload | 750-735 Stope | 7 min | Assisted Flight | On-board LED, handheld LED | Zenmuse X3 |
| | 7 | - | Hovermap <i>Std.</i> Payload | 750-735 Stope | - | Assisted Flight | Handheld LED | Zenmuse XT |
| | 8 | - | Hovermap <i>Std.</i> Payload | 750-735 Stope | - | Assisted Flight | Handheld LED | Zenmuse XT |

| Supplementary Flights - Team: Montana Tech | | | | | | | | |
|--|----------|--------|-------------|-----------------|---------|-----------------|--------------|----------------|
| Date | Flight # | Time | Platform | Flight Location | Length | Flight Mode | Lighting | Imaging Device |
| 09 Aug 2018 | 6 | - | M100 | 815-945 Stope | 5 min | Guidance Assist | On-board LED | Zenmuse X3 |
| | 7 | - | M100 | 815-945 Stope | 6.5 min | Guidance Assist | On-board LED | Zenmuse X3 |
| | 8 | - | M100 | 815-945 Stope | 7.5 min | Guidance Assist | On-board LED | Zenmuse X3 |
| 31 Aug 2018 | 1 | 9:45a | M100 | 735 Stope | 1.5 min | Guidance Assist | On-board LED | Zenmuse X3 |
| | 2 | 10:05a | M100 | 735 Stope | 5 min | Guidance Assist | On-board LED | Zenmuse X3 |
| | 3 | 10:25a | M100 | 735 Stope | 7.5 min | Guidance Assist | On-board LED | Zenmuse X3 |
| | 4 | 10:45a | M100 | 735 Stope | 3.5 min | Guidance Assist | On-board LED | Zenmuse X3 |
| | 5 | 10:55a | M100 | 735 Stope | 6.5 min | Guidance Assist | On-board LED | Zenmuse X3 |
| | 6 | 11:20a | Black Widow | 750 Run-around | 1.5 min | Atti | Handheld LED | SJ 4000 |
| | 7 | 11:45a | Black Widow | 750 Run-around | 2 min | Atti | Buggy lights | SJ 4000 |

9. Appendix B: Qualitative Evaluation Score Sheets

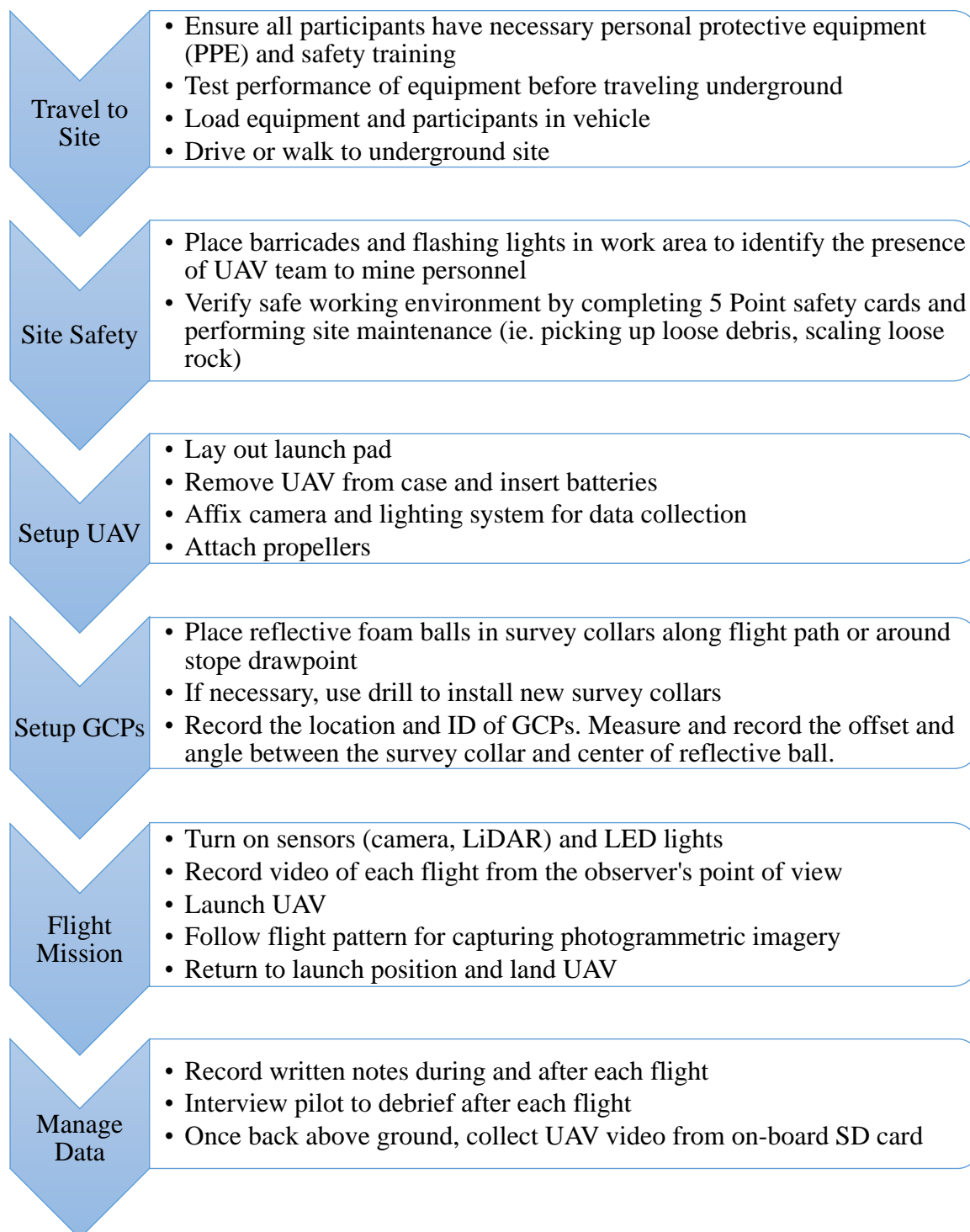
PHOTOGRAMMETRIC 3D POINT CLOUD / MODEL EVALUATION SCORE SHEET

| | Completeness | | | | Score (1-10) | Detail | | | | Score (1-10) | Comments |
|-----|-------------------------------------|-------------------------------------|-------------------------------------|-----------------------------|--------------|-------------------------------------|-------------------------------------|-------------------------------------|---|--------------|---|
| | Poor | Mid | Good | | | Poor | Mid | Good | | | |
| 1_1 | <input checked="" type="checkbox"/> | <input type="checkbox"/> | <input type="checkbox"/> | Continuous surface | 2 | <input type="checkbox"/> | <input checked="" type="checkbox"/> | <input type="checkbox"/> | Surface texture | 5 | |
| | <input checked="" type="checkbox"/> | <input type="checkbox"/> | <input type="checkbox"/> | Realistic geometry | | <input type="checkbox"/> | <input checked="" type="checkbox"/> | <input type="checkbox"/> | Surface resolution | | |
| | <input checked="" type="checkbox"/> | <input type="checkbox"/> | <input type="checkbox"/> | Lack of excessive artifacts | | <input type="checkbox"/> | <input checked="" type="checkbox"/> | <input type="checkbox"/> | Visible discontinuities | | |
| | <input type="checkbox"/> | <input checked="" type="checkbox"/> | <input type="checkbox"/> | Lack of distortion | | <input checked="" type="checkbox"/> | <input type="checkbox"/> | <input type="checkbox"/> | Recognizable features | | |
| 1_2 | <input checked="" type="checkbox"/> | <input checked="" type="checkbox"/> | <input type="checkbox"/> | Continuous surface | 4 | <input type="checkbox"/> | <input type="checkbox"/> | <input checked="" type="checkbox"/> | Surface texture | 9 | |
| | <input type="checkbox"/> | <input checked="" type="checkbox"/> | <input type="checkbox"/> | Realistic geometry | | <input type="checkbox"/> | <input type="checkbox"/> | <input checked="" type="checkbox"/> | Surface resolution | | |
| | <input checked="" type="checkbox"/> | <input checked="" type="checkbox"/> | <input type="checkbox"/> | Lack of excessive artifacts | | <input type="checkbox"/> | <input type="checkbox"/> | <input checked="" type="checkbox"/> | Visible discontinuities | | |
| | <input type="checkbox"/> | <input checked="" type="checkbox"/> | <input type="checkbox"/> | Lack of distortion | | <input type="checkbox"/> | <input type="checkbox"/> | <input checked="" type="checkbox"/> | Recognizable features | | |
| 1_3 | <input type="checkbox"/> | <input type="checkbox"/> | <input checked="" type="checkbox"/> | Continuous surface | 9 | <input type="checkbox"/> | <input type="checkbox"/> | <input checked="" type="checkbox"/> | Surface texture | 9 | |
| | <input type="checkbox"/> | <input type="checkbox"/> | <input checked="" type="checkbox"/> | Realistic geometry | | <input type="checkbox"/> | <input type="checkbox"/> | <input checked="" type="checkbox"/> | Surface resolution | | |
| | <input type="checkbox"/> | <input type="checkbox"/> | <input checked="" type="checkbox"/> | Lack of excessive artifacts | | <input type="checkbox"/> | <input type="checkbox"/> | <input checked="" type="checkbox"/> | Visible discontinuities | | |
| | <input type="checkbox"/> | <input type="checkbox"/> | <input checked="" type="checkbox"/> | Lack of distortion | | <input type="checkbox"/> | <input type="checkbox"/> | <input checked="" type="checkbox"/> | Recognizable features | | |
| 2_1 | <input type="checkbox"/> | <input checked="" type="checkbox"/> | <input type="checkbox"/> | Continuous surface | 8 | <input type="checkbox"/> | <input checked="" type="checkbox"/> | <input checked="" type="checkbox"/> | Surface texture | 7 | both sides of slope but more small holes |
| | <input type="checkbox"/> | <input type="checkbox"/> | <input checked="" type="checkbox"/> | Realistic geometry | | <input type="checkbox"/> | <input checked="" type="checkbox"/> | <input checked="" type="checkbox"/> | Surface resolution | | |
| | <input type="checkbox"/> | <input type="checkbox"/> | <input checked="" type="checkbox"/> | Lack of excessive artifacts | | <input type="checkbox"/> | <input checked="" type="checkbox"/> | <input checked="" type="checkbox"/> | Visible discontinuities | | |
| | <input type="checkbox"/> | <input type="checkbox"/> | <input checked="" type="checkbox"/> | Lack of distortion | | <input type="checkbox"/> | <input checked="" type="checkbox"/> | <input checked="" type="checkbox"/> | Recognizable features | | |
| 2_2 | <input type="checkbox"/> | <input checked="" type="checkbox"/> | <input type="checkbox"/> | Continuous surface | 7 | <input checked="" type="checkbox"/> | <input type="checkbox"/> | <input type="checkbox"/> | Surface texture | 3 | only one side of slope but fewer holes, discontinuities more visible zoomed out |
| | <input type="checkbox"/> | <input type="checkbox"/> | <input checked="" type="checkbox"/> | Realistic geometry | | <input checked="" type="checkbox"/> | <input type="checkbox"/> | <input type="checkbox"/> | Surface resolution | | |
| | <input type="checkbox"/> | <input type="checkbox"/> | <input checked="" type="checkbox"/> | Lack of excessive artifacts | | <input checked="" type="checkbox"/> | <input type="checkbox"/> | <input type="checkbox"/> | Visible discontinuities | | |
| | <input type="checkbox"/> | <input type="checkbox"/> | <input checked="" type="checkbox"/> | Lack of distortion | | <input type="checkbox"/> | <input checked="" type="checkbox"/> | <input type="checkbox"/> | Recognizable features | | |
| 2_3 | <input type="checkbox"/> | <input type="checkbox"/> | <input checked="" type="checkbox"/> | Continuous surface | 10 | <input type="checkbox"/> | <input type="checkbox"/> | <input checked="" type="checkbox"/> | Surface texture | 10 | super detailed, very complete surface texture a bit smoothed? |
| | <input type="checkbox"/> | <input type="checkbox"/> | <input checked="" type="checkbox"/> | Realistic geometry | | <input type="checkbox"/> | <input type="checkbox"/> | <input checked="" type="checkbox"/> | Surface resolution | | |
| | <input type="checkbox"/> | <input type="checkbox"/> | <input checked="" type="checkbox"/> | Lack of excessive artifacts | | <input type="checkbox"/> | <input type="checkbox"/> | <input checked="" type="checkbox"/> | Visible discontinuities | | |
| | <input type="checkbox"/> | <input type="checkbox"/> | <input checked="" type="checkbox"/> | Lack of distortion | | <input type="checkbox"/> | <input type="checkbox"/> | <input checked="" type="checkbox"/> | Recognizable features | | |
| 3_1 | <input type="checkbox"/> | <input checked="" type="checkbox"/> | <input type="checkbox"/> | Continuous surface | 6 | <input type="checkbox"/> | <input checked="" type="checkbox"/> | <input type="checkbox"/> | Surface texture | 5 | color difference picked up well |
| | <input checked="" type="checkbox"/> | <input type="checkbox"/> | <input type="checkbox"/> | Realistic geometry | | <input checked="" type="checkbox"/> | <input type="checkbox"/> | <input type="checkbox"/> | Surface resolution | | |
| | <input checked="" type="checkbox"/> | <input type="checkbox"/> | <input type="checkbox"/> | Lack of excessive artifacts | | <input type="checkbox"/> | <input checked="" type="checkbox"/> | <input type="checkbox"/> | Visible discontinuities | | |
| | <input checked="" type="checkbox"/> | <input checked="" type="checkbox"/> | <input type="checkbox"/> | Lack of distortion - buried | | <input type="checkbox"/> | <input checked="" type="checkbox"/> | <input type="checkbox"/> | Recognizable features | | |
| 3_2 | <input type="checkbox"/> | <input type="checkbox"/> | <input checked="" type="checkbox"/> | Continuous surface | 10 | <input type="checkbox"/> | <input type="checkbox"/> | <input checked="" type="checkbox"/> | Surface texture | 8 | 1 side of drift |
| | <input type="checkbox"/> | <input type="checkbox"/> | <input checked="" type="checkbox"/> | Realistic geometry | | <input type="checkbox"/> | <input type="checkbox"/> | <input checked="" type="checkbox"/> | Surface resolution | | |
| | <input type="checkbox"/> | <input type="checkbox"/> | <input checked="" type="checkbox"/> | Lack of excessive artifacts | | <input type="checkbox"/> | <input checked="" type="checkbox"/> | <input type="checkbox"/> | Visible discontinuities | | |
| | <input type="checkbox"/> | <input type="checkbox"/> | <input checked="" type="checkbox"/> | Lack of distortion | | <input type="checkbox"/> | <input type="checkbox"/> | <input checked="" type="checkbox"/> | Recognizable features - people, bolt plates | | |
| 3_3 | <input type="checkbox"/> | <input type="checkbox"/> | <input checked="" type="checkbox"/> | Continuous surface | 10 | <input type="checkbox"/> | <input type="checkbox"/> | <input checked="" type="checkbox"/> | Surface texture | 10 | super detailed, can read marks painted on walls, recognize specific people |
| | <input type="checkbox"/> | <input type="checkbox"/> | <input checked="" type="checkbox"/> | Realistic geometry | | <input type="checkbox"/> | <input type="checkbox"/> | <input checked="" type="checkbox"/> | Surface resolution | | |
| | <input type="checkbox"/> | <input type="checkbox"/> | <input checked="" type="checkbox"/> | Lack of excessive artifacts | | <input type="checkbox"/> | <input type="checkbox"/> | <input checked="" type="checkbox"/> | Visible discontinuities | | |
| | <input type="checkbox"/> | <input type="checkbox"/> | <input checked="" type="checkbox"/> | Lack of distortion | | <input type="checkbox"/> | <input type="checkbox"/> | <input checked="" type="checkbox"/> | Recognizable features | | |
| 4_1 | <input checked="" type="checkbox"/> | <input checked="" type="checkbox"/> | <input type="checkbox"/> | Continuous surface | 7 | <input type="checkbox"/> | <input checked="" type="checkbox"/> | <input type="checkbox"/> | Surface texture | 4 | |
| | <input type="checkbox"/> | <input checked="" type="checkbox"/> | <input type="checkbox"/> | Realistic geometry | | <input checked="" type="checkbox"/> | <input type="checkbox"/> | <input type="checkbox"/> | Surface resolution | | |
| | <input type="checkbox"/> | <input type="checkbox"/> | <input checked="" type="checkbox"/> | Lack of excessive artifacts | | <input type="checkbox"/> | <input checked="" type="checkbox"/> | <input type="checkbox"/> | Visible discontinuities | | |
| | <input type="checkbox"/> | <input type="checkbox"/> | <input checked="" type="checkbox"/> | Lack of distortion | | <input type="checkbox"/> | <input checked="" type="checkbox"/> | <input type="checkbox"/> | Recognizable features | | |
| 4_2 | <input type="checkbox"/> | <input checked="" type="checkbox"/> | <input type="checkbox"/> | Continuous surface | 8.5 | <input type="checkbox"/> | <input type="checkbox"/> | <input checked="" type="checkbox"/> | Surface texture | 9 | |
| | <input type="checkbox"/> | <input type="checkbox"/> | <input checked="" type="checkbox"/> | Realistic geometry | | <input type="checkbox"/> | <input type="checkbox"/> | <input checked="" type="checkbox"/> | Surface resolution | | |
| | <input type="checkbox"/> | <input type="checkbox"/> | <input checked="" type="checkbox"/> | Lack of excessive artifacts | | <input type="checkbox"/> | <input type="checkbox"/> | <input checked="" type="checkbox"/> | Visible discontinuities | | |
| | <input type="checkbox"/> | <input type="checkbox"/> | <input checked="" type="checkbox"/> | Lack of distortion | | <input type="checkbox"/> | <input type="checkbox"/> | <input checked="" type="checkbox"/> | Recognizable features | | |
| 4_3 | <input type="checkbox"/> | <input type="checkbox"/> | <input checked="" type="checkbox"/> | Continuous surface | 7 | <input type="checkbox"/> | <input type="checkbox"/> | <input checked="" type="checkbox"/> | Surface texture | 9 | |
| | <input checked="" type="checkbox"/> | <input checked="" type="checkbox"/> | <input type="checkbox"/> | Realistic geometry | | <input type="checkbox"/> | <input type="checkbox"/> | <input checked="" type="checkbox"/> | Surface resolution | | |
| | <input type="checkbox"/> | <input type="checkbox"/> | <input checked="" type="checkbox"/> | Lack of excessive artifacts | | <input type="checkbox"/> | <input type="checkbox"/> | <input checked="" type="checkbox"/> | Visible discontinuities | | |
| | <input type="checkbox"/> | <input type="checkbox"/> | <input checked="" type="checkbox"/> | Lack of distortion | | <input type="checkbox"/> | <input type="checkbox"/> | <input checked="" type="checkbox"/> | Recognizable features | | |

PHOTOGRAMMETRIC 3D POINT CLOUD / MODEL EVALUATION SCORE SHEET

| | Completeness | | | Score (1-10) | Detail | | | Score (1-10) | Comments |
|-----|-------------------------------------|-------------------------------------|-------------------------------------|--------------|--------------------------|-------------------------------------|-------------------------------------|--------------|--------------------------------------|
| | Poor | Mod | Good | | Poor | Mod | Good | | |
| 1_1 | <input checked="" type="checkbox"/> | <input type="checkbox"/> | <input type="checkbox"/> | 4 | <input type="checkbox"/> | <input checked="" type="checkbox"/> | <input type="checkbox"/> | 6 | |
| | <input type="checkbox"/> | <input checked="" type="checkbox"/> | <input type="checkbox"/> | | <input type="checkbox"/> | <input checked="" type="checkbox"/> | <input type="checkbox"/> | | |
| | <input type="checkbox"/> | <input checked="" type="checkbox"/> | <input type="checkbox"/> | | <input type="checkbox"/> | <input checked="" type="checkbox"/> | <input type="checkbox"/> | | |
| | <input type="checkbox"/> | <input checked="" type="checkbox"/> | <input type="checkbox"/> | | <input type="checkbox"/> | <input checked="" type="checkbox"/> | <input type="checkbox"/> | | |
| 1_2 | <input type="checkbox"/> | <input type="checkbox"/> | <input checked="" type="checkbox"/> | 10 | <input type="checkbox"/> | <input checked="" type="checkbox"/> | <input type="checkbox"/> | 8 | |
| | <input type="checkbox"/> | <input type="checkbox"/> | <input checked="" type="checkbox"/> | | <input type="checkbox"/> | <input type="checkbox"/> | <input checked="" type="checkbox"/> | | |
| | <input type="checkbox"/> | <input type="checkbox"/> | <input checked="" type="checkbox"/> | | <input type="checkbox"/> | <input checked="" type="checkbox"/> | <input type="checkbox"/> | | |
| | <input type="checkbox"/> | <input type="checkbox"/> | <input checked="" type="checkbox"/> | | <input type="checkbox"/> | <input checked="" type="checkbox"/> | <input type="checkbox"/> | | |
| 1_3 | <input type="checkbox"/> | <input type="checkbox"/> | <input checked="" type="checkbox"/> | 10 | <input type="checkbox"/> | <input type="checkbox"/> | <input checked="" type="checkbox"/> | 10 | Best of group |
| | <input type="checkbox"/> | <input type="checkbox"/> | <input checked="" type="checkbox"/> | | <input type="checkbox"/> | <input type="checkbox"/> | <input checked="" type="checkbox"/> | | |
| | <input type="checkbox"/> | <input type="checkbox"/> | <input checked="" type="checkbox"/> | | <input type="checkbox"/> | <input type="checkbox"/> | <input checked="" type="checkbox"/> | | |
| | <input type="checkbox"/> | <input type="checkbox"/> | <input checked="" type="checkbox"/> | | <input type="checkbox"/> | <input type="checkbox"/> | <input checked="" type="checkbox"/> | | |
| 2_1 | <input checked="" type="checkbox"/> | <input type="checkbox"/> | <input type="checkbox"/> | 5 | <input type="checkbox"/> | <input checked="" type="checkbox"/> | <input type="checkbox"/> | 6 | |
| | <input type="checkbox"/> | <input type="checkbox"/> | <input checked="" type="checkbox"/> | | <input type="checkbox"/> | <input checked="" type="checkbox"/> | <input type="checkbox"/> | | |
| | <input type="checkbox"/> | <input checked="" type="checkbox"/> | <input type="checkbox"/> | | <input type="checkbox"/> | <input checked="" type="checkbox"/> | <input type="checkbox"/> | | |
| | <input type="checkbox"/> | <input checked="" type="checkbox"/> | <input type="checkbox"/> | | <input type="checkbox"/> | <input checked="" type="checkbox"/> | <input type="checkbox"/> | | |
| 2_2 | <input type="checkbox"/> | <input checked="" type="checkbox"/> | <input type="checkbox"/> | 7 | <input type="checkbox"/> | <input type="checkbox"/> | <input checked="" type="checkbox"/> | 10 | |
| | <input type="checkbox"/> | <input checked="" type="checkbox"/> | <input type="checkbox"/> | | <input type="checkbox"/> | <input checked="" type="checkbox"/> | <input type="checkbox"/> | | |
| | <input type="checkbox"/> | <input checked="" type="checkbox"/> | <input type="checkbox"/> | | <input type="checkbox"/> | <input checked="" type="checkbox"/> | <input type="checkbox"/> | | |
| | <input type="checkbox"/> | <input checked="" type="checkbox"/> | <input type="checkbox"/> | | <input type="checkbox"/> | <input checked="" type="checkbox"/> | <input type="checkbox"/> | | |
| 2_3 | <input type="checkbox"/> | <input type="checkbox"/> | <input checked="" type="checkbox"/> | 8 | <input type="checkbox"/> | <input type="checkbox"/> | <input checked="" type="checkbox"/> | 10 | Keeps Crashing Best of group |
| | <input type="checkbox"/> | <input type="checkbox"/> | <input checked="" type="checkbox"/> | | <input type="checkbox"/> | <input type="checkbox"/> | <input checked="" type="checkbox"/> | | |
| | <input type="checkbox"/> | <input checked="" type="checkbox"/> | <input type="checkbox"/> | | <input type="checkbox"/> | <input checked="" type="checkbox"/> | <input type="checkbox"/> | | |
| | <input type="checkbox"/> | <input checked="" type="checkbox"/> | <input type="checkbox"/> | | <input type="checkbox"/> | <input checked="" type="checkbox"/> | <input type="checkbox"/> | | |
| 3_1 | <input type="checkbox"/> | <input checked="" type="checkbox"/> | <input type="checkbox"/> | 4 | <input type="checkbox"/> | <input checked="" type="checkbox"/> | <input type="checkbox"/> | 6 | large curvature |
| | <input type="checkbox"/> | <input checked="" type="checkbox"/> | <input type="checkbox"/> | | <input type="checkbox"/> | <input checked="" type="checkbox"/> | <input type="checkbox"/> | | |
| | <input type="checkbox"/> | <input checked="" type="checkbox"/> | <input type="checkbox"/> | | <input type="checkbox"/> | <input checked="" type="checkbox"/> | <input type="checkbox"/> | | |
| | <input checked="" type="checkbox"/> | <input type="checkbox"/> | <input type="checkbox"/> | | <input type="checkbox"/> | <input checked="" type="checkbox"/> | <input type="checkbox"/> | | |
| 3_2 | <input type="checkbox"/> | <input type="checkbox"/> | <input checked="" type="checkbox"/> | 7 | <input type="checkbox"/> | <input type="checkbox"/> | <input checked="" type="checkbox"/> | 8 | Kept Crashing Very visible people |
| | <input type="checkbox"/> | <input checked="" type="checkbox"/> | <input type="checkbox"/> | | <input type="checkbox"/> | <input checked="" type="checkbox"/> | <input type="checkbox"/> | | |
| | <input type="checkbox"/> | <input checked="" type="checkbox"/> | <input type="checkbox"/> | | <input type="checkbox"/> | <input checked="" type="checkbox"/> | <input type="checkbox"/> | | |
| | <input type="checkbox"/> | <input checked="" type="checkbox"/> | <input type="checkbox"/> | | <input type="checkbox"/> | <input checked="" type="checkbox"/> | <input type="checkbox"/> | | |
| 3_3 | <input type="checkbox"/> | <input type="checkbox"/> | <input checked="" type="checkbox"/> | 10 | <input type="checkbox"/> | <input type="checkbox"/> | <input checked="" type="checkbox"/> | 10 | Best of group |
| | <input type="checkbox"/> | <input type="checkbox"/> | <input checked="" type="checkbox"/> | | <input type="checkbox"/> | <input type="checkbox"/> | <input checked="" type="checkbox"/> | | |
| | <input type="checkbox"/> | <input type="checkbox"/> | <input checked="" type="checkbox"/> | | <input type="checkbox"/> | <input type="checkbox"/> | <input checked="" type="checkbox"/> | | |
| | <input type="checkbox"/> | <input type="checkbox"/> | <input checked="" type="checkbox"/> | | <input type="checkbox"/> | <input type="checkbox"/> | <input checked="" type="checkbox"/> | | |
| 4_1 | <input type="checkbox"/> | <input checked="" type="checkbox"/> | <input type="checkbox"/> | 7 | <input type="checkbox"/> | <input type="checkbox"/> | <input checked="" type="checkbox"/> | 10 | Best of group |
| | <input type="checkbox"/> | <input checked="" type="checkbox"/> | <input type="checkbox"/> | | <input type="checkbox"/> | <input type="checkbox"/> | <input checked="" type="checkbox"/> | | |
| | <input type="checkbox"/> | <input checked="" type="checkbox"/> | <input type="checkbox"/> | | <input type="checkbox"/> | <input type="checkbox"/> | <input checked="" type="checkbox"/> | | |
| | <input type="checkbox"/> | <input checked="" type="checkbox"/> | <input type="checkbox"/> | | <input type="checkbox"/> | <input type="checkbox"/> | <input checked="" type="checkbox"/> | | |
| 4_2 | <input type="checkbox"/> | <input type="checkbox"/> | <input checked="" type="checkbox"/> | 8 | <input type="checkbox"/> | <input type="checkbox"/> | <input checked="" type="checkbox"/> | 8 | |
| | <input type="checkbox"/> | <input checked="" type="checkbox"/> | <input type="checkbox"/> | | <input type="checkbox"/> | <input checked="" type="checkbox"/> | <input type="checkbox"/> | | |
| | <input type="checkbox"/> | <input checked="" type="checkbox"/> | <input type="checkbox"/> | | <input type="checkbox"/> | <input checked="" type="checkbox"/> | <input type="checkbox"/> | | |
| | <input checked="" type="checkbox"/> | <input type="checkbox"/> | <input type="checkbox"/> | | <input type="checkbox"/> | <input checked="" type="checkbox"/> | <input type="checkbox"/> | | |
| 4_3 | <input type="checkbox"/> | <input type="checkbox"/> | <input checked="" type="checkbox"/> | 7 | <input type="checkbox"/> | <input type="checkbox"/> | <input checked="" type="checkbox"/> | 10 | Kept crashing Tied best of group |
| | <input type="checkbox"/> | <input checked="" type="checkbox"/> | <input type="checkbox"/> | | <input type="checkbox"/> | <input type="checkbox"/> | <input checked="" type="checkbox"/> | | |
| | <input type="checkbox"/> | <input checked="" type="checkbox"/> | <input type="checkbox"/> | | <input type="checkbox"/> | <input type="checkbox"/> | <input checked="" type="checkbox"/> | | |
| | <input type="checkbox"/> | <input checked="" type="checkbox"/> | <input type="checkbox"/> | | <input type="checkbox"/> | <input type="checkbox"/> | <input checked="" type="checkbox"/> | | |

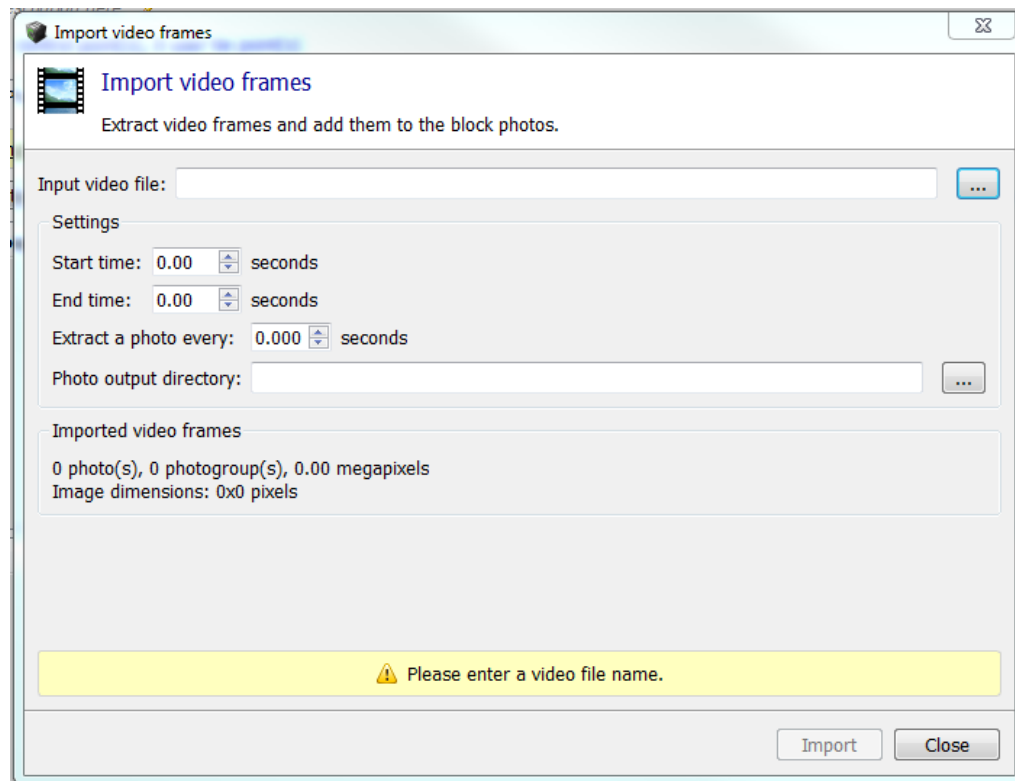
10. Appendix C: UAV Flight Workflow



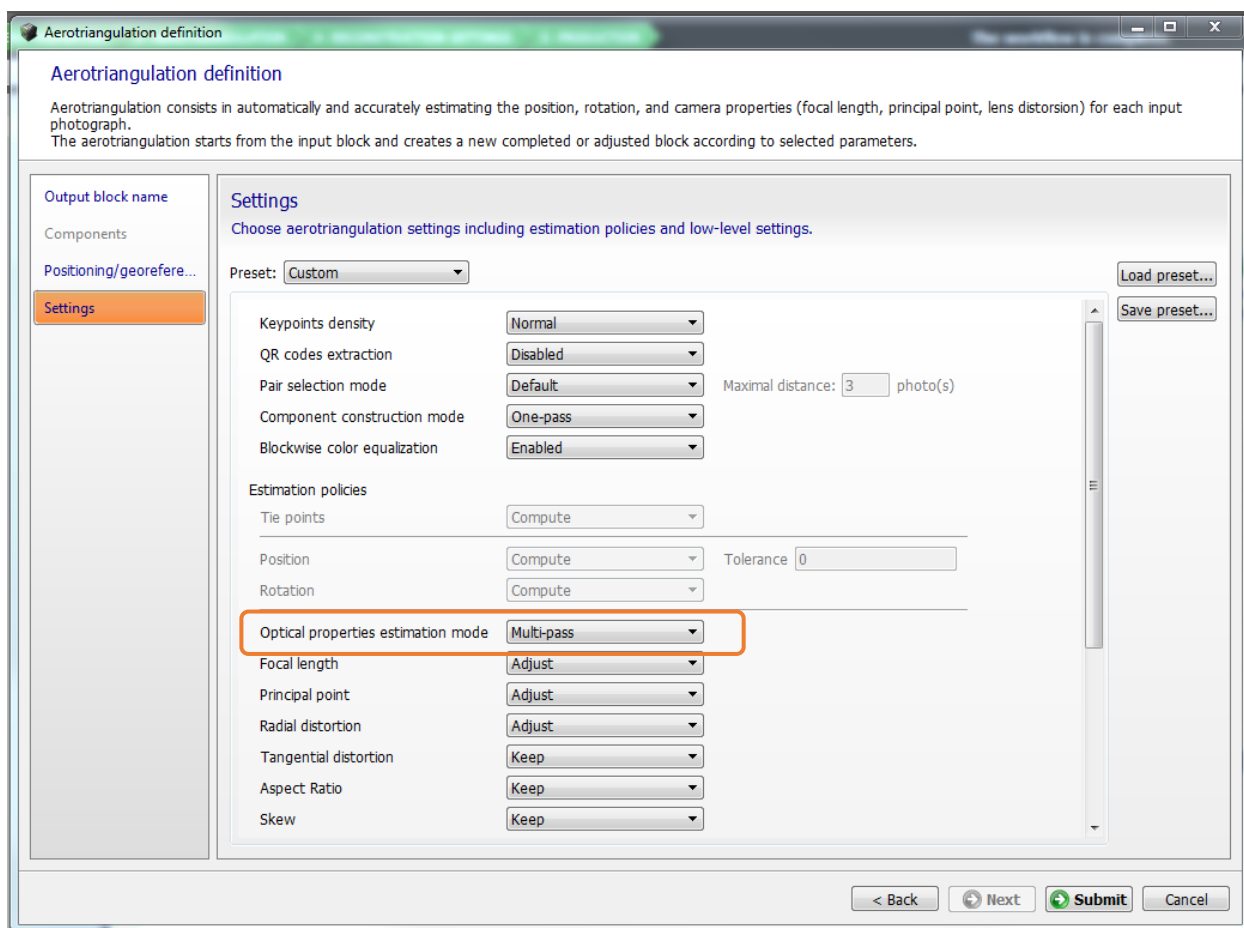
11. Appendix D: Workflow for Completing Photogrammetric Point Cloud Analysis

Construct Photogrammetric Point Cloud

1. Open Bentley ContextCapture (www.bentley.com/en/products/brands/contextcapture) and start a new project . Define the project name and location. An empty block, or project file, is created.
2. Navigate to the *Photos* tab and select *Import Videos*. Choose the UAV video file and enter the start time and end time corresponding to the beginning and end of the UAV flight in the video. Choose the rate to extract still images; depending on the flight speed and length, the image extraction rate may be between every 0.5-2 seconds. Import the video frames.



- If the sensor size and focal length of the camera are known, enter them next to the photogroup parameters in the *Photos* tab. If this information is not known, continue to step 4.
- Navigate to the *General* tab and select *Submit Aerotriangulation*. This step will identify tie points between overlapping images and create a sparse point cloud that can be viewed in the *3D View* tab. In the *Settings* tab of the *Aerotriangulation definition* window, change the *optical properties estimation mode* to *Multi-pass*.



- After the aerotriangulation is complete, select *New Reconstruction*. In the new reconstruction, select *Submit New Production*. In the *Purpose* tab of the *Production*

definition window, choose *3D point cloud*. Submit the production. The default file format is *.LAS*, which can be imported and manipulated in other software.

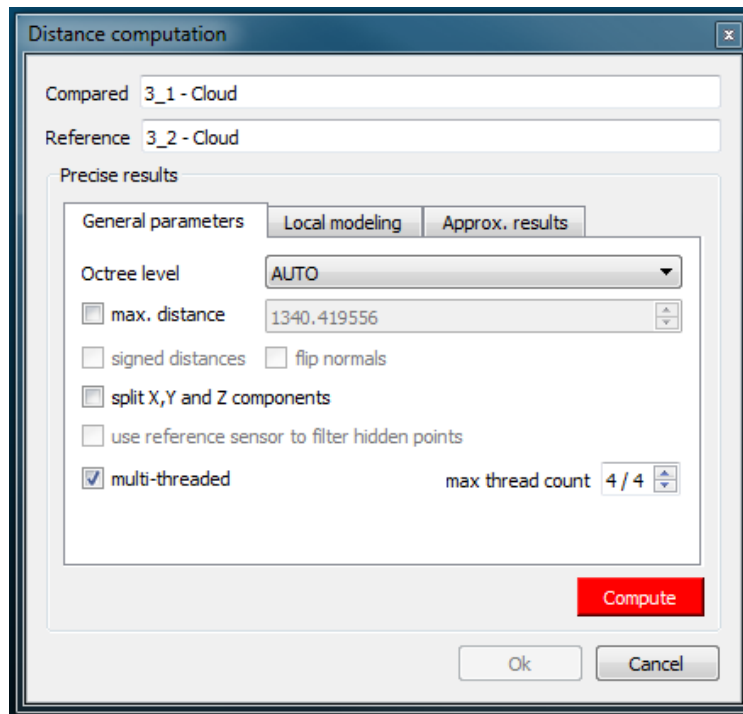
6. Once the point cloud is built, select *Submit New Production*. In the *Purpose* tab of the *Production definition* window, choose *3D mesh*. In the *Format/Options* tab, select the desired file format. The default file format is *.3MX*, which is specific to ContextCapture. Submit the production. Once the production is complete, the mesh can be viewed in the *3D View* tab.
7. If any other outputs are desired, build and export them using *Submit New Production*. This could include an orthophoto or DSM.

Photogrammetric Point Cloud Analysis

1. Open CloudCompare (available from <https://www.danielgm.net/cc/>). Add the Compass plugin if planar surfaces will be measured.
2. Import the georeferenced LiDAR point cloud (*.LAS*) by navigating to *File > Open* and selecting the appropriate file. Select *Apply* in the *Open LAS File* window. In the *Global shift/scale* window, select *No*.
3. Import the photogrammetric point cloud (*.LAS*) following the same steps.
4. Roughly align the photogrammetric point cloud to the LiDAR point cloud by selecting the photogrammetric point cloud in the DB Tree. Go to *Tools > Registration > Match bounding-box centers*. Next select both point clouds in the DB Tree and select *Edit > Multiply/Scale*. Choose a scale factor to approximately match the size of the point clouds. Select the photogrammetric point cloud in the DB Tree and choose *Edit >*

Translate/Rotate. Match the orientation and position of the point cloud as closely as possible to the LiDAR point cloud.

5. Complete the fine alignment by selecting both point clouds in the DB Tree and choosing *Tools > Registration > Fine Registration*. Set the LiDAR point cloud as the *Reference* point cloud. Check the box to *Adjust Scale*. The RMS difference between the point clouds will be displayed in the output window.
6. With both point clouds selected in the DB Tree, compare the accuracy of the photogrammetric point cloud by selecting *Compute Cloud/Cloud Distance* in the toolbar. Set the LiDAR point cloud as the *Reference* point cloud. Select OK.
7. In the *Distance computation* window, select *Compute* to run the comparison. Once this is complete, select OK.

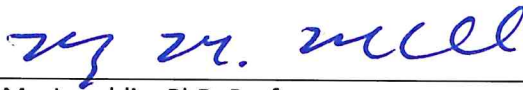


8. A colored point cloud will be produced, and the mean error and standard deviation will be displayed in the Console.

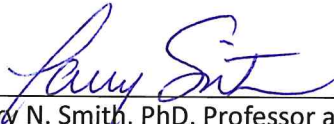
9. To add the color scale legend, select the point cloud in the DB Tree. In the *Properties* window, check *Visible* under the *Color Scale* subsection.

SIGNATURE PAGE

This is to certify that the thesis prepared by Rachel Becker entitled "Development of a Methodology for the Evaluation of UAV-Based Photogrammetry: Implementation at an Underground Mine" has been examined and approved for acceptance by the Department of Geological Engineering, Montana Technological University, on this 25th day of April, 2019.



Mary MacLaughlin, PhD, Professor
Department of Geological Engineering
Chair, Examination Committee



Larry N. Smith, PhD, Professor and Department Head
Department of Geological Engineering
Member, Examination Committee



Jeremy Crowley, MS, Hydrogeologist and Assistant Professor
Montana Bureau of Mines and Geology
Member, Examination Committee